University of Alberta

Gas Injection in Water for Artificial Aeration and Circulation

by

Iran Eduardo Lima Neto ©

A thesis submitted to the
Faculty of Graduate Studies and Research
in partial fulfillment of the requirements for the degree of

Doctor of Philosophy
in
Water Resources Engineering

Department of Civil and Environmental Engineering
Edmonton, Alberta

Fall 2007

Library and
Archives Canada

Published Heritage
Branch

395 Wellington Street
Ottawa ON K1A 0N4
Canada

Bibliothèque et
Archives Canada

Direction du
Patrimoine de l'édition

395, rue Wellington
Ottawa ON K1A 0N4
Canada

Your file Votre référence
ISBN: 978-0-494-33017-3
Our file Notre référence
ISBN: 978-0-494-33017-3

NOTICE:
The author has granted a non-exclusive license allowing Library and Archives Canada to reproduce, publish, archive, preserve, conserve, communicate to the public by telecommunication or on the Internet, loan, distribute and sell theses worldwide, for commercial or non-commercial purposes, in microform, paper, electronic and/or any other formats.

The author retains copyright ownership and moral rights in this thesis. Neither the thesis nor substantial extracts from it may be printed or otherwise reproduced without the author's permission.

AVIS:
L'auteur a accordé une licence non exclusive permettant à la Bibliothèque et Archives Canada de reproduire, publier, archiver, sauvegarder, conserver, transmettre au public par télécommunication ou par l'Internet, prêter, distribuer et vendre des thèses partout dans le monde, à des fins commerciales ou autres, sur support microforme, papier, électronique et/ou autres formats.

L'auteur conserve la propriété du droit d'auteur et des droits moraux qui protège cette thèse. Ni la thèse ni des extraits substantiels de celle-ci ne doivent être imprimés ou autrement reproduits sans son autorisation.

In compliance with the Canadian Privacy Act some supporting forms may have been removed from this thesis.

While these forms may be included in the document page count, their removal does not represent any loss of content from the thesis.

Conformément à la loi canadienne sur la protection de la vie privée, quelques formulaires secondaires ont été enlevés de cette thèse.

Bien que ces formulaires aient inclus dans la pagination, il n'y aura aucun contenu manquant.

Canada

To my wife Andrea,
parents Iran and Catarina,
and sisters Isabela and Carolina

Abstract

This thesis presents investigations on gas injection in water, including a large-scale study on river aeration and four subsequent laboratory-scale studies on bubble plumes and gas-liquid jets. The purpose of the first investigation was to evaluate the effectiveness of a new artificial aeration technique, in which pure oxygen was injected into an effluent pipeline and discharged into a river as a gas-liquid jet. This technique takes advantage of the existing effluent outfall for artificial aeration and was shown to be an effective means of improving the dissolved oxygen levels in the river. The purpose of the laboratory investigations was to better understand the effect of tank size and geometry, nozzle type, and different gas injection methods on the artificial aeration/circulation potential of bubble plumes and gas-liquid jets. The experimental results can be applied for many engineering applications, including the above-mentioned river aeration technique as well as lake/reservoir restoration and wastewater treatment, and can also be used for evaluation and validation of computational fluid dynamic (CFD) models for simulation of gas-liquid flows. Important fundamental results obtained in this thesis such as increased bubble relative velocity on bubble swarms, as compared to that of isolated bubbles, and increased liquid volume flux in bubbly jets, as compared to that of simple water jets, will also help the understanding of complex interactions involved in two-phase flows.

Acknowledgements

I gratefully acknowledge my PhD scholarship funded by the Coordination for the Improvement of Higher Education Personnel Foundation (CAPES), Brazilian Government.

I am very grateful to my supervisors Dr. David Zhu and Dr. Nallamuthu Rajaratnam for their invaluable guidance and encouragement. Their support throughout the entire course of my studies helped me overcome many obstacles. It was a privilege to work under their supervision.

I am thankful to Dr. Tong Yu for his advices, encouragement and helpful insights to this thesis. Likewise I would like to thank Dr. John Gulliver, Dr. Peter Steffler and Dr. Sean Sanders for their time and efforts in reading this thesis thoroughly and making very helpful comments and suggestions.

I wish to thank Mr. Mark Spafford and Dr. Preston McEachern for their important contributions to Chapter 2. Field data provided by Mrs. Chandra Mahabir were also a great help.

I thank Perry Fedun and Chris Kraft for building the experimental setups and for their willingness to help. I wish to extend my thanks to Dr. Mark Loewen for his flexibility in sharing the water tank facility used in this study. The support from my friends Adriana Camino, Ali Kiany, Aqeel Jalil, Faheem Sadeque, German Rojas, Hesham Fouli, Minnan Liu, Moniz Mukto, Shaheli Masoom, Shoma Tanzeeba and Yaser Shammaa, was also a great help. It was a pleasure to meet you all and share this valuable experience at the University of Alberta.

I would like to express my deepest gratitude to my previous supervisors in Brazil, Dr. José Carlos de Araújo and Dr. Rodrigo de Melo Porto, for their encouragement and friendship. Their support in my journey to Canada, in addition to that from Dr. Fazal Chaudhry, is also gratefully acknowledged.

I am very thankful to Álvaro Lemenhe and his family for their enormous help when my wife and I came to Canada and for their constant friendship. Likewise I thank my friends Alexandre Wanderley, Beatriz Zinezi, Breno Diógenes, Jack Dawe, Leandro Prado, Luciane de Almeida, Marcelo Medeiros, Maurício Dollabela and their families.

I deeply thank my brothers Antônio Eugênio Vieira Filho, Eduardo Sturtz and Wladyr Uchôa, my best men Camilo Diógenes, Fábio Lavor, Felipe Freire, Flávio Sidou and Tibério Pinheiro, as well as my friends from our group *cearaminas*, especially João Fernando Menescal and Luis Eduardo Carvalho, for their great support and friendship.

A special thanks goes to my family and my wife's family for their love, encouragement and support that always provide me the strength to become a better person and to achieve my aspirations. Finally, thanks God for everything in my life.

Table of Contents

Chapter 1 1

General Introduction 1

1.1 Dissolved Oxygen and Water Quality 1

1.2 Artificial Aeration and Circulation 2

1.3 Thesis Organization 6

Chapter 2 9

Dissolved Oxygen Downstream of an Effluent Outfall in an Ice-Covered River: Natural and Artificial Aeration 9

2.1. Introduction 9

2.2. Physical characteristics and field work 12

2.3. Modeling open-water lead development 16

2.4. Dissolved oxygen balance model and surface aeration 22

2.5. Efficiency of oxygen injection 27

2.6. Summary and conclusions 30

2.7. Notation 32

Chapter 3 34

Effect of Tank Size and Geometry on the Flow Induced by Circular Bubble Plumes and Water Jets 34

3.1. Introduction 34

3.2. Experimental setup and procedure 36

3.3. Results and discussions 40

3.4. Summary and conclusions 51

3.5. Notation 53

Chapter 4 55

Air Injection in Water with Different Nozzles 55

4.1. Introduction 55

4.2. Experimental apparatus and program 58

4.3. Experimental results and analysis 65

4.4. Applications 81

4.5. Summary and conclusions 83

4.6. Notation 84

Chapter 5 86

Bubbly Jets in Stagnant Water 86

5.1. Introduction 86

5.2. Experimental apparatus and program 87

5.3. Results and discussions 91

5.4. Conclusions 103

5.6. Notation 104

Chapter 6 106

Horizontal Injection of Gas-Liquid Mixtures in a Water Tank 106

6.1 Introduction 106

6.2. Experimental setup and procedure 107

6.3. Experimental results and analysis 111

6.4. Applications 122

6.5. Summary and conclusions 123

6.6. Notation.......... 125

Chapter 7.......... 127

General Conclusions and Recommendations for Future Research.......... 127

References.......... 130

List of Tables

Table 2-1. Characteristics of the Athabasca River during ice-covered periods (Al-Pac location) ... 13

Table 2-2. Comparison between the plume width and dilution rate obtained by Beak Consultants Ltd. (1995) and CORMIX2 simulation. ... 19

Table 2-3. Sensitivity analysis for the parameters used in the thermal breakup model.... 21

Table 2-4. Estimation of the reaeration coefficients by using predictive equations ... 25

Table 2-5. Absorption efficiencies for different artificial aeration systems ... 29

Table 2-6. Summary of all input parameters used in the CORMIX2/thermal breakup and DO balance model simulations... 33

Table 3-1. Details of experimental conditions, showing centerline velocities measured with the propeller anemometer at 40 cm above the nozzle exit for the square and rectangular setups. The water depth was fixed at 0.76 m in all experiments. ... 37

Table 4-1. Estimated volumetric mass transfer coefficients (K_La) for each experimental condition. The values of K_L were obtained from the correlation given by Wüest et al. (1992) and McGinnis and Little (2002) as a function of the mean bubble diameter. ... 60

Table 5-1. Summary of experimental conditions. The first and second numbers in the notation of the experiments correspond respectively to the air and water flow rates at the nozzle. C_o and Re are defined in the text [see Eqs. (5.1) and (5.2)]. ... 89

Table 6-1. Summary of experimental conditions. The gas-volume fraction (ε), Reynolds number (Re) and densimetric Froude number (Fr) are defined by Eqs. (6.2), (6.5) and (6.7), respectively. ... 108

List of Figures

Figure 1-1. Photo of a liquid oxygen tank that feeds a submerged diffuser in a Brazilian River (Rio dos Sinos, RS) (courtesy of FEPAM, RS, Brazil <http://www.fepam.rs.gov.br>). 3

Figure 1-2. Schematic of gas injection for destratification and aeration of lakes and reservoirs (obtained from Socolofsky, 2001).......... 4

Figure 1-3. Schematic of gas injection in ice-covered lakes (obtained from McCord et al., 2000) 4

Figure 1-4. Schematic of gas injection in a large wastewater treatment tank (obtained from García and García, 2006) 5

Figure 1-5. Typical installations of jet aeration systems: series of horizontal air-water jets inline (left) and at the center of a wastewater treatment tank (right) (courtesy of Mixing Systems, Inc., OH, USA <http://www.mixing.com>) 6

Figure 2-1. Location map of the Athabasca River, with indication of the study reach 10

Figure 2-2. Diagram of the effluent discharge near the right bank of the Athabasca River, with indication of the oxygen injection point 11

Figure 2-3. Open-water lead in the Athabasca River downstream of Al-Pac diffuser, with indication of flow direction.......... 12

Figure 2-4. Typical river cross-section at 50 m downstream of Al-Pac diffuser (river discharge is 84 m^3/s), indicating solute (Rhodamine WT dye) effluent concentration, ice thickness and width of the open-water lead (data obtained from Beak Consultants Ltd., 1995) 13

Figure 2-5. Cross-sectional DO variation for each test (data obtained from by Stantec 2004): 16

Figure 2-6. CORMIX2 simulation of transverse mixing downstream of Al-Pac diffuser for February 11th, 2004, in which half-width of the effluent plume corresponds to the distance from the centerline where the temperature is equal to 46% of the centerline value. 18

Figure 2-7. Open-water lead development downstream of Al-Pac diffuser: 21

Figure 2-8. Influence of air and effluent temperatures on the final open-water length 22

Figure 2-9.Comparison of the DO balance model to field data: 26

Figure 3-1. Schematic of experimental apparatus, indicating circulation flow cells at the longer side of the rectangular tank with two plexiglass sheets (for the square setup). Note that the confined setup (not shown in the figure) was obtained by placing a plexiglass box at the center of the tank. 37

Figure 3-2. Typical images obtained using background illumination and dye injection: (a) bubble plumes and (b) water jets (Q_o = 33.3 cm^3/s). Dashed line indicates a 20% spreading with height. 38

Figure 3-3. Instantaneous horizontal velocity (u) measured at r = 15 cm and z = 40 cm (Q_o = 33.3 cm^3/s), periodic component (u''), and turbulent component (u'), for the flow induced by (a) bubble plumes in the square and confined setups and (b) water jets in the square and rectangular (in the longer plane) setups. 41

Figure 3-4. Power spectra of horizontal velocity component u measured at r = 15 cm and z = 40 cm for the square, rectangular (in both shorter and longer planes), and confined setups, indicating dominant frequencies of about 0.03 and 0.11 Hz and the presence of an inertial subrange (line with slope of -5/3): (a) bubble plumes (also indicating a void fraction spectrum for the square setup measured at $r = 0$ cm and $z = 40$ cm); (b) water jets ($Q_o = 33.3$ cm^3/s). 41

Figure 3-5. Typical coherence between the horizontal and vertical velocity components of the flow induced by bubble plumes. 42

Figure 3-6. Variation of the dimensionless wandering frequency with the ratio of jet radius to tank radius (or half-width). Our data points correspond to the air flow rates Q_o of 33.3 and 50.0 cm^3/s, including the 95% confidence intervals (indicated with error bars). Dashed line indicates the region where the wandering frequency becomes independent of b/B, according to the experimental results of Rensen and Roig (2001). 44

Figure 3-7. Time-averaged velocity fields surrounding the (a) bubble plumes and (b) water jets in the (i) square setup, (ii) longer and (iii) shorter planes of the rectangular setup ($Q_o = 33.3$ cm^3/s). Note that the mean vertical velocity $\bar{v}$ is distorted (about 3.5 times smaller). 45

Figure 3-8. Time-averaged velocity field surrounding the bubble plumes in the confined setup 46

Figure 3-9. Streamlines generated from time-averaged PIV measurements for the flow surrounding the (a) bubble plumes and (b) water jets in the (i) square setup, (ii) longer and (iii) shorter planes of the rectangular setup ($Q_o = 50.0$ cm^3/s) 47

Figure 3-10. Variation of the approximate spreading of the surface jet with the ratio of jet radius to tank radius (or half-width) 49

Figure 3-11. Typical axial variation of the normalized turbulent stresses measured at r = 15 cm (Q_o = 33.3 cm^3/s) for (a) bubble plumes and (b) water jets: (i) horizontal normal stresses, (ii) vertical normal stresses, and (iii) shear stresses. 51

Figure 4-1. Schematic of experimental apparatus........ 59

Figure 4-2. Sketch of the nozzle types, indicating number and diameter of the orifices (top view) and the porous airstone nozzle (side view) 59

Figure 4-3. Bubble column tests to validate measurements of void fraction........ 62

Figure 4-4. Tests to validate measurements of bubble size and velocity using the optical probe system: (a) small bubbles, (b) intermediate bubbles and (c) large bubbles (Note: distance between the tips of the probe is 2 mm). 62

Figure 4-5. Typical images of the bubbles for Q_a = 50.0 cm^3/s: (a) single orifice nozzle of 0.6 mm (showing breakup of large bubbles into smaller bubbles); (b) multiple orifice nozzle of 9 x 1.0 mm (showing almost no bubble breakup). 63

Figure 4-6. Typical void fraction time series for the two fiber-optic tips of the RBI probe: measurements taken at r = 2 cm and z = 43 cm (nozzle type: 4 x 1.5 mm, Q_a = 50.0 cm^3/s) 66

Figure 4-7. Typical bubble size distributions obtained from measurements at r = 0 cm and z = 43 cm (Q_a = 33.3 cm^3/s) 66

Figure 4-8. Typical radial distributions of: (a) bubble mean Sauter diameter (also indicating standard deviations); (b) absolute bubble velocity (also indicating mean vertical water velocity); and (c) specific interfacial area (nozzle: Airstone, Q_a = 33.3 cm^3/s). Measurements shown were taken at z = 43 cm........ 67

Figure 4-9. Average radial values of: (a) bubble mean Sauter diameter; (b) absolute bubble velocity; and (c) specific interfacial area. Measurements shown were taken at $z = 43$ cm. 69

Figure 4-10. Adjustment of Eqs. (4.5), (4.6) and (4.7) to experimental data, with dashed lines indicating approximately the maximum variation of each parameter with nozzle type........ 71

Figure 4-11. Power spectrums of horizontal and vertical velocity components (G_u and G_v) measured at $r = 10.8$ cm and $z = 43$ cm, indicating the dominant frequency (0.03 Hz) and the presence of an inertial subrange (line with slope of -5/3)........ 73

Figure 4-12. Velocity decomposition: (a) original velocity signal u measured at $r = 10.8$ cm and $z = 43$ cm; (b) periodic velocity component u''; (c) turbulent velocity component u' 73

Figure 4-13. Time-averaged flow field indicating a velocity scale of 3 cm/s 74

Figure 4-14. Typical axial variation of the turbulent stresses measured at $r = 10.8$ cm... 76

Figure 4-15. Typical axial variation of: (a) cumulative entrainment rate; (b) kinetic energy of the mean flow; (c) kinetic energy of the turbulent flow 77

Figure 4-16. (a) Total entrainment rate; (b) depth-averaged value of kinetic energy of the mean flow; (c) depth-averaged value of kinetic energy of the turbulent flow........ 78

Figure 4-17. Adjustment of Eqs. (4.12), (4.13) and (4.14) to experimental data, with dashed lines indicating approximately the maximum variation of each parameter with nozzle type 80

Figure 5-1. Schematic of experimental apparatus........ 88

Figure 5-2. Bubble images for each experiment (images of 15 x 15 cm^2 with their centers at $r = 0$ and $z = 43$ cm): (a) at a fixed water flow rate, (b) at a fixed air flow rate, and (c) at a fixed gas volume fraction. 90

Figure 5-3. Typical void fraction time series (experiment 3-3). Measurements taken at $r =$ 0 cm and $z = 43$ cm. 92

Figure 5-4. Typical bubble size distributions obtained from optical probe measurementsat $r = 0$ cm and $z = 43$ cm 92

Figure 5-5. Time-averaged radial distributions of: (a) void fraction, (b) bubble frequency, (c) absolute bubble velocity, and (d) bubble diameter for each experimental condition. 94

Figure 5-6. Centerline values of (a) void fraction, (b) bubble frequency, (c) absolute bubble velocity, and (d) bubble diameter. ● – Re = 17684, □ – Re = 14147, △– Re = 10610. 96

Figure 5-7. Radial distributions of axial water velocity. Measurements were taken at $z =$ 43 cm. Lower and upper lines indicate fitted curves for pure water jets (0-2, 0-3, 0-4 and 0-5) and bubbly jets (5-2, 5-3, 5-4 and 5-5), respectively. 96

Figure 5-8. (a) Centerline values of axial water velocity and (b) liquid volume flux of the bubbly jet relative to that of a pure water jet with the same water flow rate at the nozzle. ● – Re = 17684, □ – Re = 14147, △– Re = 10610. 98

Figure 5-9. Typical LIF image of the bubbly jets (Exp. 3-3). 99

Figure 5-10. (a) Variation of bubble slip velocity with bubble diameter and (b) variation of drag coefficient [calculated using Eq. (5.7)] with bubble Reynolds number. 102

Figure 6-1. Schematic of experimental setup. 108

Figure 6-2. Typical images (32 x 50 cm^2) of the bubbles for each experimental condition, showing the tip of the optical probe located at $x = 16$ cm and $z = 24$ cm. 109

Figure 6-3. Typical void fraction and absolute bubble velocity time series. 113

Figure 6-4. Typical bubble size distributions obtained from measurements taken at $x = 16$ cm and $z = 24$ cm. 113

Figure 6-5. Variations along the bubble core centerline of: (a) void fraction, (b) bubble frequency, (c) absolute bubble velocity, (d) bubble diameter, and (e) specific interfacial area. Measurements shown were taken at $z = 24$ cm. 115

Figure 6-6. Adjustment of the dimensionless correlations for (a) length of the bubble core, (b) width of the bubble core, (c) absolute bubble velocity, (d) bubble diameter, and (e) volumetric mass transfer coefficient to experimental data. 117

Figure 6-7. Typical sequence of LIF images (32 x 140 cm^2) at times $t = 0.0$, 6.7, 13.3, and 20.0 s after dye injection (Exp. 3-5). Note that the bubbles are shown in the first image while the water jet development is shown in the subsequent images. Part of the water jet inside the bubble core cannot be visualized because the bubbles blocked the laser sheet. 118

Figure 6-8. Typical variations of mean vertical water velocity along the bubble plume/water jet centerline. Measurements shown were taken at and $z = 24$ cm. 119

Figure 6-9. Dimensionless trajectory of the bubble plumes. 120

Figure 6-10. Dimensionless trajectory of the water jets. Note that data corresponding to Exp. 1-7 (with $Fr > 40$) is excluded because of the occurrence of complete separation between the bubble core and the water jet 120

Figure 6-11. Bubble slip velocity *vs.* bubble diameter. Dashed and solid lines indicate fitted curves obtained from the literature pertaining to isolated bubbles and vertical bubbly flows, respectively. 122

Figure 6-12. Estimated aeration potential for each experimental condition. 123

Chapter 1

General Introduction

1.1 Dissolved Oxygen and Water Quality

The presence of sufficient dissolved oxygen (DO) in natural streams and water bodies is very important because it supports life throughout the entire food chain in the aquatic biota. According to Chapra (1997), the DO budget in such ecosystems is controlled basically by the following supply and demand processes: natural aeration (i.e., oxygen transfer from the atmosphere to the water through surface diffusion), oxygen production by algae (i.e., photosynthesis), oxygen consumption by algae (i.e., respiration), biochemical oxygen demand or BOD (i.e., oxygen utilization by microorganisms to consume the organic matter and nitrogenous compounds); chemical oxygen demand or COD (i.e., oxygen consumption by reducing chemicals such as sulfides and nitrites), and sediment oxygen demand or SOD (i.e., biochemical/chemical oxygen demand to consume the materials on or within the sediments).

In addition to the natural DO demand processes mentioned above, low DO levels in natural streams and water bodies and their negative impacts on water quality have been frequently observed with the fast growing of the human population and development of the cities. This problem has been attributed to the increasing amount of industrial and municipal wastewater discharges, pasture and agricultural runoff, which contain materials that increase the BOD, COD and SOD in receiving waters. Excess nutrient (typically nitrogen and phosphorous) loading also leads to eutrophication, which causes rapid decline of DO levels and deterioration of water quality due to algae bloom, death and decomposition (Chapra, 1997). Eutrophic conditions are even more critical in tropical regions, where droughts reduce significantly river discharges, resulting in lack of water renewal and circulation in lakes and reservoirs (Bouvy et al., 2000), and in cold regions, where ice-cover reduces significantly natural aeration and photosynthesis rates (McCord et al., 2000). Thus, in order to improve the water quality in such ecosystems, artificial aeration techniques are commonly used, and it will be the discussed in next section.

1.2 Artificial Aeration and Circulation

Gas injection systems, mechanical surface aerators, U-tube aerators and hydraulic structures such as weirs and overfalls are artificial aeration techniques that have long been used to supplement the DO and improve the water quality in rivers, estuaries, lakes and reservoirs (Tyler, 1946; Whipple and Yu, 1970; Avery and Novak, 1978; Wüest et al.; 1992; Speece, 1996; McCord et al., 2000; Miller, 2005). Because of their high benefit-cost ratio, gas injection systems are the most popular artificial aeration technique. Over the past two decades, these systems have also become widely accepted and increasingly popular in wastewater treatment technology because of their high efficiency in removing BOD and COD from the effluent (WPCF, 1988; Mueller et al., 2002). Therefore, the focus of this thesis will be on gas injection systems for aeration and circulation in natural waters and wastewater treatment plants.

In gas injection systems, air, pure oxygen or gas-liquid mixtures are pumped through single orifices or diffusers in order to generate bubbles that induce oxygen transfer to the water by diffusion processes, as described by Gulliver (2007). The choice between air and pure oxygen is a debatable issue. While the use of air (which contains about 21% of O_2) saves maintenance and operational costs, the use of pure oxygen (which contains about 99% of O_2) eliminates the problem of supersaturation with respect to nitrogen, which may cause the "gas-bubble" disease of fish (Amberg et al., 1969), and saves costs for electricity consumption, as the rate of oxygen transfer to the water is about 5 times higher due to an increase in the DO saturation concentration (Speece, 1996).

Both gas and gas-liquid injection are widely used for artificial aeration in rivers and estuaries (Amberg et al., 1969, Whipple and Yu, 1970, 1971; Town et al., 1988; Marr et al., 1993, Mueller et al., 2002). Figure 1-1 shows a liquid oxygen tank that feeds a submerged diffuser in a Brazilian River (Rio dos Sinos, RS) in order to increase the DO level and prevent fish kill.

O2
OXIGÊNIO
LIQUIDO

Figure 1-1. Photo of a liquid oxygen tank that feeds a submerged diffuser in a Brazilian River (Rio dos Sinos, RS) (courtesy of FEPAM, RS, Brazil <http://www.fepam.rs.gov.br>).

In stratified lakes and reservoirs, a temperature gradient (thermocline) acts as a barrier preventing exchange of DO between the highly aerated surface water layers (epilimnion) and the poorly aerated deeper water layers (hypolimnion). In these ecosystems, pure oxygen is widely used for hypolimnetic oxygenation to minimize eutrophication (Fast et al., 1975, 1977; Prepas et al., 1997) while air is used both to induce strong circulation flow patterns to destroy stratification and improve DO levels (Wüest et al.; 1992; Sahoo and Luketina, 2005). Thus, in air aeration/destratification systems relatively high gas flow rates are used to produce large bubbles that can penetrate into the thermocline, in contrast with pure oxygen aeration systems, where smaller bubbles are produced to be dissolved in the hypolimnion (Socolofsky, 2001; McGinnis et al., 2004), as shown schematically in Fig. 1-2. However, the implementation of high gas flow rate systems should be done with caution to avoid disturbing bottom sediment, which may lead to deterioration of water quality (Perin et al., 1997).

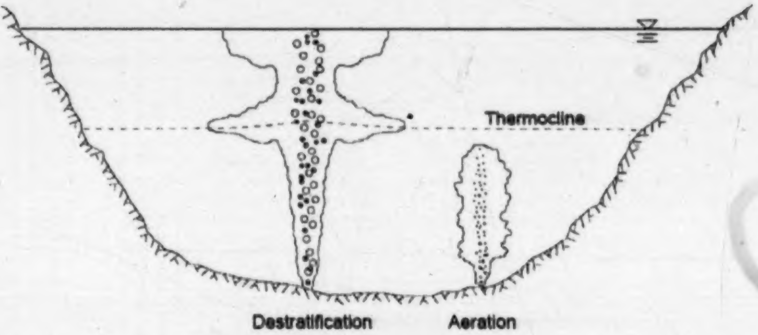

Figure 1-2. Schematic of gas injection for destratification and aeration of lakes and reservoirs (obtained from Socolofsky, 2001)

In ice-covered lakes, the induced circulation flow patterns also bring the heat reserve in the hypolimnetic waters to the surface, melting the ice and developing an open-water area (polynya), where additional oxygen can be transferred from the atmosphere through turbulent diffusion (McCord et al., 2000; Miller, 2005), as shown schematically in Fig. 1-3.

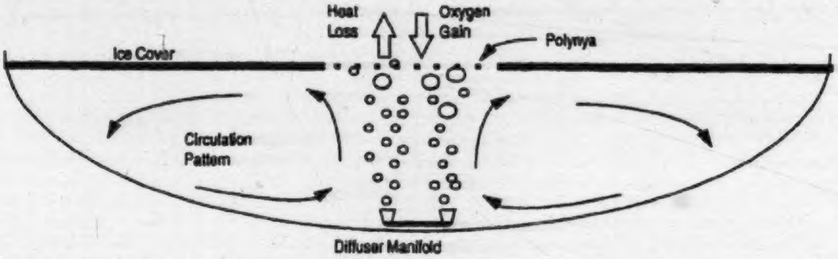

Figure 1-3. Schematic of gas injection in ice-covered lakes (obtained from McCord et al., 2000)

In wastewater treatment systems, gas injection is used to improve the DO levels and generate sufficient flow circulation and mixing to disperse DO and provide uniform concentrations throughout the water (WPCF, 1988; Wagner and Pöpel, 1998; Duchene et al., 2001; Mueller et al., 2002; Schierholz et al., 2006). Another role of these systems is to keep the sediments suspended to avoid the formation of an anaerobic layer at the bottom of the tank (Mueller et al., 2002; Soga and Rehmann, 2004). Figure 1-4 shows schematically an air diffuser system for aeration and mixing in a large wastewater treatment tank. Since aeration systems usually consume between 50 to 90% of the total energy of a municipal wastewater treatment facility (WPCF, 1988; Duchene et al., 2001), it is very important to optimize their design in order to meet the mixing and DO requirements at the lowest cost possible.

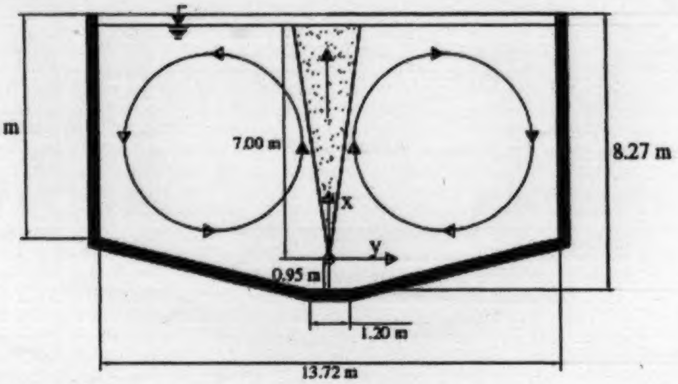

Figure 1-4. Schematic of gas injection in a large wastewater treatment tank (obtained from García and García, 2006)

Gas-liquid injection techniques are also widely used in wastewater treatment systems such as aeration tanks, lagoons and oxidation ditches (Morchain et al., 2000; Fonade et al., 2001, Mueller et al., 2002). These systems, also called jet aerators, combine liquid pumping with gas pumping through mixing chambers, Venturi tubes or ejectors to discharge the mixture as a two-phase jet-plume that provides both aeration and mixing. In most cases, the water depth is small compared to the water surface area and the gas-liquid mixture is discharged horizontally to maximize the contact time between the bubbles and the water. Figure 1-5 shows typical installations of series of horizontal air-water jets inline and at the center of a wastewater treatment tank.

Other common applications of gas injection techniques include promotion of mixing and chemical reactions in metallurgical vessels (Szekely and Themelis, 1971), oxygenation of fish cultures (Colt and Watten, 1988), ocean CO_2 sequestration to minimize global warming effects (Adams et al., 1995), and bubble column reactors (Sommerfeld, 2004). This thesis will focus, however, on gas injection systems for artificial aeration and circulation in natural waters and wastewater treatment tanks.

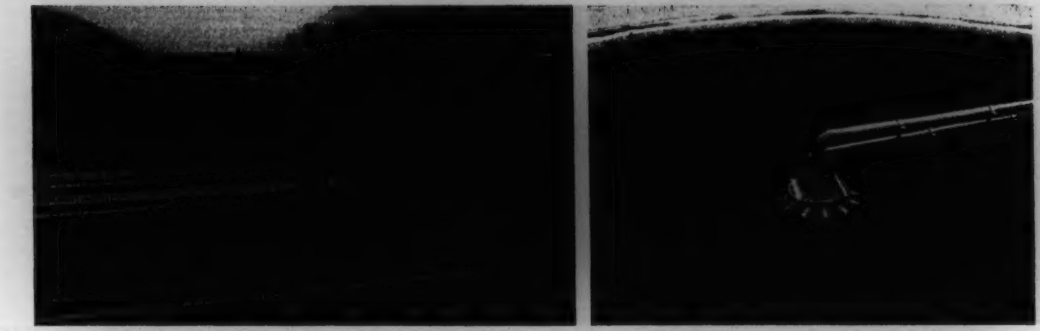

Figure 1-5. Typical installations of jet aeration systems: series of horizontal air-water jets inline (left) and at the center of a wastewater treatment tank (right) (courtesy of Mixing Systems, Inc., OH, USA <http://www.mixing.com>)

1.3 Thesis Organization

This thesis is composed of five contributions on gas injection in water, including a large-scale study on river aeration and four subsequent laboratory-scale studies on bubble plumes and gas-liquid jets. Each contribution is presented in a separate chapter. Following is a brief introduction to each chapter.

Chapter 2 describes a field study and analysis of natural and artificial aeration in the Athabasca River, Alberta, Canada, under ice-covered conditions. In this study, a new oxygen injection technique, in which pure oxygen is injected into the sewage pipeline and discharged into the river, was evaluated. This technique takes advantage of the existing sewage outfall for aeration and was shown to be an effective means of improving DO levels in the river.

Chapter 3 describes laboratory experiments on bubble plumes and water jets in tanks of different size and geometry. The main objective of this study was to better understand the effect of tank size and geometry on the mean, turbulent and periodic flows induced by bubble plumes and water jets as well as to obtain general correlations to describe the oscillatory motions and circulation flow patterns. The results obtained can be used in many engineering applications, including lake/reservoir aeration and circulation, mixing in wastewater treatment tanks, and prevention of suspended solids deposition.

Chapter 4 describes laboratory experiments and analysis of the characteristics of the bubbles and the induced mean-turbulent flow structure generated due to air injection in a water tank. The main goal of this study was to investigate the effect of different nozzle types on bubble plume dynamics, in order to design and optimize air injections systems. The experimental results and correlations obtained can be applied for artificial aeration, circulation and mixing in lakes, reservoirs, wastewater treatment tanks, and low-velocity streams and channels.

Chapter 5 describes laboratory experiments and analysis of the characteristics of the bubbles and the induced mean flow structure generated due to vertical air-water injection in a water tank. Note that the discharge of such gas-liquid jets into the water is similar to the artificial aeration technique described in Chapter 2. The main objective of this study was to investigate the effect of the gas volume fraction and Reynolds number on the behavior of such flows. The experiments revealed fundamental results that can be used to model more accurately vertical bubbly flows. The correlations obtained can also be used to design and optimize artificial aeration and circulation systems in natural waters and wastewater treatment tanks.

Chapter 6 describes laboratory experiments and analysis of the characteristics of the bubbles and the induced mean flow structure generated due to horizontal air-water injection in a water tank. These types of flows are preferred in relatively shallow water systems rather than vertical gas-liquid injection in order to increase the contact time between the gas and liquid. The main goal of this study was to obtain important information on the dynamics of such flows and investigate the effect of the gas volume fraction and densimetric Froude number on the aeration/mixing potential. The results and correlations obtained can be used to design and optimize wastewater treatment systems such as aeration tanks, lagoons and oxidation ditches as well as to better understand river aeration systems as described in Chapter 2.

Chapter 7 presents some general conclusions and recommendations for future research.

A compact disc (CD-ROM) is also provided at the back of this thesis containing an electronic version of the text and information related to each contribution, including raw data and analysis of the errors involved in the measurements.

Chapter 2

Dissolved Oxygen Downstream of an Effluent Outfall in an Ice-Covered River: Natural and Artificial Aeration[*]

2.1. Introduction

The presence of sufficient dissolved oxygen (DO) in rivers is important for aquatic life. Since the late 1980s, pulp mills along the Athabasca River, Alberta, Canada have been under various stages of development or expansion (see Fig. 2-1). High levels of biochemical oxygen demand (BOD) loading from the mill effluents, in addition to natural and municipal discharges, have been shown to cause a pronounced decline in DO concentrations progressively downstream in the river (Chambers et al., 2000). The situation is more critical in winter seasons as a result of low flow conditions, which reduce the ability of the river to dilute BOD, and ice-cover conditions, which stop surface re-aeration and substantially reduce photosynthesis rates.

There is a growing concern that increased development combined with reduced river flows in recent years will cause DO concentrations to fall below critical levels for aquatic biota during winter months. The current guidelines for the maintenance of DO in Alberta Rivers are 5.0 mg/L for acute exposure and 6.5 mg/L for 7-day chronic exposure (Alberta Environment, 1999). Historical low flows occurred in the Athabasca River during the winters of 2002 and 2003. As a result, very low DO concentrations were observed that fell below chronic threshold values. In 2002, for instance, DO concentrations in the Athabasca River declined to an average of 5.7 mg/L for a 28-day period upstream of Grand Rapids (see Fig. 2-1).

In order to minimize the impact of low DO levels in the Athabasca River, Alberta Environment has recently requested that the pulp mills along the river develop contingency plans for their operations. All of the mills are currently operating with efficient wastewater treatment systems and can maintain good water quality in the Athabasca River under all but extreme climate and flow conditions. A low-cost alternative is required for the infrequent climatic conditions that can generate low DO conditions in the river. Oxygen injection into the effluent stream has been proposed as a possible remedy. Alberta-Pacific Forest Industries Inc. (Al-Pac) has recently conducted two oxygen injection tests during one winter season by injecting oxygen into the mill effluent before it is discharged through an existing diffuser outfall (Stantec, 2004) (see Fig. 2-2). While preliminary results seem to indicate that it is possible to increase the DO level by 0.5 mg/L, several complications need to be carefully addressed before its effectiveness can be evaluated: the mixing of the effluent with the ambient river water and the development of the open-water lead downstream of the diffuser.

---

[*] A paper based on the content of this chapter has been accepted for publication in the Journal of Environmental Engineering, ASCE, as Lima Neto et al. (2006b).

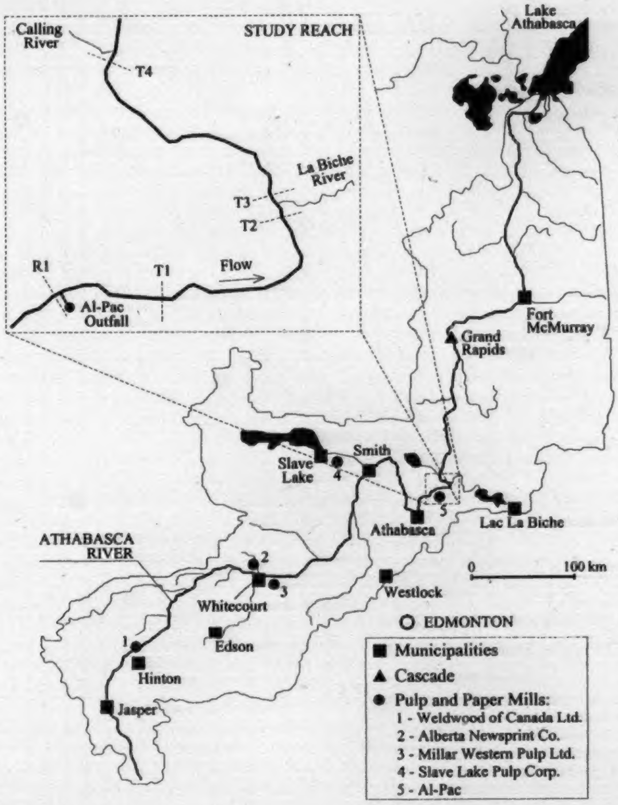
Calling River
STUDY REACH
T4
La Biche River
T3
T2
R1
T1
Flow
Al-Pac Outfall
Lake Athabasca
Fort McMurray
Grand Rapids
Slave Lake
Smith
4
5
Athabasca
Lac La Biche
ATHABASCA RIVER
2
3
Whitecourt
Westlock
0
100 km
EDMONTON
1
Edson
Hinton
Jasper
■ Municipalities
▲ Cascade
● Pulp and Paper Mills:
1 - Weldwood of Canada Ltd.
2 - Alberta Newsprint Co.
3 - Millar Western Pulp Ltd.
4 - Slave Lake Pulp Corp.
5 - Al-Pac

Figure 2-1. Location map of the Athabasca River, with indication of the study reach

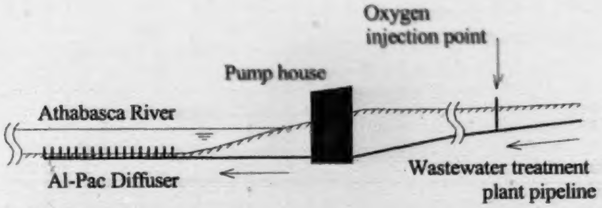

Figure 2-2. Diagram of the effluent discharge near the right bank of the Athabasca River, with indication of the oxygen injection point

The temperature of the mill effluent is typically much warmer than the river water in winter months. It ranges from 10 to 22°C even when the ambient air temperature is below -30°C. This warm effluent thus keeps an open-water lead downstream of the diffuser outfall throughout the winter (see Fig. 2-3). The length of the open-water lead downstream of the Al-Pac diffuser ranges from a few hundred meters to several kilometers, and varies mainly as a function of air temperature and effluent rate and temperature. Given its significant length, it is important to properly estimate the size of the open-water lead as well as the amount of surface aeration it provides. In the Al-Pac's oxygen injection study, it is also important to quantify the amount of the DO level increase due to oxygen injection and that due to surface aeration at the open-water lead. In a recent study by Tian (2005) using USEPA's Water Quality Analysis Simulation Program (WASP) it is shown that the DO level is very sensitive to the ice-cover ratio, i.e. the ratio of the ice-covered surface area to the total river surface area. So far, there is no predictive model for estimating the size of the open-water lead downstream of an effluent outfall.

The objectives of this study are: 1) to develop a methodology for predicting the size of the open-water lead downstream of a diffuser; 2) to assess the ability of a modified Streeter-Phelps model to simulate the DO variation under partially and fully ice-covered conditions; and 3) to evaluate the effectiveness of the above-mentioned oxygen injection system. This study is important for the following reasons: 1) Effluent induced open water zones have not been reported in the literature, and there are no reliable methods for quantifying their sizes. The amount of surface aeration through these open-water zones also needs to be quantified. 2) Injecting oxygen into an effluent diffuser has economical and operational advantages by making use of the existing in-stream diffuser systems. However, there is no documented literature on the application of this approach and its effectiveness.

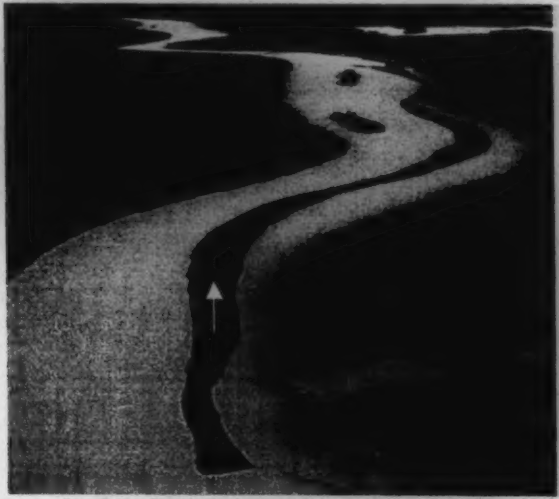

Figure 2-3. Open-water lead in the Athabasca River downstream of Al-Pac diffuser, with indication of flow direction

2.2. Physical characteristics and field work

The Athabasca River originates in the Rocky Mountains of Jasper National Park, Alberta and flows northeast across the province to Lake Athabasca, as indicated in Fig. 2-1. It is unregulated and therefore discharge is highly seasonal, with the lowest flows occurring typically in February (about 70 m^3/s), when the river is largely ice-covered, and the highest flows occurring typically in June (about 1,000 m^3/s), when the river is under ice-free condition. As a result of a number of point and non-point discharges that contribute to the oxygen demand in the river, a DO sag occurs annually at the ice-covered section just above the Grand Rapids, a 10m-cascade located approximately 180 km downstream of the last significant point source discharge which is the Al-Pac effluent diffuser. The main characteristics of the river during ice-covered periods are given in Table 2-1. A typical river cross-section at 50 m downstream of Al-Pac diffuser is shown in Fig. 2-4. The ice thickness, width of the open-water lead caused by the warmer effluent and solute effluent concentration obtained from a field study conducted by Beak Consultants Ltd. (1995) are also shown in this figure.

Table 2-1. Characteristics of the Athabasca River during ice-covered periods (Al-Pac location)

Discharge (m^3/s)	**Water Depth (m)**	**Width (m)**	**Average velocity (m/s)**	**Slope**	**Ice thickness (m)**
84	1.1	250	0.30	0.000166	0.50

Data obtained from Beak Consultants Ltd. (1995) and Putz et al. (2000)

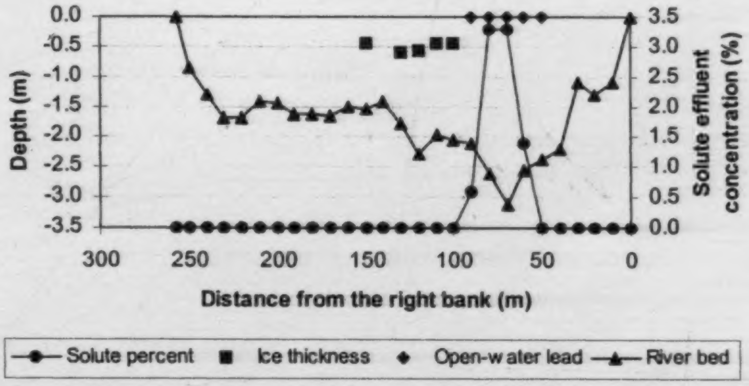

Figure 2-4. Typical river cross-section at 50 m downstream of Al-Pac diffuser (river discharge is 84 m^3/s), indicating solute (Rhodamine WT dye) effluent concentration, ice thickness and width of the open-water lead (data obtained from Beak Consultants Ltd., 1995)

The Al-Pac diffuser is located about 2.7 m below the river bed and extends from approximately 30 to 82 m from the right bank (looking downstream) of the Athabasca River (see Fig. 2-2). Its structure consists of a coated steel pipe of 0.9 m diameter, containing 25 outlet ports with height of 3.0 m and inner diameter of 0.15 m. These outlet ports are oriented along the flow direction with a vertical angle of 45° and have a typical flow velocity of 2 m/s. Since the effluent comes out from the diffuser at a much higher velocity than the river water, it behaves as a series of turbulent jets that act as a propeller contracting the flow and inducing entrainment of the surrounding ambient water. As the effluent is warmer than the river water, buoyancy will also force the jet trajectory to bend upwards. In this region, usually called the near-field zone, significant dilution is achieved within a short distance from the discharge point. After a sufficiently large distance from the diffuser, the effluent is vertically fully mixed and the turbulence in the river becomes the dominant mixing mechanism. In this region, usually called the far-field zone, the effluent behaves as a passive plume that grows in width due to turbulent diffusion processes.

Field work was conducted to evaluate the efficiency of the oxygen injection in the winter of 2004 (Stantec, 2004). The DO level was monitored at five transects across the river channel with one transect before the Al-Pac diffuser to provide background DO concentrations, and four transects below the diffuser from a distance of 6 km up to 32 km (Fig. 2-1). The details of these transects are given below:

a) R1 - Background control site, 0.5 km upstream of the diffuser outfall;
b) T1 - 6 km below the diffuser outfall;
c) T2 - 15 km below the diffuser outfall (0.5 km above La Biche River confluence);
d) T3 - 15.5 km below the diffuser outfall (0.2 km below La Biche River confluence);
e) T4 - 32 km below the diffuser outfall (0.1 km above Calling River confluence).

A baseline study with no oxygen injection was conducted on February 7th , 2004. At the beginning of the tests, the open water lead was about 2 km downstream of Al-Pac diffuser (from Al-Pac, unpublished data). The average wind speed for the time of this survey was 2.8 m/s (Alberta Ambient Air Data Management System, 2004) and air temperature was -8.9 °C (Environment Canada, 2004). In the subsequent days, two oxygen injection tests were conducted with oxygen being injected into the Al-Pac effluent pipeline at 500 m upstream of the pump house (see Fig. 2-2). The first oxygen injection test was conducted from February 10th - 13th, 2004, when the open-water lead was about 4 km downstream of Al-Pac diffuser. The average wind speed was 2.6 m/s and air temperature was -7.2 °C. The second oxygen injection test was conducted from February 17th - 20th, 2004, when the open water lead was about 6 km downstream of Al-Pac diffuser. Due to the continuing increase in the open water length and the safety concerns with working in open areas, the Transect T1 was moved to 7 km below the diffuser outfall during this oxygen injection test. The average wind speed was 1.9 m/s and air temperature was -5.1 °C. The point of the oxygen injection was before the stabilization well in the pump house and the pressure at the effluent pipeline was estimated at about 3 atmosphere pressure. There is a potential that some oxygen might leak into the atmosphere through the stabilization well.

The DO concentrations for the baseline and oxygen injection tests were measured at mid-water column of each station (spaced equally apart across the Transects R1, T1, T2, T3 and T4) with dissolved oxygen meters with an accuracy of ± 0.01 mg/L. Figure 2-5 shows the cross-sectional DO variations for each test. Notice at Transect T3, a significant DO deficit is observed at the station located near the right bank. This low DO is caused by the inflow plume from the La Biche River discharge which does not have an opportunity to mix with the Athabasca river water. The La Biche River discharge is typically small (1.15 m^3/s) compared to the Athabasca River discharge, but it has a low DO concentration (3.55 mg/L) and a BOD of 1.02 mg/L (Chambers et al., 1996). Thus Transect T3 is ignored in the following discussion. At Transect T4, the impact of La Biche River is accounted for by assuming complete mixing between the two rivers. Given the small discharge of the La Biche River (about 2% of the winter flow of the Athabasca River), its impact on the DO levels of the Athabasca River at Transect T4 is not significant. The increase in the average DO concentration (at Transect T1) above background levels (at Transect R1) was much more pronounced for the oxygen injection tests than for the baseline test. However, part of this DO increase was due to the surface aeration at the open-water lead downstream of the outfall (see Fig. 2-3).

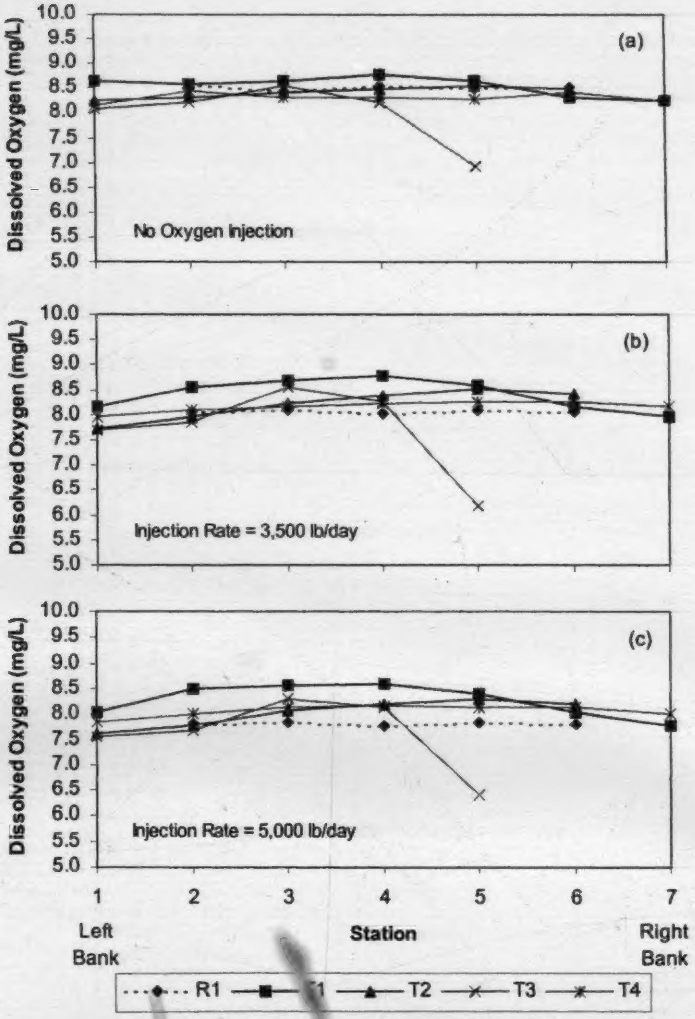

Figure 2-5. Cross-sectional DO variation for each test (data obtained from by Stantec 2004):
(a) Baseline study with no oxygen injection (February 7th, 2004)
(b) Oxygen injection at 3,500 lb/day (February 10th-13th, 2004)
(c) Oxygen injection at 5,000 lb/day (February 17th-20th, 2004)

2.3. Modeling open-water lead development

In this section, we model the development of the open-water lead downstream of Al-Pac diffuser on a daily basis by studying the mixing of the warm effluent in the river. The hydrodynamics of the turbulent buoyant jet/plume in the river is modeled using an expert system, CORMIX2 (Akar and Jirka, 1991). Once the temperature field of the effluent is obtained, the resulting open-water lead development is then predicted using a thermal breakup model (Hicks et al., 1997).

The CORMIX2 model is a subsystem of the software CORMIX-GI 4.3 (www.cormix.info) for simulating submerged multiport diffuser discharges into diverse ambient water conditions. It simplifies the receiving water body's actual geometry by a rectangular cross section (schematization) and uses the "equivalent slot diffuser" concept, which neglects the details of the individual jets issuing from each diffuser port to the distance of their merging, but rather assumes that the flow comes from a long slot discharge with equivalent dynamic characteristics. This model is based upon integral length scale, and passive diffusion approaches to simulate the hydrodynamics of both the near-field zone (where momentum flux, buoyancy flux and diffuser geometry control the jet trajectory and mixing processes), and the far-field zone (where buoyant spreading motions and passive diffusion control the trajectory and dilution of the effluent discharge plume).

In this study, the development of the open water lead during the period of field study (February 7th -20th, 2004) is predicted and the results are compared with the field measurements. The following data were obtained from Stantec (2004) for these dates: the river discharge of 63 m^3/s, effluent flow rate of 0.87 m^3/s and effluent temperature of 22°C. The river cross-section was schematized into a rectangular cross section of a depth of 1.0 m and a width of 230 m according to the requirement of the CORMIX2 model. Manning's roughness for that section of the river was obtained from Beak Consultants Ltd. (1995) and Putz et al. (2000) with $n = 0.027$, typical for mildly meandering channels. The depth at discharge of 1.2 m was also used as input data, whereas the multiport diffuser is located on the deeper part of the channel.

Using the above input data as well as information of the diffuser configuration, CORMIX2 classified the flow in the near-field as a positively buoyant multiport diffuser discharge in uniform ambient layer flow (flow class: MU2) and the flow in the far-field as a passive diffusion plume. The results for the near-field zone simulation showed that vertical mixing is completed at approximately 26 m downstream of Al-Pac diffuser due to the shallowness of the river, where the effluent plume width is 46 m and the centerline temperature is 1.0 °C. The results for the far-field zone simulation showed that at 10 km below the outfall the effluent plume width is 98 m and the centerline temperature is 0.59 °C. Figure 2-6 shows schematically the simulation of the effluent plume downstream of Al-Pac outfall (for February 11th, 2004), where the boundary of the plume is the half-width of the plume, which is defined as the distance from the centerline where the temperature is equal to 46% of the centerline value. The above CORMIX2 model was validated using the field results of Beak Consultants Ltd. (1995). Adjusting the input data to the field conditions of the Athabasca River and Al-Pac effluent discharge during the tracer studies of Beak Consultants Ltd., CORMIX2 simulation provided plume widths of only 18% smaller and dilution rates of only 24% larger (see Table 2-2). Thus the results obtained in the present study with CORMIX2 are expected to be reliable.

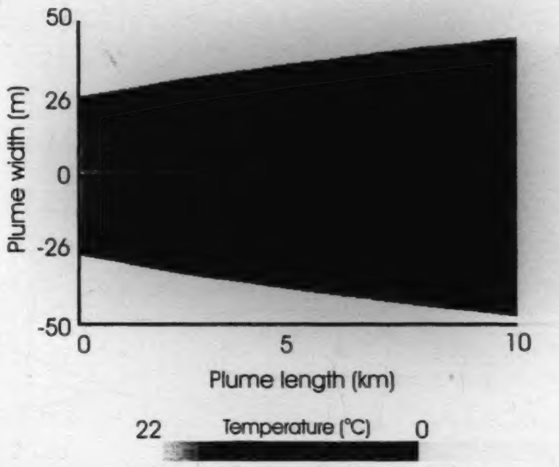

Figure 2-6. CORMIX2 simulation of transverse mixing downstream of Al-Pac diffuser for February 11th, 2004, in which half-width of the effluent plume corresponds to the distance from the centerline where the temperature is equal to 46% of the centerline value.

Table 2-2. Comparison between the plume width and dilution rate obtained by Beak Consultants Ltd. (1995) and CORMIX2 simulation.

Distance (km)	**Plume width (m)** [(1)]		**Dilution (%)** [(2)]	
	Beak Consultants Ltd. (1995)	CORMIX2 Simulation	Beak Consultants Ltd. (1995)	CORMIX2 Simulation
0.05	40	48	30	27
8	110	90	52	42
16	140	113	71	53

(1) Defined as the distance from the centerline where the concentration is equal to 46% of the centerline value.

(2) Defined as the initial concentration divided by the local centerline concentration.

According to Hicks et al. (1997), thermal breakup processes usually occur when warm water flows under the ice-cover resulting in a downstream advance of a melting front. The thermal breakup model validated by Hicks et al. (1997) for the Mackenzie River, Alberta, Canada, is used here to predict the open-water lead development in the Athabasca River. However, their model assumed that the temperature of the water was constant throughout the breakup period, as this warmer water came from a lake (Great Slave Lake). Hence, we modified this model in order to account for spatial variation of effluent temperature downstream of Al-Pac outfall. Thus, temperature contour lines were generated using the results from CORMIX2 and equations to relate effluent temperature and the area formed by these contour lines and the diffuser were obtained.

The open-water lead development was simulated assuming that the melting front follows the temperature contour lines. The ice cover is assumed to melt according to two main processes: ice-thickness reduction, assumed to occur due to direct heat input at the ice surface for a given ice density and latent heat of fusion; and open-water lead development, assumed to occur uniformly over the depth of the ice-cover leading edge due to heat carried by the warm water for a given water density and specific heat. The effluent temperature at the ice-cover leading edge is then obtained with the equations generated from CORMIX2 simulation. This iterative process is repeated for each subsequent day until the simulation reaches the desired area (or length) of the open-water lead.

The following daily average values were used as input data for the thermal breakup model: incoming solar radiation of 150 W/m^2 [obtained from Gray and Prowse (1993) for the Al-Pac's latitude], water surface albedo of 0.1, ice surface albedo of 0.8, and heat transfer coefficient between the air and the water surface of 20 W/m^2 °C (obtained from Hicks et al., 1997).

The development of the open-water lead was simulated from the first day of the field test. On the first day (February 7th, 2004), the length of the open water lead was estimated at 2.0 km based on visual observation. The ice thickness was measured by drilling holes across the river with a power ice auger. While this thickness varied from location to location, an average value of 0.5 m measured upstream of the diffuser (Transect R1 in Fig. 2-1) was used as initial ice thickness. A similar value (see Fig. 2-4) was also reported by Beak Consultants Ltd. (1995) for similar cumulative air temperature conditions. Ice surface temperature was taken to be equal to the mean daily air temperature, which varied from -12.8 to -0.6 °C (Environment Canada). Figure 2-7 shows the estimated open-water lead development obtained by the CORMIX2/thermal breakup model simulation The open-water lead increased significantly from the first to the last day of the simulation. The results are in agreement with the field observations from Al-Pac, in which the open area length was about 4.0 km for February 11th and about 6.0 km for February 18th. Except for the near-field zone, where the effluent jet contracts laterally, as mentioned above, the width of the open-water lead decreases from about 40 to 0 m in the far-field zone (see Fig. 2-3), according to the temperature contour lines sketched in Fig. 2-7. The variation of this width along the river bends is caused by variations in the channel cross-sectional characteristics and increases in the transverse mixing coefficient due to river's secondary currents, which are caused by interactions between the main flow and the river bends, as reported in Dow et al. (2007).

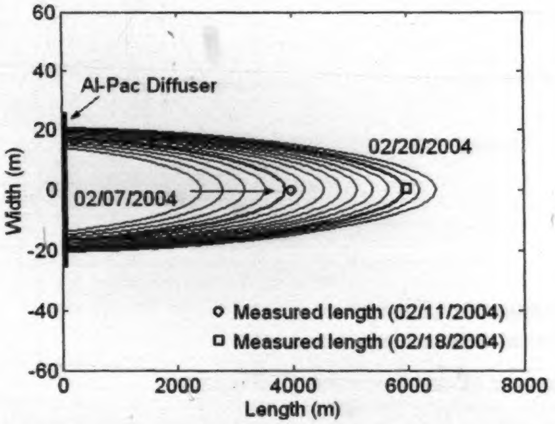

Figure 2-7. Open-water lead development downstream of Al-Pac diffuser: melting front follows temperature contour lines of 0.832, 0.811, 0.792, 0.775, 0.760, 0.746, 0.733, 0.722, 0.712, 0.703, 0.694, 0.686, 0.678 and 0.670 °C

A sensitivity analysis was conducted to investigate the importance of some parameters that are not well known for the time and location of the survey for the following parameter ranges: initial ice thickness (0.4 – 0.6 m), initial open area length (1.5 – 2.5 km), incoming solar radiation (100 – 200 W/m^2), heat transfer coefficient between the air and the water surface (15 – 25 W/m^2 °C), water surface albedo (0.05 – 0.15) and ice surface albedo (0.7 – 0.9). Table 2-3 shows that the initial ice thickness and initial open area length have the largest influence on the results. However, since the maximum variation of the final open area length from the model calculation by using the standard values was about 10%, it can be inferred that the model is not highly sensitive to the range of parameters evaluated in this study.

Table 2-3. Sensitivity analysis for the parameters used in the thermal breakup model

Parameter	Standard value	Range	Variation of the final open-water length (%)
Initial ice thickness (m)	0.5	0.4 – 0.6	+10.13 – -9.39
Initial open area length (km)	2.0	1.5 – 2.5	-4.05 – +3.96
Incoming solar radiation (W/m^2)	150	100 – 200	-1.54 – +1.51
Air-water heat transfer coefficient (W/m^2 °C)	20	15 – 25	+1.05 – -1.08
Water surface albedo	0.1	0.05 – 0.15	+0.29 – -0.31
Ice surface albedo	0.8	0.7 – 0.9	+0.22 – -0.23

The final open-water length as a function of the air and effluent temperatures is studied in Fig. 2-8, with the other input values the same as those in the above simulation. We can see that the lower the air and effluent temperatures, the shorter the final open-water length. For example, when the effluent temperature decreases from 22 to 10°C while the average air temperature remains constant, the length of the final open lead decreases by about 2.4 km. On the other hand, when the average air temperature decreases from 0 to -20°C while the effluent temperature remains constant, the final open lead length decreases by only 0.7 km. This means that the effluent temperature is the main parameter affecting the length of the open water lead. Figure 2-8 can be used as a quick predictive tool for estimating the final length of the open-water lead for similar conditions to our examined case. This graph also shows the sensitivity of the final open-water length to air and effluent temperatures and it will be useful for plant operation.

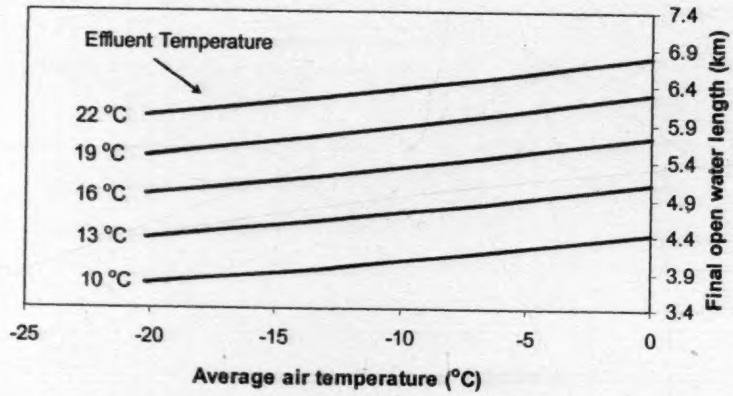

Figure 2-8. Influence of air and effluent temperatures on the final open-water length

2.4. Dissolved oxygen balance model and surface aeration

Dobbins (1964) extended Streeter-Phelps's equation by obtaining a one-dimensional unsteady advection-dispersion equation incorporating reaction terms to simulate the coupling variation of BOD concentration and DO deficit in the river, assuming complete mixing across the channel.

$$\frac{\partial L}{\partial t}+U\frac{\partial L}{\partial x}=\frac{\partial}{\partial x}\left(K_x\frac{\partial L}{\partial x}\right)-K_1L \tag{2.1}$$

$$\frac{\partial D}{\partial t}+U\frac{\partial D}{\partial x}=\frac{\partial}{\partial x}\left(K_x\frac{\partial D}{\partial x}\right)+K_1L-K_2D+K_3-K_4+S \tag{2.2}$$

where L is the BOD concentration; D is the DO deficit (C_S - C), in which C is the DO concentration and C_S is the saturation value; U is the mean river velocity; K_x is the longitudinal dispersion coefficient; K_1 is the BOD decay rate, K_2 is the reaeration coefficient, K_3 is the oxygen uptake rate by algae; K_4 is the oxygen supply rate by algal photosynthesis; and S is the sediment oxygen demand (SOD). Assuming a constant width along the river, Eqs. (2.1) and (2.2) are simplified as following for partially and fully ice-covered conditions.

For partially ice-covered conditions (with open-water lead), the effective surface reaeration coefficient becomes αK_2, where α is the open-water ratio (i.e. the ratio of the open-water width to the average river width of 230m) and K_2 is the reaeration coefficient for an ice-free surface. The value of α varies along the river according the width of the open water lead (see Fig. 2-7). Assuming steady-state conditions and neglecting the dispersion terms (Dobbins, 1964) and the difference between the oxygen uptake and supply rates by algae (Hou and Li, 1987), we obtain the following analytical solutions for Eqs. (2.1) and (2.2)

$$L=L_0\exp\left(-K_1\frac{x}{U}\right) \tag{2.3}$$

$$D=D_0\exp\left(-\alpha K_2\frac{x}{U}\right)+\frac{K_1L_0}{\alpha K_2-K_1}\left[\exp\left(-K_1\frac{x}{U}\right)-\exp\left(-\alpha K_2\frac{x}{U}\right)\right]+\frac{S}{\alpha K_2}\left[1-\exp\left(-\alpha K_2\frac{x}{U}\right)\right] \tag{2.4}$$

in which L_0 and D_0 are the initial BOD concentration and DO deficit, respectively. In Eq. (2.4), the only source of oxygen is the reaeration (controlled by K_2), and the sinks of oxygen are the BOD decay (controlled by K_1) and the sediment oxygen demand, S.

For fully ice-covered conditions, a field study conducted by McDonald et al. (1989) showed that under-ice reaeration coefficient K_2 approaching zero in the Athabasca River. This not only implies that reaeration is negligible but also that groundwater, which is often poorly oxygenated and can contain significant chemical oxygen demand (COD), did not influence K_2 in the studied reach (see Schreier et al., 1980). Thus, for ice-covered conditions, Eq. (2.4) can be simplified by setting K_2 to zero:

$$D = D_0 + L_0\left[1 - \exp\left(-K_1 \frac{x}{U}\right)\right] + S\left(\frac{x}{U}\right) \tag{2.5}$$

where the variation of BOD concentration in the river is also calculated by Eq. (2.3). In Eq. (2.5), there is no source of oxygen due to the ice cover, and two sinks of oxygen: BOD decay and the SOD.

In order to apply the model to predict the change of DO in the Athabasca River downstream of Al-Pac outfall for the baseline study (February 7th, 2004), we used an average value of K_1 of 0.01 day^{-1} (Chambers et al., 1996), corrected to an average effluent plume temperature of 0.90 °C (from CORMIX2 simulation), and an average value of S of 0.18 mg/L/day measured by Tian (2005) for the time and location of our study. However, the value for K_2 depends on several parameters such as river flow conditions and wind shear velocity. For the conditions of the field study: the river discharge (63 m^3/s), water depth (1.0 m), river width (230 m), water surface slope (0.000166), Manning's roughness (n = 0.027), and average wind speed (2.81 m/s), as well as the average effluent plume temperature of 0.90 °C, we calculated values for K_2 by using some of the most popular predictive equations for reaeration induced by pure open-channel flows and combined wind/open-channel flows. Table 2-4 shows that these reaeration coefficients varied from 0.64 to 1.95 day^{-1}. In this study, we adopt a value for $K_2 = 1.63\ \text{day}^{-1}$, which was obtained by Chambers et al. (1996) from their field study for an open-water reach of the Athabasca River downstream of a pulp mill (Millar Western Pulp Ltd.). This value is within the range of K_2 shown in Table 2-4 and seems to be adequate under relatively calm wind conditions. Note that when the wind speed is beyond 6 m/s, K_2 value will increase significantly due to wind generated waves and greater mixing at the air-water interface.

As the dissolved oxygen balance model is a 1-D model, we need to obtain a cross-sectional averaged DO value in order to compare the field measurements with the model predictions. The measured DO varies across the channel due to the process of surface aeration and oxygen injection, with both of the processes giving a higher DO in the effluent plume. It is also interesting to point out that at the R1 section (see Fig. 2-1 insert), DO is more or less uniform (see Fig. 2-5). To obtain a cross-sectional averaged DO concentration, we cannot take a simple math average of the measured DO shown in Fig. 2-5, as in the deeper part of the channel, the unit-width flow rate is bigger, thus the DO flux is larger. As the flow velocity typically increases with depth, the unit-width discharge can be taken from Manning's equation as proportional to the water depth to the power of 1.66. This power of 1.66 is also obtained by Chambers et al. (1996) for the same reach of the Athabasca River evaluated in the present study. Therefore, the cross-sectional averaged DO value is estimated by the following equation:

$$C_{avg} = \sum_{i=1}^{J} C_i (h_i)^{1.66} \Big/ \sum_{i=1}^{J} (h_i)^{1.66} \tag{2.6}$$

where C_i and h_i are the local DO concentration and water depth for each station i, respectively.

Table 2-4. Estimation of the reaeration coefficients by using predictive equations

Reaeration Equation	**K_2 (day^{-1} at 20°C)**	**K_2 (day^{-1} at 0.90°C)**
$K_2 = 3.90\, U^{0.5} H^{-1.5}$ (1)	2.06	1.31
$K_2 = 5.010\, U^{0.969} H^{-1.673}$ (2)	1.46	0.93
$K_2 = 173\, (IU)^{0.404} H^{-0.66}$ (3)	3.07	1.95
$K_2 = 543\, I^{0.6236} U^{0.5325} H^{-0.7258}$ (4)	1.22	0.77
$K_2 = 1{,}740\, I^{0.79} U^{0.46} H^{0.74}$ (5)	1.01	0.64
$K_2 = K_{2,channel} + K_{2,wind}$ (6)	1.63	1.04
$K_2 = K_{2,channel} + K_{2,wind}$ (7)	2.71	1.73

where: H = average water depth (m), I = water surface slope, $K_{2,channel}$ = reaeration coefficient for pure open-channel flows (day^{-1}), and $K_{2,wind}$ = reaeration coefficient for pure wind-driven flows (day^{-1})

(1) O'Connor and Dobbins (1958)
(2) Churchill et al. (1962)
(3) Krenkel and Orlob (1962)
(4) Smoot (1988)
(5) Moog and Jirka (1998), valid for $I > 0.000$
(6) Combination of wind and open-channel flow induced reaeration equations given by Chu and Jirka (2003)
(7) Combination of wind and open-channel flow induced reaeration equations used in the USEPA's WASP model

The following water quality parameters were used as input data for the DO balance model: background BOD of 0.9 mg/L (Alberta Environment, 2004), saturation DO concentration of 13.7 mg/L (Stantec, 2004), effluent DO concentration of 5.6 mg/L and effluent BOD concentration of 3.8 mg/L (Tian, 2005). Figure 2-9(a) shows the prediction of the DO balance model with the measured (cross-sectional averaged) DO concentrations at Transects R1, T1, T2 and T4. Here an average length of the open-water lead (2.2 km) and open-water ratio α (varying from 0.112 to 0) were obtained from the CORMIX2/thermal breakup model simulation. The DO model presents good fit to the field data with correlation coefficient $R^2 = 0.930$.

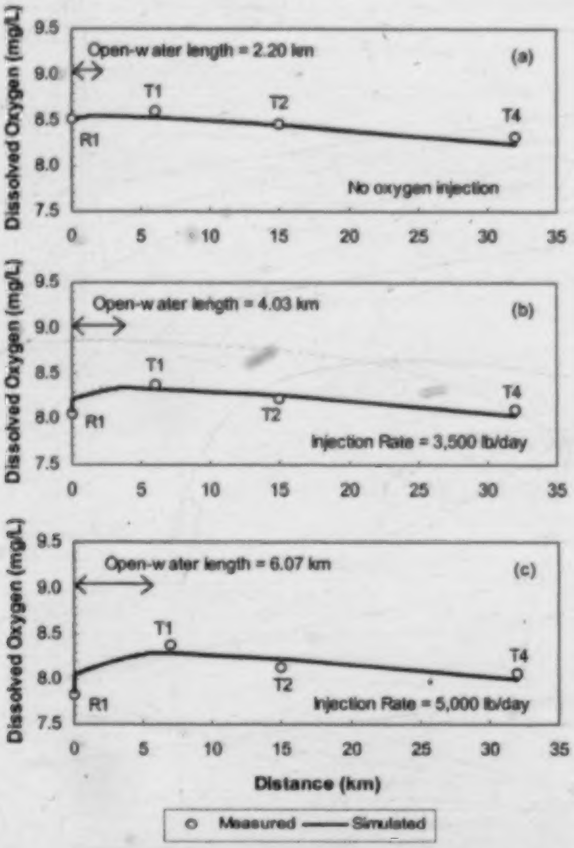

Figure 2-9.Comparison of the DO balance model to field data:
(a) Total DO increase = 0.05 mg/L (α varies from 0.112 to 0)
(b) Total DO increase = 0.30 mg/L, being 52% of this total due to oxygen injection and 48% due to surface aeration (α varies from 0.148 to 0)
(c) Total DO increase = 0.46 mg/L, being 44% of this total due to oxygen injection and 56% due to surface aeration (α varies from 0.174 to 0)

Two important processes are clearly shown in Fig. 2-9(a): the increase of DO (about 0.05 mg/L) in the open-water lead downstream of the diffuser due to surface aeration, and the decrease of DO from the end of the open-water lead to T4 due to a lack of surface aeration and the effects of BOD and SOD. The slope of the DO depletion from T2 to T4 is well modeled, which indicates that the adopted K_1 and S values are reasonable. As K_1 is small compared to S, the DO decrease is dominated by SOD and its slope is almost linear under ice-covered conditions [see Eq. (2.5)]. This linear decrease in DO was also observed by Chambers et al. (1997), who evaluated the impact of effluent discharges in several ice-covered rivers. In the open water region, surface aeration dominates over the SOD and BOD, thus the DO increases. Clearly the values of K_1, K_2 and S can be adjusted to have a better fit of the measurement data in Fig. 2-9(a). However, by using the values obtained from the literature, we demonstrated the importance of the surface aeration in the open-water lead and the reliability of the DO balance model.

2.5. Efficiency of oxygen injection

Artificial aeration has long been successfully applied to minimize the problem of low DO levels in rivers by injecting air or oxygen into the water through submerged multi-port diffusers (Amberg et al., 1969; Whipple and Yu, 1971; Marr et al., 1993). Here we investigate the injection of oxygen into the existing effluent pipeline to make use of the existing in-stream diffuser for maximizing the mixing and oxygen transfer. The approach provides significantly economic benefits and operational advantages. There are, however, several fundamental issues that need to be addressed: related to the dynamics of the gas-bubbles and effluent-water mixture and whether or not the bubbles separate from the effluent plume in the river (see Socolofsky and Adams, 2002). In the present study, we estimate the bulk efficiency of the oxygen injection through a field pilot study.

The field study takes advantage of the existing Al-Pac diffuser by injecting oxygen into the Al-Pac effluent pipeline during periods of critical DO levels in the Athabasca River (see Fig. 2-2). Two tests were conducted with oxygen being injected at a rate of 3,500 lb/day (February 10th – 13th, 2004) and 5,000 lb/day (February 17th – 20th, 2004).

In this section, we apply the DO balance model to estimate the efficiency of this oxygen injection. We used the same values of K_1, K_2, S and water quality parameters assumed in the previous section of this paper. Figure 9(b) shows the prediction of the DO balance model compared with the measured DO concentrations at Transects R1, T1, T2 and T4 for the oxygen injection rate of 3,500 lb/day, considering an average length of the open-water lead (4.03 km) and open-water ratio α (varying from 0.148 to 0) obtained from the CORMIX2/thermal breakup model simulation. The DO model presents good fit to the field data, with the correlation coefficient $R^2 = 0.935$. Three processes are shown in Fig. 2-9(b): DO increase due to oxygen injection, assumed to occur instantaneously right after the diffuser; DO increase from the diffuser to the end of the open-water lead due to the dominant effect of K_2 over K_1 and S; and DO decrease from the end of the open-water lead to T4 due the effects of K_1 and S and lack of surface aeration. The predicted total DO increase from R1 to the end of the open water lead is 0.30 mg/L, which is composed of the surface aeration of the open water lead and the oxygen injection. The DO increase over the open water lead is 0.14 mg/L (i.e., 48% of the total DO increase). The remaining 52% of the total DO increase (or 0.16 mg/L) is due to oxygen injection. This gives the standard oxygen transfer efficiency (SOTE) of 53%. SOTE is defined here as the fraction of oxygen supplied which is actually transferred or dissolved into the water.

Figure 2-9(c) presents the results for the oxygen injection rate of 5,000 lb/day, considering an average length of the open-water lead (6.07 km) and open-water ratio α (varying from 0.174 to 0) obtained from the CORMIX2/thermal breakup model simulation. The DO model also presents good fit to the field data with the correlation coefficient $R^2 = 0.829$. The three processes shown in Fig. 2-9(c) are the same as those described for Fig. 2-9(b). The total DO increase from R1 to the end of the open water lead is 0.46 mg/L, with 0.26 mg/L (or 56% of the total DO increase) due to the open water lead. The remaining 44% of the total DO increase (or 0.21 mg/L) is due to oxygen injection. This gives the SOTE of 49%. In both tests, the amounts of oxygen transferred to the river due to oxygen injection were of the same order of those due to open-water lead reaeration.

The SOTE decreased slightly from 53 to 49% when the amount of the oxygen injection increased from 3,500 lb/day to 5,000 lb/day. It should be noted that these numbers will change when the values of K_1, K_2 and S are adjusted. However, the above results appear to be quite consistent and are expected to be reliable. From Table 2-5 one can see that the SOTE obtained in the present study is higher than those for conventional air injection systems and of the same order of those for oxygen injection systems. This efficiency is, however, lower than that for the U-tube/diffuser system, which has disadvantages such as higher construction/maintenance costs and inflexibility to be modified (Mueller et al., 2002). In this study, some amount of the oxygen injected into the effluent pipeline could have escaped through the stabilization well in the pump house prior to the diffuser outfall.

Table 2-5. Absorption efficiencies for different artificial aeration systems

Type of Aerator	SOTE (%)
Coarse-bubble diffuser (Chicago River) (1)	2 – 10
Coarse-bubble diffuser (Tank) (1)	5 – 25
Fine-bubble diffuser (Tank) (1)	10 – 40
Oxygen diffuser (Androscoggin River) (2)	37
Oxygen sidestream/diffuser (Pearl River) (3)	55
U-tube/diffuser (Tombigbee River) (4)	80 – 90
Present study	*50*

(1) Mueller et al. (2002)
(2) Marr et al. (1993)
(3) Amberg et al. (1969)
(4) Speece (1996)

The amount of the oxygen injection in the present study is relatively small with an increase of DO about 0.2 mg/L in the river. The oxygen injection system used in the Pearl River

(Amberg et al., 1969) was similar to the one used in this study. However, that system increased the DO level by 2 mg/L in the Pearl River by applying a much larger oxygen injection rate (30,000 lb/day). The discharge of the Pearl River (43.2 m^3/s) and the sidestream to be oxygenated (0.71 m^3/s) were of the same order of the Athabasca River discharge (63.0 m^3/s) and the Al-Pac effluent flow rate (0.87 m^3/s), respectively. This comparison illustrates how much the artificial aeration technique evaluated here could potentially improve the DO levels in the Athabasca River if a higher oxygen injection rate were effectively applied.

When a higher oxygen injection rate is applied, Amberg et al. (1969) and Mueller et al. (2002) reported that the SOTE becomes significantly lower as observed in other studies with different artificial aeration systems. Lower SOTE at higher injection rate may be due to coalescence of more numerous bubbles, reducing the surface–to–volume ratio and the contact time with the river water due to increased bubble slip velocities. A laboratory study is currently being conducted to better understand the dynamics of the gas bubble-water mixture and mass transfer under various flow and operation conditions in order to improve the efficiency of oxygen injection systems.

2.6. Summary and conclusions

In this paper, dissolved oxygen level in an ice-covered river downstream of an effluent diffuser is studied with or without oxygen injection. A methodology for predicting the open-water lead development was presented, and natural aeration through this open water lead is studied. The efficiency of oxygen injection into an effluent diffuser is also evaluated through a field test. This study is important in modeling and managing DO levels in ice-covered rivers.

A CORMIX2 model was used to predict the behavior of an effluent plume downstream of the diffuser while a thermal breakup model was adapted to simulate the resulting open-water lead development. This combined CORMIX2/thermal breakup model was able to predict field observations of an open-water advance from about 2 to 6 km in the river over the period of the field study. Model simulations revealed that effluent temperature was the dominant parameter affecting the length of the open-water lead while air temperature was of lesser importance. This predictive tool for estimating the final size of the open-water lead is essential to predict DO depletion resulting from BOD loading to the river and the amount of oxygen that should be injected to offset depletion.

With the results from the CORMIX2/thermal breakup model and the water quality parameters and rates obtained from the literature, it is shown that the spatial variation of DO along the river can be modeled with Streeter-Phelps equations proposed here for partially and fully ice-covered conditions. For the baseline study without oxygen injection, the model properly simulated two important processes: DO increase from the diffuser to the end of the open-water lead (2.2 km long) due to the dominant effect of surface aeration over BOD and SOD; and DO decrease from the end of the open-water lead to the last transect due to a lack of surface aeration and the effects of BOD and SOD. The DO decrease was dominated by SOD with its slope close to linear.

The DO balance model was also applied to evaluate the efficiency of the artificial aeration system by injecting oxygen directly into the effluent pipeline at 3,500 and 5,000 lb/day. For the 3,500 lb/day test, a total DO increase of 0.30 mg/L in the river was estimated, from which 52% was added by oxygen injection and the remaining 48% was added by surface aeration through an open-water lead of 4.03 km long. For the 5,000 lb/day test, the total DO increase was 0.46 mg/L, from which 44% was added by oxygen injection and the remaining 56% was added due to surface aeration through an open-water lead of 6.07 km long. Therefore, the amounts of oxygen transferred to the river due to oxygen injection were of the same order of those due to open-water lead reaeration.

The standard oxygen transfer efficiency was about 50% at both 3,500 lb/day 5,000 lb/day. These efficiencies are higher than those for conventional air injection systems and of the same order of those for oxygen injection systems described in the literature. From these results, it can be inferred that the artificial aeration technique evaluated here can be a low-cost and efficient alternative to minimize the impact of low DO levels in ice-covered rivers. The oxygen transfer efficiency at much higher injection rates is still not clear as there are reports that this efficiency will decrease due to increased bubble coalescence processes and increased bubble slip velocities. Further lab and field studies are needed.

2.7. Notation

The following symbols are used in this chapter:

D = dissolved oxygen deficit (mg/L)

D_0 = initial dissolved oxygen deficit (mg/L)

K_1 = oxygen uptake rate by biochemical oxygen demand (day^{-1})

K_2 = reaeration coefficient (day^{-1})

K_3 = oxygen uptake rate by algae (mg/L/day)

K_4 = oxygen supply rate by algal photosynthesis (mg/L/day)

K_x = longitudinal dispersion coefficient (m^2/s)

L = biochemical oxygen demand concentration (mg/L)

L_0 = initial biochemical oxygen demand concentration (mg/L)

S = sediment oxygen demand (mg/L/day)

$SOTE$ = standard oxygen transfer efficiency, defined as the fraction of oxygen supplied which is actually transferred or dissolved into the water (%)

t = time (s)

U = mean river velocity (m/s)

x = longitudinal distance (m)

α = open-water width divided by the total river width (open-water ratio)

Table 2-6. Summary of all input parameters used in the CORMIX2/thermal breakup and DO balance model simulations.

Parameter	Value
River discharge (m^3/s) (1)	63
Water depth (m) (2)	1.0
Average river width (m) (3)	230
Manning's roughness (4)	0.027
Background BOD (mg/L) (5)	0.9
Saturation DO concentration (mg/L) (1)	13.7
BOD decay rate, K_1 (day^{-1}) (6)	0.01
Reaeration coefficient, K_2 (day^{-1}) (6)	1.63
Sediment oxygen demand, S (mg/L/day) (7)	0.18
Effluent flow rate (m^3/s) (1)	0.87
Effluent temperature (°C) (1)	22
Depth at discharge (m) (8)	1.2
Diffuser length (m) (8)	52
Number of ports (8)	25
Port height (m) (8)	3.0
Port diameter (m) (8)	0.15
Port vertical angle (°) (8)	45
Distance to the right bank (m) (8)	30
Effluent DO concentration (mg/L) (1)	5.6
Effluent BOD concentration (mg/L) (7)	3.8
Daily average air temperatures (°C) (February 7th-20th, 2004) (9)	-8.9, -3.3, -2.2, -6.2, -12.8, -2.4, -7.4, -11.6, -9.1, -9.9, -8.4, -7.4, -3.9, -0.6
Daily average wind speeds (m/s) (February 7th-20th, 2004) (10)	2.8, 3.1, 2.0, 4.2, 1.9, 2.2, 2.3, 2.8, 1.3, 1.9, 2.0, 1.4, 2.3, 2.0
Initial ice thickness (m) (11)	0.5
Initial open area length (km) (11)	2.0
Incoming solar radiation (W/m^2) (12)	150
Air-water heat transfer coefficient (W/m^2 °C) (13)	20
Water surface albedo (13)	0.1
Ice surface albedo (13)	0.8

(1) Stantec (2004)
(2) Water Survey of Canada (2004)
(3) Estimated using the water depth of 1.0 m and the river transects measured by Beak Consultants Ltd. (1995)
(4) Beak Consultants Ltd. (1995) and Putz et al. (2000).
(5) Alberta Environment (2004)
(6) Chambers et al. (1996)
(7) Tian (2005)
(8) Based on engineering plans of the diffuser outfall (Al-Pac)
(9) Environment Canada (2004)
(10) Alberta Ambient Air Data Management System (2004)
(11) Field measurements (Al-Pac).
(12) Obtained from Gray and Prowse (1993) for the Al-Pac's latitude
(13) Obtained from Hicks et al. (1997) for the Mackenzie River, Alberta, Canada

Chapter 3

Effect of Tank Size and Geometry on the Flow Induced by Circular Bubble Plumes and Water Jets[*]

3.1. Introduction

Bubble plumes and water jets are widely used to promote circulation and turbulent mixing in aeration tanks, mixing chambers, reservoirs, lakes and other water bodies (Abramovich, 1963; Rajaratnam, 1976; Socolofsky, 2001; Soga and Rehmann, 2004). While bubble plumes entrain the surrounding liquid mainly due to buoyancy, water jets induce the entrainment mainly due to momentum. Earlier studies have mostly focused on the dynamics of jets and plumes. Only a few studies examined the effects of the tank sizes and geometry on the ambient flows and circulations patterns (Iamandi and Rouse, 1969; Jirka and Harleman, 1979; Fanneløp et al., 1991; Riess and Fanneløp, 1998).

Iamandi and Rouse (1969) studied plane air jets in tanks with different lengths and found that a primary circulation flow cell was formed when this length was up to about 2 times the height of the tank. However, a secondary cell with opposite rotation of the primary cell was also formed when the length of the tank was 4 times its height. In this particular case, the length of the primary cell was about 2.5 times the height of the tank. Jirka and Harleman (1979) investigated buoyant plane water jets with different lengths and water depths and found that circulation cells were formed when the discharge was unstable. But, in contrast with the above mentioned non-buoyant case, no secondary cell was formed even when the length of the tank was about 20 times the water depth. Fanneløp et al. (1991) and Riess and Fanneløp (1998) studied plane water jets and line-source bubble plumes and observed the formation of secondary cells in water tanks with length of about 20 times the water depth. Nevertheless, the length of the primary cell was about 7 times the water depth, which is much larger than that reported by Iamandi and Rouse (1969). In all the above studies, line jets and plumes were used across the channel width; thus the flows were made two-dimensional without 3D effects.

---

[*] A paper based on the content of this chapter has been accepted for publication in the Journal of Hydraulic Engineering, ASCE, as Lima Neto et al. (2007b).

The flow field induced by bubble plumes in confined setups such as bubble column reactors has also been investigated. Experimental studies have shown that the number of vertical circulation cells generated in these setups is close to the ratio of column height to diameter or width (see summary in Mudde, 2005). However, no general description of the effect of tank size and geometry, ranging from confined setups to larger scale tanks, has been provided.

In both confined and unconfined bubble plume setups, a periodic lateral oscillation of the bubble core (also called wandering motion) is usually reported (Rensen and Roig, 2001; García and García, 2006). Rensen and Roig (2001) studied the wandering motion in a confined bubble column and obtained oscillation frequencies ranging from about 0.1 to 0.2 Hz, increasing with the air flow rate following approximately a power law with slope of about 0.50. García and García (2006), on the other hand, studied the wandering motion in a large wastewater treatment tank and obtained much smaller oscillation frequencies (ranging from about 0.002 to 0.003 Hz). They noticed that the frequencies increased with the air flow rate following approximately a power law with slope of about 0.30. This implies that the wandering frequency depends on both tank size and air flow rate, but no general correlation including both small and large scale tanks has been provided. Besides, there remain debates on the mechanism that cause this oscillatory flow, either attributing it to buoyancy-driven instabilities enhanced by the presence of the walls and/or the presence of coherent flow structures. Therefore, measurements of the mean, turbulent and periodic flows induced by bubble plumes and water jets for different tank geometries are necessary to improve knowledge of such flows and to validate computational fluid dynamic codes using advanced techniques such as large-eddy simulation (see Bombardelli, 2004).

In the present study we investigate experimentally the effect of tank size and geometry, including rectangular and square setups, on the mean, turbulent and periodic flow fields induced by circular bubble plumes and water jets. We analyzed our results and combined with those available in the literature to provide a better understanding of such flows.

3.2. Experimental setup and procedure

The experiments were performed using three different setups: a rectangular tank, a square tank and a smaller square tank (called here as the confined setup), shown schematically in Fig. 3-1. The rectangular setup consisted of a glass-walled tank, 1.20 m wide, 1.80 m long and 0.80 m deep. The square setup was built by placing two plexiglass sheets inside the rectangular tank to form a 1.20 m square tank. The confined setup was obtained by placing a plexiglass box of side 0.40 m at the center of the tank in order to reach similar conditions as bubble columns. The water depth was fixed at 0.76 m for all setups. The gas supply was taken from an air line, while the water was pumped from a small reservoir. Both air and water temperatures were about 20°C. Volumetric flow rates of 33.3 and 50.0 cm^3/s were adjusted by rotameters for both the air and water phases (total of 4 experiments for one tank geometry) and discharged through single-orifice nozzles connected to the air and water lines by a PVC pipe with an inner diameter of 25.4 mm. A pressure-regulating valve was used to keep the air pressure at 1 ATM and ensure a constant air flow rate to the nozzle during the bubble plume tests. The diameter of the nozzles, d_o, used in the air and water injection tests was 1.5 and 3.0 mm, respectively. The nozzles were placed at the center of the tank and their exit was 45 mm above the bottom. The experiments with water injection were limited to the square and rectangular setups to minimize the effect of increase in the water level, which was less than 1% over the duration of the experiments in both cases. These flow rates and nozzle diameters were chosen in order to provide similar velocity scales of the entrained liquid jet for the air and water injection tests.

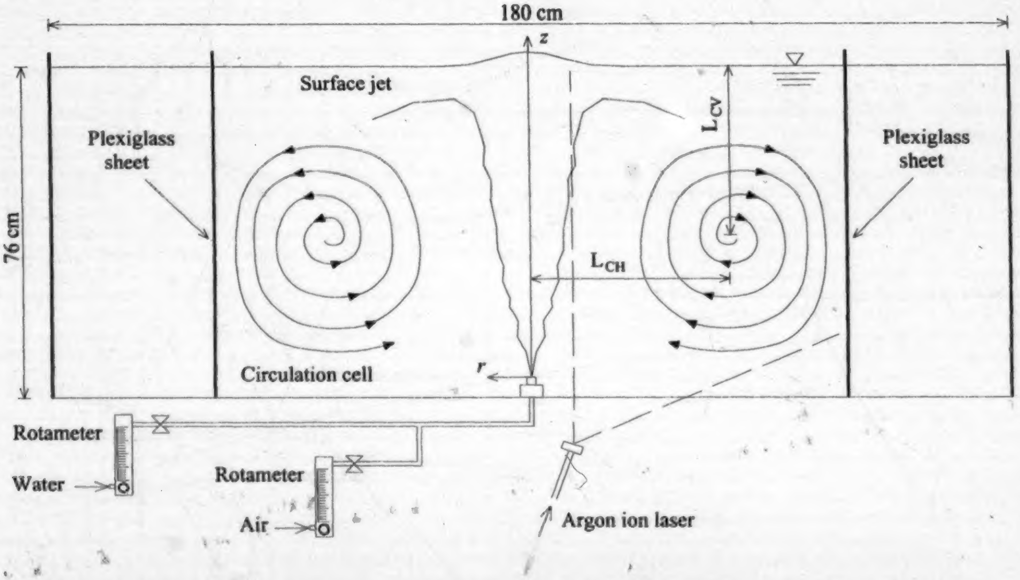

Figure 3-1. Schematic of experimental apparatus, indicating circulation flow cells at the longer side of the rectangular tank with two plexiglass sheets (for the square setup). Note that the confined setup (not shown in the figure) was obtained by placing a plexiglass box at the center of the tank.

Table 3-1 shows a summary of the experimental conditions, the Reynolds number being defined as $\mathrm{Re} = U_o d_o / \nu$, where U_o and ν are the velocity at the nozzle exit and kinematic viscosity for each phase (air or water) , respectively.

Table 3-1. Details of experimental conditions, showing centerline velocities measured with the propeller anemometer at 40 cm above the nozzle exit for the square and rectangular setups. The water depth was fixed at 0.76 m in all experiments.

	Square 1.2m x 1.2m	Rectangular 1.2m x 1.8m	Confined 0.4m x 0.4m	Air and water flow injection rates
Bubble plume d_o = 1.5mm	X	X	X	Q_o = 33.3cm^3/s, U_o = 18.9m/s, Re = 1885, $U_{c,40cm}$ = 24cm/s Q_o = 50.0cm^3/s, U_o = 28.3m/s, Re = 2831, $U_{c,40cm}$ = 32cm/s
Water jet d_o = 3.0mm	X	X		Q_o = 33.3cm^3/s, U_o = 4.7m/s, Re = 14140, $U_{c,40cm}$ = 20cm/s Q_o = 50.0cm^3/s, U_o = 7.1m/s, Re = 21231, $U_{c,40cm}$ = 29cm/s

Typical images of the bubble plumes and water jets are shown in Fig. 3-2. A spreading rate of about 20% of height is observed by injecting dye close to the nozzle exit (for bubble plumes) and at the water supply pipeline (for water jets). In the bubble plume tests, the ratio of the bubble core to entrained liquid jet diameter was about 0.6, which was within the typical range of 0.5-0.9 reported by Socolofsky (2001). Therefore, the bubble core had a spreading rate of about 12%.

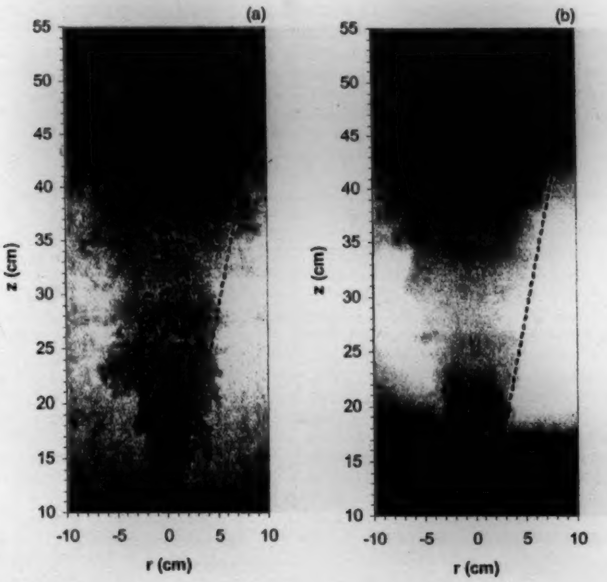

Figure 3-2. Typical images obtained using background illumination and dye injection: (a) bubble plumes and (b) water jets ($Q_o = 33.3$ cm^3/s). Dashed line indicates a 20% spreading with height.

An electromagnetic propeller anemometer (Omni Instruments, MiniWater20) with an internal diameter of 22 mm was used to measure mean vertical water velocity inside the bubble plumes and water jets in the square and rectangular setups. The measured velocities at the centerline water jet at different distances above the nozzle were about 10% smaller than those obtained by using the classical theory of free jets (see Rajaratnam, 1976). This 10% difference was was probably due to the accuracy of the propeller anemometer, as well as the assumption of the jet behaving like an ideal jet. Table 3-1 shows that although the velocity at the nozzle exit, U_o, for bubble plumes was higher than that for water jets, the centerline water velocity measured with the propeller anemometer at 0.40 m above the nozzle exit, $U_{c,40cm}$, was of the same order. The small Reynolds number, Re, in the bubble plume tests also ensured that the flow was dominated by buoyancy forces. The bubble plumes contained bubbles of mean volume equivalent-sphere diameters of about 8 mm, which were measured across the bubble core at 0.40 m above the nozzle exit using an optical probe system described by Lima Neto et al. (2006a). Visual observation of the bubble plumes and the entrained fluid (from dye injection tests) in the square and rectangular setups revealed a low-frequency oscillation of the core (wandering motion), which was smaller than that observed in the confined setup. This wandering frequency also appeared to increase with air flow rate. The water jets, however, did not present significant wandering motions.

The flow field surrounding the bubble plumes and water jets was measured using particle image velocimetry (PIV). Silver-coated glass particles with a density of 1.65 g/cm^3 and a mean diameter of 15 μm were homogenously distributed into the water. A continuous 6W argon ion laser operating at 488 nm (Stabilite 2017, Spectra-Physics Lasers) and optics (OZ optics) were used to generate a light sheet to illuminate the flow (see Fig. 3-1). Because strong 3D effects were observed in the rectangular setup for both bubble plumes and water jets, measurements were taken both in the longer and shorter planes of the tank. A high resolution CCD camera (1392 x 1040 pixels) (TM-1040, Pulnix America Inc.) controlled by a computer frame grabber system (Streams 5, IO Industries Inc.) captured 10-bit images of the particles with a resolution of 18 pixel/cm, frame rate of 30 fps, and exposure time of 1/60 s for all setups. The displacements between subsequent images were computed using a standard cross-correlation PIV algorithm (Heurisko, version 4.0.8, Aeon Verlag and Studio) with an interrogation window size of 32 x 32 pixels and 50% overlap between adjacent windows. In the confined setup, because of the wandering motion and the proximity of the PIV field of view to the bubble core centerline (7 cm), a few bubbles could be periodically observed (closer to the water surface), but this effect was considered negligible as the PIV code corrected the velocity vectors using a threshold technique. This problem was much less pronounced in the square and rectangular setups, where the frequency of the wandering was lower and the PIV field of view was located farther away from the bubble core centerline (10 cm).

The bubble plume experiments were performed for 2 and 5 min in duration, which resulted in similar flow patterns. This is consistent with preliminary bubble plume tests in the square setup conducted by Lima Neto et al. (2006a) with sampling times ranging from 5 to 30 min, which resulted in measurements of average air-phase properties (void fraction, bubble velocity and diameter) within only about 10 % difference. We decided not to exceed the 2 min duration in the water jet tests in order to minimize the effect of increasing water level in the tank.

3.3. Results and discussions

Typical horizontal velocity components, *u*, obtained from PIV measurements of the flow near the bubble plumes and water jets, and power spectrums of these velocities, G_u, are shown in Figs. 3-3 and 3-4, respectively. In Fig. 3-4, a line with a slope of -5/3 is also shown to indicate the presence of Kolmogorov's inertial subrange. A dominant frequency, *f*, of about 0.03 Hz was obtained for the velocity signals near the core of both the bubble plumes and water jets in the square and rectangular setups. The same frequency was obtained for different sampling times (2 and 5 min) and from optical probe measurements of void fraction (5 min duration) at the bubble core centerline in the square setup. Thus, the dominant frequency in the spectrum of bubble plumes will be considered here as a wandering frequency, as suggested by Rensen and Roig (2001). A dominant frequency of about 0.11 Hz was obtained for the velocity signals near the bubble core in the confined setup and it was also considered as a wandering frequency for this particular case. This is consistent with the higher wandering frequency observed visually in the confined setup. Note that these frequencies were obtained for the flow rate of 33.3 cm^3/s. For the higher flow rate used in this study (50.0 cm^3/s), these frequencies were higher, i.e. about 0.04 for the square/rectangular setups and 0.12 Hz for the confined setup. This supports the idea that these dominant frequencies corresponded to the wandering frequencies of the bubble plumes, which increased with air flow rate but decreased with tank size. It is important to mention, however, that estimation of the 95% confidence intervals in the power spectra shown in Fig. 3-4 resulted in deviations of the peak frequency by up to about 33%. In this case, the peak frequencies for 33.3 and 50.0 cm^3/s will be assumed to be of the same order. Visual observation and optical probe measurements of the bubble core oscillation also confirmed a weak influence of the air flow rate tested here on the wandering motion, as compared to that of tank size.

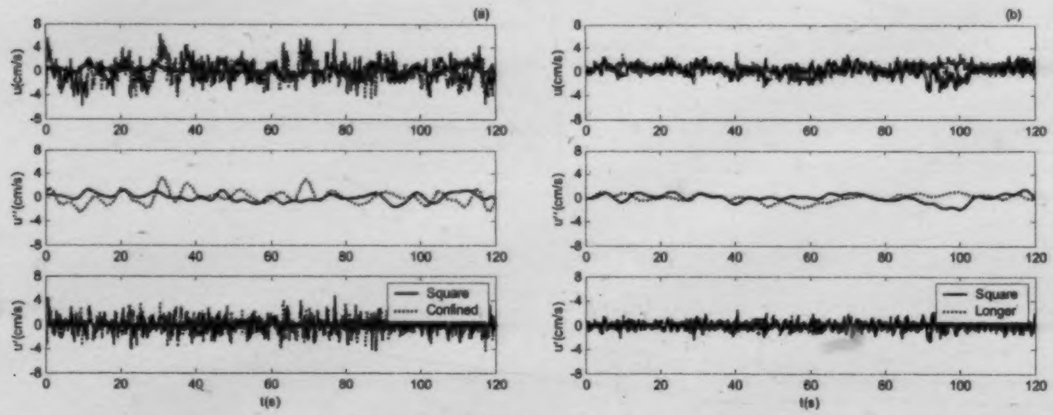

Figure 3-3. Instantaneous horizontal velocity (u) measured at $r = 15$ cm and $z = 40$ cm ($Q_o = 33.3$ cm^3/s), periodic component (u''), and turbulent component (u'), for the flow induced by (a) bubble plumes in the square and confined setups and (b) water jets in the square and rectangular (in the longer plane) setups.

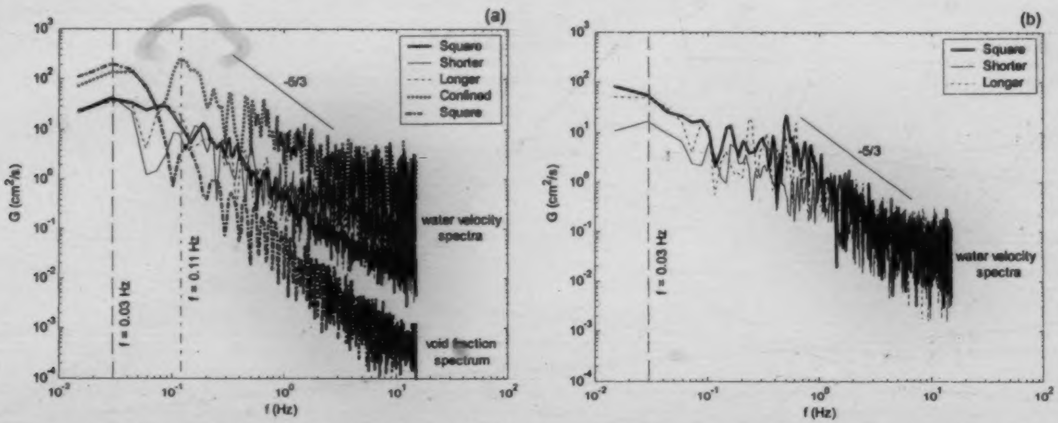

Figure 3-4. Power spectra of horizontal velocity component u measured at $r = 15$ cm and $z = 40$ cm for the square, rectangular (in both shorter and longer planes), and confined setups, indicating dominant frequencies of about 0.03 and 0.11 Hz and the presence of an inertial subrange (line with slope of -5/3): (a) bubble plumes (also indicating a void fraction spectrum for the square setup measured at $r = 0$ cm and $z = 40$ cm); (b) water jets ($Q_o = 33.3$ cm^3/s).

Because of the non-stationary nature of the flow, a digital filtering technique was used to separate the turbulent motions (i.e. high-frequency signals) and the periodic motions (i.e. low-frequency signals) from the original velocity signals. In order to define a cut-off frequency, we examined the coherence (C_{uv}) between the horizontal and vertical velocity components, estimated using the power spectra of these variables [i.e., $C_{uv} = G_{uv}^2/(G_u G_v)$]. Thus, a low coherence indicates the random (i.e., turbulent) motions while a high coherence indicates the well correlated (i.e., periodic) motions. A frequency of 0.2 Hz gave a coherence lower than about 0.3 for the high-frequency signals and a coherence higher than about 0.7 for the low-frequency signals (see Fig. 3-5). Although the limits above varied across the tank and some contamination between the turbulent and periodic motions is also expected, the use of 0.2 Hz as a cut-off frequency fitted the periodic velocity fluctuations in the instantaneous velocity time series. This is also consistent with the procedure described by García and García (2006), where a cut-off frequency higher than the dominant wandering frequency was used to decompose the velocity signals. Hence, considering this cut-off frequency, a Butterworth high-pass filters of 6th order was used to eliminate the mean velocities ($\overline{u}$ and $\overline{v}$) from the original velocity signals (u and v) and separate the dominant periodic velocity fluctuations (u'' and v'') from the turbulent velocity fluctuations (u' and v'), where $u = \overline{u} + u' + u''$ and $v = \overline{v} + v' + v''$. Examples of this velocity decomposition are shown in Fig. 3-3. It is seen that both u'' and u' in the confined setup are higher than those for the square and rectangular setups.

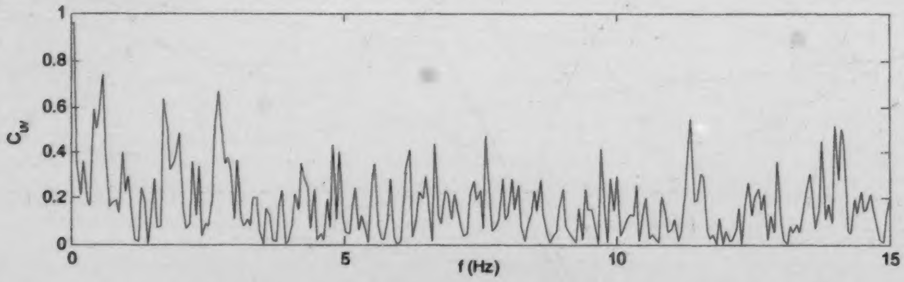

Figure 3-5. Typical coherence between the horizontal and vertical velocity components of the flow induced by bubble plumes.

To examine the effect of the tank size on the dominant frequency (or wandering frequency) induced by bubble plumes and to non-dimensionalize the results, we introduce the ratio *b*/*B*, where *b* is a length scale for the jet and plume at the free surface and *B* is the tank radius or half-width. For circular jets and plumes, *b* can be estimated as $b = 0.2\,H$ (Rajaratnam, 1976), where *H* is the travel distance of the jet and plume to the water surface. To examine the effect of the air flow rate, we introduce velocity and length scales defined by $U = Q_o/L^2$ and $L = \left(Q_o^2/g\right)^{1/5}$, respectively, as well as a densimetric Froude number defined by $Fr = U\Big/\sqrt{bg\left(\rho_w - \rho_a\right)/\rho_w}$, in which ρ_w and ρ_a are the water and air density, respectively. Thus, combining the above parameters with curve fitting of experimental data obtained here and available in the literature, a dimensionless wandering frequency can be expressed by the following equation

$$\frac{fL}{U} = Fr^{2.9}\left[0.268\log\left(\frac{b}{B}\right) + 0.205\right] \tag{3.1}$$

Figure 3-6 shows that Eq. (3.1) describes well ($r^2 = 0.994$) the experimental data and that the dimensionless wandering frequency *fL*/*U* increases as the tank size becomes small compared to the jet radius up to *b*/*B* = 0.76, where this frequency becomes independent of tank size. This is consistent with the experimental results of Rensen and Roig (2001), in which the wandering frequency was constant for *b*/*B* varying from about 0.7 to 1.8. It is interesting to note that, according to Eq. (3.1), the wandering frequency also increases with the air flow rate following approximately a power law with slope of 0.38, which is within the above-mentioned values of 0.30 and 0.50 obtained from the data given by Rensen and Roig (2001) and García and García (2006).

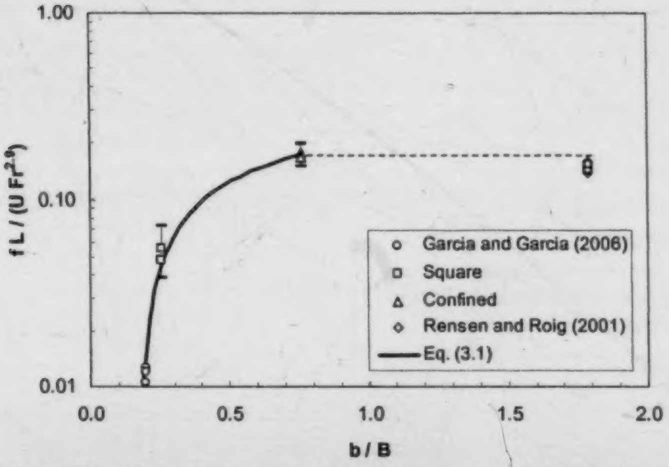

Figure 3-6. Variation of the dimensionless wandering frequency with the ratio of jet radius to tank radius (or half-width). Our data points correspond to the air flow rates Q_o of 33.3 and 50.0 cm^3/s, including the 95% confidence intervals (indicated with error bars). Dashed line indicates the region where the wandering frequency becomes independent of b/B, according to the experimental results of Rensen and Roig (2001).

The comparison shown in Fig. 3-6 is for bubble plume studies with different diffusers but similar range of bubble diameters: 3 mm (obtained from Rensen and Roig, 2001); 8 mm (obtained from the present study); and 10 mm (estimated for the coarse bubble diffuser used by García and García, 2006). Note that these bubble diameters are within the range of 1-15 mm reported by Clift et al. (1978) for ellipsoidal bubbles. Previous study by Lima Neto et al. (2006a) on bubble plumes generated using different nozzle types (including single and multiple orifices of different sizes and a porous airstone) resulted in similar wandering frequencies as obtained in the present study, even though the average bubble diameters varied from 3 to 10 mm with different nozzle types. In addition, all the data presented in Fig. 3-6 correspond to studies with diffusers occupying a small area on the bottom of the tank, which can be assumed to be point source diffusers. Therefore, we expect that Eq. (3.1) should be valid for those types of diffusers and the above-mentioned bubble sizes.

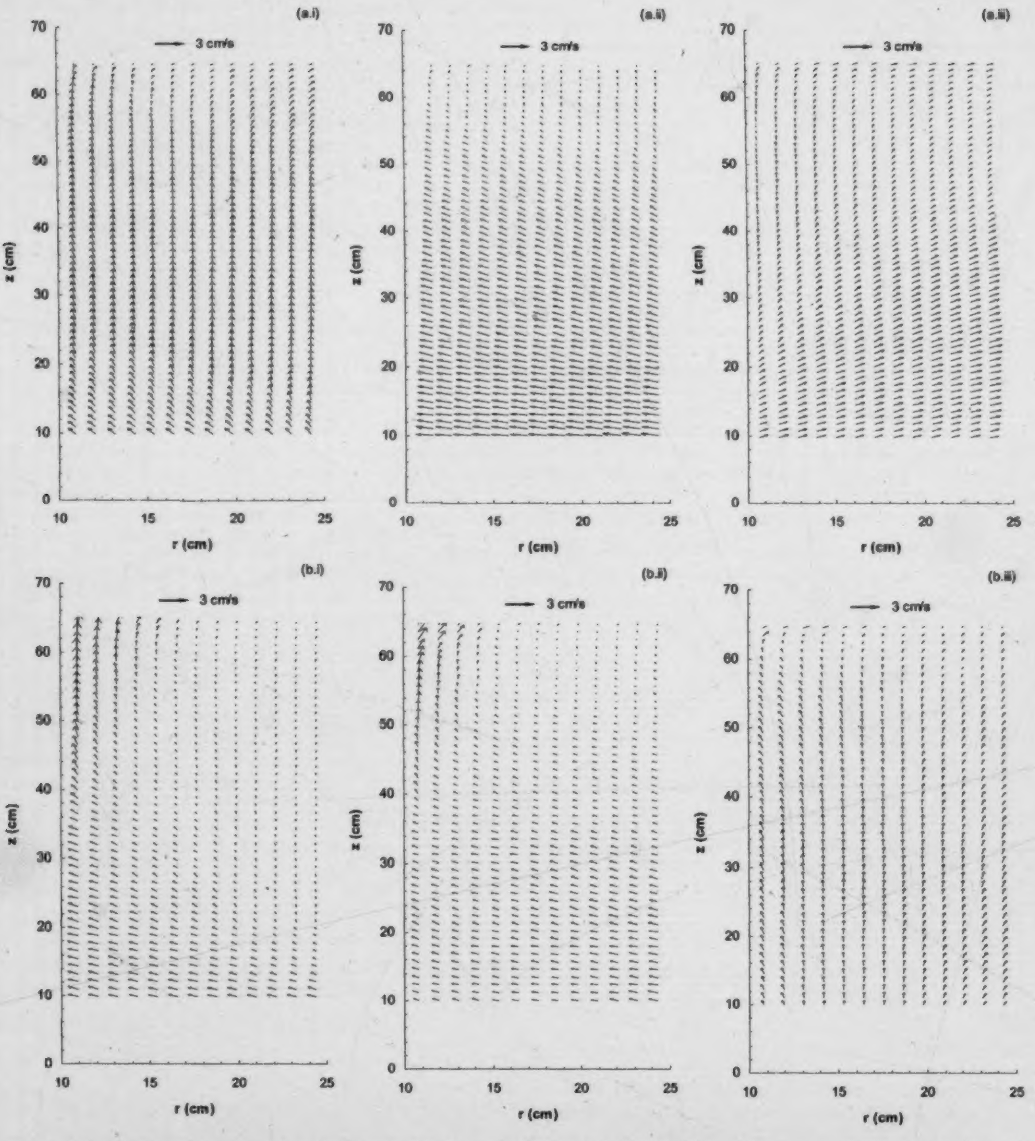

Figure 3-7. Time-averaged velocity fields surrounding the (a) bubble plumes and (b) water jets in the (i) square setup, (ii) longer and (iii) shorter planes of the rectangular setup ($Q_o = 33.3$ cm^3/s). Note that the mean vertical velocity $\overline{v}$ is distorted (about 3.5 times smaller).

Similar flow patterns surrounding the bubble plumes and water jets were obtained for both volumetric flow rates (33.3 and 50.0 cm^3/s). Typical time-averaged flow fields for the square and rectangular setups are shown in Fig. 3-7. It can be seen that the time-averaged horizontal velocity component, $\overline{u}$, decreased with height while the vertical velocity component, $\overline{v}$, increased until the flow approached the surface jet region, as observed by Fanneløp et al. (1991) and Riess and Fanneløp (1998) for line-source bubble plumes. However, in our bubble plume tests, strong 3D effects were generated in the rectangular tank, with larger water flow entraining in the longer plane and smaller water flow detraining in the shorter plane. Similar 3D effects were generated in our water jet tests, with water flow entraining in the longer plane and part of the flow entraining (up to about r = 15 cm) and then detraining in the shorter plane. This implies that the bubble plumes were more affected by the tank asymmetry than the water jets.

A time-averaged flow field for the bubble plumes in the confined setup is shown in Fig. 3-8, in which more than one circulation flow cell (vortex) was generated, in contrast with the above mentioned flow patterns for bubble plumes in the square and rectangular setups. The presence of about two vortices stacked vertically in the confined setup is consistent with the results summarized by Mudde (2005), in which the number of vertical cells is close to the aspect ratio $H/2B$ (note that in our case $H/2B = 1.9$).

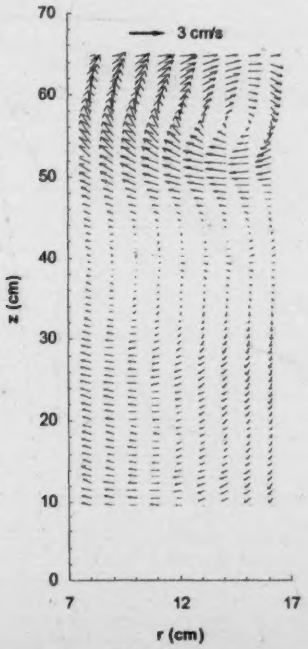

Figure 3-8. Time-averaged velocity field surrounding the bubble plumes in the confined setup (Q_o = 33.3 cm^3/s). Note that the mean vertical velocity $\overline{v}$ is distorted (about 3.5 times smaller).

Figure 3-9 shows large-circulation patterns for each plane of the square and rectangular setups in which the entraining and detraining flows are clearly represented through streamlines generated from PIV measurements. The flow patterns obtained for the bubbles plumes were similar to those obtained for the water jets, with the center of the circulation cells located approximately at the same positions. However, the center of the circulation cells in the longer plane of the rectangular setup was much closer to the water surface, while in the shorter plane it was closer to the tank bottom. Comparing these flow patterns with that shown in Fig. 3-8, we can see that both the number of cells and location of their centers varied with tank size and geometry.

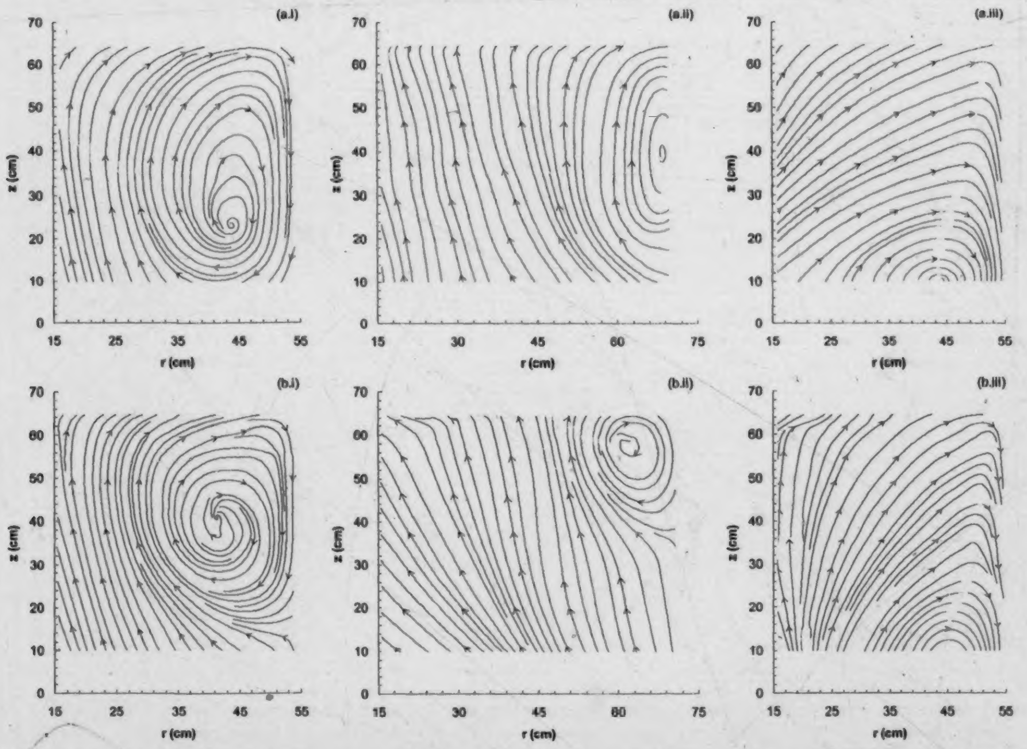

Figure 3-9. Streamlines generated from time-averaged PIV measurements for the flow surrounding the (a) bubble plumes and (b) water jets in the (i) square setup, (ii) longer and (iii) shorter planes of the rectangular setup ($Q_o = 50.0$ cm^3/s)

The presence of large-circulation flow cells surrounding the bubble plumes and water jets (see Fig. 3-9) is consistent with the length of the cells varying from about 2 to 7 times the water depth reported by Iamandi and Rouse (1969), Jirka and Harleman (1979), Fanneløp et al. (1991)

and Riess and Fanneløp (1998). This suggests that tank aspect ratios $H/2B$ lower than about 0.25 are necessary to generate more than one circulation cell in the lateral direction. Note that our aspect ratios $H/2B$ were 0.42 for the longer plane of the rectangular tank and 0.63 for both the square tank and the shorter plane of the rectangular tank, and no secondary cell was observed.

The geometry of the primary circulation cells in each setup can be estimated by the ratio L_{CV}/L_{CH}, in which L_{CV} is the vertical distance from the water surface to the center of the circulation cells and L_{CH} is the horizontal distance from the nozzle centerline to the center of the circulation cells (see Fig. 3-1). This ratio can also be interpreted as an approximate spreading of the surface jet. The values of L_{CV}/L_{CH}, obtained from Figs. 3-8 and 3-9 are plotted in Fig. 3-10 along with the values from the literature. Figure 3-10 shows that L_{CV}/L_{CH} in square and 2D tanks increases logarithmically with b/B, which means that longer cells are formed in larger tanks. The curve shown in this figure [Eq. (3.2)] was also obtained from curve fitting (r^2 = 0.964) of experimental data.

$$\frac{L_{CV}}{L_{CH}} = 0.675\log\left(\frac{b}{B}\right) + 1.419 \tag{3.2}$$

It is interesting to observe that due to 3D effects in our rectangular tank, the values of L_{CV}/L_{CH} in the shorter and longer planes were about 1.5 and 0.4 times the value of L_{CV}/L_{CH} for the square tank, respectively (see Fig. 3-9). Besides, the values of L_{CV}/L_{CH} for bubble plumes are consistently higher than those for water jets, especially for the longer plane of the rectangular setup. This difference may be attributed to larger liquid volume fluxes (and perhaps higher turbulence levels) induced by the bubble plumes than those induced by the water jets (see Table 3-1), which may have caused higher spreading of the surface jet. It is consistent with the results of Fanneløp et al. (1991), in which the primary cell length was found to be a weak function of the flow rate in their bubble plume tests and independent of the flow rate in the water jet tests. This supports the negligibility of the densimetric Froude number Fr in Eq. (3.2). A diagram with approximate limits of b/B to estimate the flow patterns of the circulation cells based on the aspect ratios mentioned above is also given in Fig. 3-10. This diagram shows that multiple horizontal cells (MHC) are formed when *b*/*B* is up to about 0.1, single cells (SC) are formed when *b*/*B* ranges from about 0.1 and 0.7, and multiple vertical cells (MVC) are formed when *b*/*B* is larger than about 0.7. This suggests that Eq. (3.2) can be used to estimate both the size and number of circulation cells in a general tank.

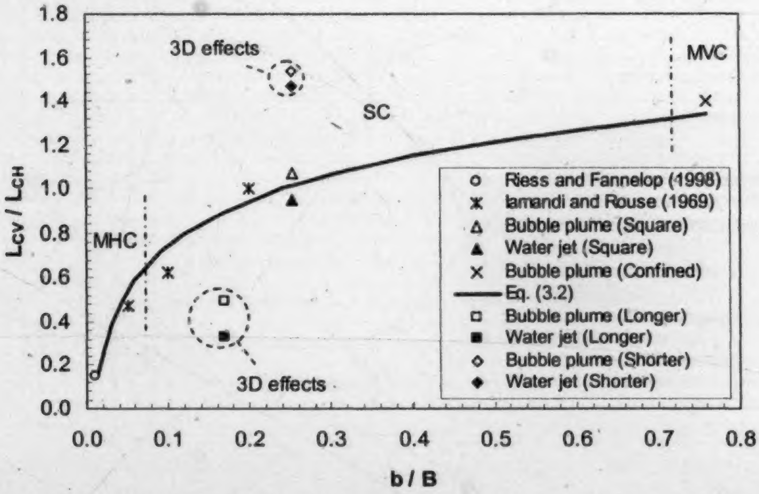

Figure 3-10. Variation of the approximate spreading of the surface jet with the ratio of jet radius to tank radius (or half-width). Note that MHC, SC and MVC correspond to the regions in which multiple horizontal cells, single cells, and multiple vertical cells are formed, respectively. Dashed circles indicate the data points obtained in the rectangular setup, where strong 3D effects were observed.

Typical distributions of the normalized turbulent stresses $\overline{u'u'}/U^2$, $\overline{v'v'}/U^2$ and $\overline{u'v'}/U^2$ with the normalized vertical distance from the nozzle *z*/*L* are shown in Fig. 3-11, in which *U* and *L* are respectively the velocity and length scales given above. Note that the results are shown for values of *z*/*L* up to 50. For higher values of *z*/*L*, the turbulence levels increased significantly as the flow approached the surface jet region (at *z*/*L* = 60). It can be seen that the horizontal normal stresses, $\overline{u'u'}/U^2$, were of the same order of the vertical normal stresses, $\overline{v'v'}/U^2$, and that the shear stresses, $\overline{u'v'}/U^2$, were much smaller than those, which implies that the turbulent flow field was nearly isotropic for all experiments. The turbulent stresses in the bubble plume tests were more affected by the tank geometry than those in the water jet tests. For example, in the bubble plume tests, the values of $\overline{v'v'}/U^2$ for the shorter plane of the rectangular setup were about 2 times larger than those for the longer plane, while in the water jet tests, the values were of the same order. The magnitude of the turbulent stresses for the bubble plumes in the square and rectangular setups was slightly higher than that for water jets. On the other hand, the magnitude of the turbulent stresses for bubble plumes in the confined setup was about 3 times higher than that in the square and rectangular setups due to the effect of the recirculation eddies. Moreover, these stresses did not decay with the inverse of axial distance, as expected for the turbulent stresses inside single-phase jets (see Rajaratnam, 1976). The axial variation of the terms $\overline{u^{\cdot}u^{\cdot}}$, $\overline{v^{\cdot}v^{\cdot}}$ and $\overline{u^{\cdot}v^{\cdot}}$, called here as periodic stresses, followed similar trends as those of turbulent stresses for both bubble plumes and water jets, but their magnitude was approximately twice as high.

An examination of the velocity signals in the entire tank (away from the jet/plume region) revealed that the periodic fluctuations were distributed approximately uniformly across the tank but their strength increased about one order of magnitude as the flow approached the center of the circulation cells. This behavior was similar for bubble plume and water jet tests. The flow fields at different times showed that the circulation cells traveled basically up and down within a distance of up to about 10 and 20% of water depth for the water jet and bubble plume tests, respectively. This was probably the cause of the wandering motions described by Eq. (3.1). The turbulent stresses were also distributed approximately uniformly across the tank. Nearly isotropic turbulence was obtained in the entire tank, with horizontal and vertical normal stresses within about 20% difference. Note that our measurements were limited to a distance of at least 4 cm from the walls.

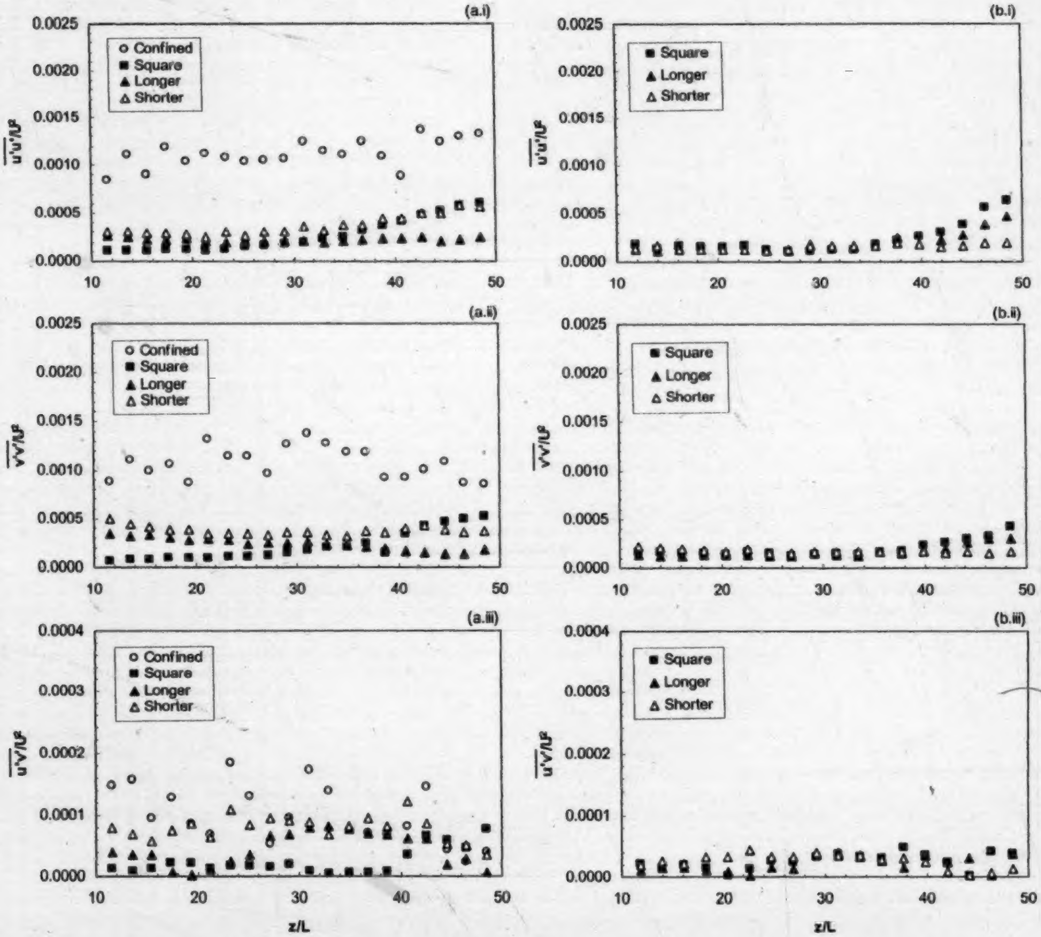

Figure 3-11. Typical axial variation of the normalized turbulent stresses measured at r = 15 cm (Q_o = 33.3 cm^3/s) for (a) bubble plumes and (b) water jets: (i) horizontal normal stresses, (ii) vertical normal stresses, and (iii) shear stresses.

3.4. Summary and conclusions

An experimental study was conducted to investigate the effect of tank size and geometry on the ambient flow field and circulation patterns induced by circular bubble plumes and water jets. The results revealed a non-stationary nature of the flow for all experiments, which was attributed mainly to the presence of coherent structures instead of buoyancy-driven instabilities. The wandering frequency of the bubble plumes was assumed to be equal to the dominant frequency of the velocity oscillations near the bubble core. This frequency was found to increase with air flow rate and to decrease with tank size, and a correlation based on our measurements and results available in the literature was proposed to describe this variation.

The mean flow patterns clearly changed with tank geometry. While multiple vortices were stacked vertically for bubble plumes in the confined setup, a large-circulation flow cell surrounding the bubble plumes and water jets was generated in both the square and rectangular setups, but the latter produced strong 3D effects with larger flow entraining in the longer plane of the rectangular setup and smaller flow detraining in the shorter plane. These 3D effects were more pronounced in the bubble plume tests than in the water jet tests. A parameter corresponding to the spreading of the surface jet was introduced to describe the geometry of the circulation cells. This parameter was found to increase as the tank size became small compared to the radius of the jets and plumes, and a correlation was obtained to describe the flow patterns of the circulation cells as a function of tank size.

Nearly isotropic turbulent flow conditions were obtained in all experiments. However, the effect of tank size and geometry on the intensity of the turbulent stresses was more pronounced in the bubble plume tests. Besides, the axial variation of the turbulent and periodic stresses followed similar trends, but their magnitude was higher for bubble plumes in the confined setup than that in the square and rectangular setups because of the effect of the recirculation eddies.

The above results describe the ambient flow field and circulation patterns induced by bubble plumes and water jets, which are important in many engineering applications, including lake and reservoir aeration, mixing in wastewater treatment tanks, and prevention of suspended solids settling. It should be pointed out, however, that there are still a few important questions remaining. Our results imply that the wandering motion observed visually in the bubble plume experiments was caused mainly due to vertical oscillations in the position of the large circulation cells (instead of buoyancy-driven instabilities). The reason water jets are less susceptible to wandering motion is not clear, possibly due to much higher momentum flux in water jets. The reason for the 3D effects observed in the longer and shorter planes of the rectangular tank is also an open question. One possible explanation for such effects is the presence of secondary flows in the tank, as the surface jet in the shorter plane reaches the tank walls with higher velocity than that in the longer plane. Possible imbalanced Reynolds stresses and non-uniform distributions of shear stresses at the wall may also play an important role. Further research is needed to answer the above questions.

3.5. Notation

The following symbols are used in this chapter:

d_o = nozzle diameter (mm)

Q_a = volumetric air flow rate (cm^3/s)

Q_w = volumetric water flow rate (cm^3/s)

Re = Reynolds number defined as $\mathrm{Re} = U_o d_o / \nu$

r = radial distance from the plume centerline (cm)

U_o = velocity at the nozzle exit for each phase (air or water) (m/s)

$\bar{u}$ = time-averaged horizontal velocity component (cm/s)

u' = turbulent horizontal velocity fluctuation (cm/s)

$u^{\bullet}$ = periodic horizontal velocity fluctuation (cm/s)

$\overline{u'u'}$ = horizontal normal stress due to turbulent fluctuations (cm^2/s^2)

$\overline{u^{\bullet}u^{\bullet}}$ = horizontal normal stress due to periodic fluctuations (cm^2/s^2)

$\overline{u'v'}$ = shear stress due to turbulent fluctuations (cm^2/s^2)

$\overline{u^{\bullet}v^{\bullet}}$ = shear stress due to periodic fluctuations (cm^2/s^2)

$\bar{v}$ = time-averaged vertical velocity component (cm/s)

v' = turbulent vertical velocity fluctuation (cm/s)

v° = periodic vertical velocity fluctuation (cm/s)

$\overline{v'v'}$ = vertical normal stress due to turbulent fluctuations (cm^2/s^2)

$\overline{v^{\circ}v^{\circ}}$ = vertical normal stress due to periodic fluctuations (cm^2/s^2)

z = axial distance from the nozzle exit (cm)

ν = kinematic viscosity of each phase (air or water) (m^2/s)

Chapter 4

Air Injection in Water with Different Nozzles[*]

4.1. Introduction

Bubble plumes are widely used for artificial aeration and mixing in lakes, reservoirs and wastewater treatment systems (Wüest et al., 1992; McCord et al., 2000; McGinnis and Little, 2002; DeMoyer et al., 2003, McGinnis et al., 2004; Sahoo and Luketina, 2006). These types of two-phase flows are formed when air or pure oxygen is continuously discharged into the water, producing bubbles that rise inducing surrounding liquid entrainment and oxygen transfer to the water. The size of the rising bubbles depends on bubble breakup/coalescence processes (which depend on several factors such as turbulence, bubble collision frequency, presence of impurities, and so forth) and the counterbalancing effects of mass transfer and reducing pressure head acting on the bubble surface. Two important parameters that are controlled by the sizes of the bubbles are the mass transfer coefficient or liquid film coefficient, K_L, and the air-water interfacial area per unit liquid volume or specific interfacial area, a. These parameters are related to the rate of oxygen transfer to the water through the following equation, derived from Fick's law of diffusion (Mueller et al., 2002)

$$\frac{dC}{dt} = K_L a(C_s - C) \tag{4.1}$$

where C is the dissolved oxygen (DO) concentration in the water and C_s is the saturation DO concentration. Correction factors for K_L and C_s to account for the effects of water temperature, pressure and presence of impurities are commonly used in wastewater aeration systems (see Mueller et al., 2002). While the mass transfer coefficient K_L increases with bubble diameter, reaching a maximum of approximately 0.05 cm/s for bubbles of about 2 mm and then decreasing as the diameter increases (Barnhart, 1969; Montarjemi and Jameson, 1978), the specific interfacial area *a* decreases significantly as the mean bubble diameter increases. The sizes of the bubbles also determine their shape and velocity (Clift et al., 1978), which in return affect their residence time in the water and, as a consequence, the rate of oxygen transfer to the water. An experimental study conducted by Leitch and Baines (1989) on dilute bubble plumes also showed that bubble size affects the surrounding flow structure because the individual bubble wakes play an important role on the liquid entrainment rate. Additional liquid turbulence caused by the wakes of the bubbles and bubble collision processes has also been observed recently by Brücker and Schröder (2004).

---

[*] A paper based on the content of this chapter has been submitted for publication in the Journal of Environmental Engineering, ASCE, as Lima Neto et al. (2006a).

In artificial aeration systems, oxygen transfer to the water also occurs during bubble formation at the orifices and bubble bursting at the free surface. In principle, the oxygen transfer rate for each of these processes could also be described as a function of a mass transfer coefficient, interfacial area and DO concentration deficit (Eckenfelder, 1959; Barnhart, 1969), as mentioned above for rising bubbles [see Eq. (4.1)]. However, the complexity of these processes complicates the estimation of the mass transfer coefficient and interfacial area. Following the methods of McWhirter and Hutter (1989) and DeMoyer et al. (2003), Schierholz et al. (2006) used measurements of DO concentrations in several aeration tanks of different scales and performed a regression analysis to separate the contributions of oxygen transfer to the water from the bubbles and across the air-water surface. They reported that for relatively high air flow rates, fine bubble diffusers are better for bubble aeration while coarse bubble diffusers are more suitable for surface aeration. They also proposed correlations for bubble and surface volumetric mass transfer coefficients (K_La). A summary of standard measurement methods to estimate the total value of K_La through regression analysis in aeration systems is given in a recent ASCE Standard - ASCE/EWRI 2-06 (2007). On the other hand, in the case of point-source bubble plumes in lakes or reservoirs with much larger free surface areas, additional oxygen transfer will occur through turbulent diffusion at the water surface due to the effects of circulation water flow and wind stream (see McCord et al., 2000). Several equations of K_L for each of these effects are summarized by Chu and Jirka (2003) and Lima Neto et al. (2006b).

Sufficient circulation and mixing is also required in artificial aeration systems to disperse DO and provide uniform organic matter concentrations throughout the water. Due to the difficulty in measuring flow patterns for a particular aeration system, limited information on circulation and mixing characteristics is available and usually a velocity of about 0.15 m/s across the basin bottom is assumed to prevent solids deposition in degritted wastewater tanks (WPCF, 1988; Mueller et al., 2002). Soga and Rehmann (2004), Wain and Rehmann (2005) and García and García (2006) recently conducted measurements of turbulence in the flow field surrounding a bubble plume for aeration and mixing in a wastewater tank to prevent anaerobic conditions. These measurements will help to evaluate the mixing requirements and associated transport processes induced by a bubble plume.

Despite the importance of bubble properties and mean-turbulent liquid flow structure on the performance of aeration/mixing systems and their designs, very few studies have devoted into this issue. In addition to bulk dissolved oxygen (DO) measurements, Rosso and Stenstrom (2006) roughly estimated average bubble size and velocity in a relatively small aeration tank (with diameter smaller than 40 cm), but no detailed information such as bubble size distribution, bubble slip velocity, interfacial area and liquid flow structure were provided. The studies mentioned above were conducted for diffusers occupying a large area on the bottom of the tank (partial or total floor coverage). The case of point source discharges have been studied by Kobus (1968), Iguchi et al. (1989, 1992), Swan and Moros (1993), Friedl and Fanneløp (2000), Soga and Rehmann (2004), Wain and Rehmann (2005) and García and García (2006). Among these studies, only Iguchi et al. (1989, 1992) investigated the effect of single orifice nozzle diameter on bubble properties and mean-turbulent liquid flow structure. However, their experiments were conducted in small scale vessels (or confined setups) where the flow behaves differently from unbounded bubble plumes away from the boundaries (see Lima Neto et al., 2007b).

Therefore, the aim of the present work was to investigate experimentally the effect of different nozzles, including single/multiple orifice nozzles and a porous airstone, on the characteristics of the bubbles such as bubble size, velocity and interfacial area as well as the mean-turbulent liquid flow structure generated in a relatively large water tank. The results of this study are applicable to shallow water cases such as artificial aeration/mixing in wastewater tanks (Mueller et al., 2002) and rivers (Lima Neto et al., 2006b) and provide information for initial conditions in bubble plume models.

4.2. Experimental apparatus and program

The experiments were performed in a square glass-walled tank of 1.2 m with a height of 0.8 m, shown schematically in Fig. 4-1. The tank was filled with tap water at 20 ± 1°C up to a depth of 0.76 m. The gas supply was taken from an air line with 1.0 atmosphere pressure and temperature of 21 ± 1°C. Volumetric air flow rates, Q_a, of 33.3 and 50.0 cm^3/s were adjusted by a rotameter and discharged through different nozzles (single/multiple orifice nozzles and a porous airstone), connected by a PVC pipe with inner diameter of 2.54 cm. These air flow rates were chosen because preliminary dye injection tests showed that for smaller values (Q_a = 16.7 cm^3/s), the flow behaves like weak bubble plumes with the entrained liquid spreading approximately with the square-root of height, while for higher values (Q_a = 33.3 and 50.0 cm^3/s), the entrained liquid spreads linearly with height, as expected for larger-scale bubble plumes (see Leitch and Baines, 1989). Higher air flow rates (Q_a = 66.7 cm^3/s) were not considered here because the flow became very unstable with strong surface waves being reflected from the walls of the tank. As sketched in Fig. 4-2, the single/multiple orifice nozzles were built from PVC caps where circular holes of different sizes were drilled, while the porous nozzle was built by drilling a circular hole of 6 mm diameter on a PVC cap and gluing a porous airstone on its top. The nozzles of 1 x 3.0 mm, 4 x 1.5 mm and 9 x 1.0 mm were design such that the total orifice area remains the same, the single-orifice nozzle of 0.6 mm and the porous airstone being special cases. The sizes of the orifices used here were similar to those usually employed in fine and intermediate bubble diffuser systems, which range from about 0.1 to 5.0 mm (Mueller et al., 2002). The nozzles were placed at the center of the tank and their exit was about 4.5 cm above the bottom. Experiments with each nozzle and flow rate (see Table 4-1) were performed separately for optical probe tests and particle image velocimetry (PIV) tests, which are described in the following sections.

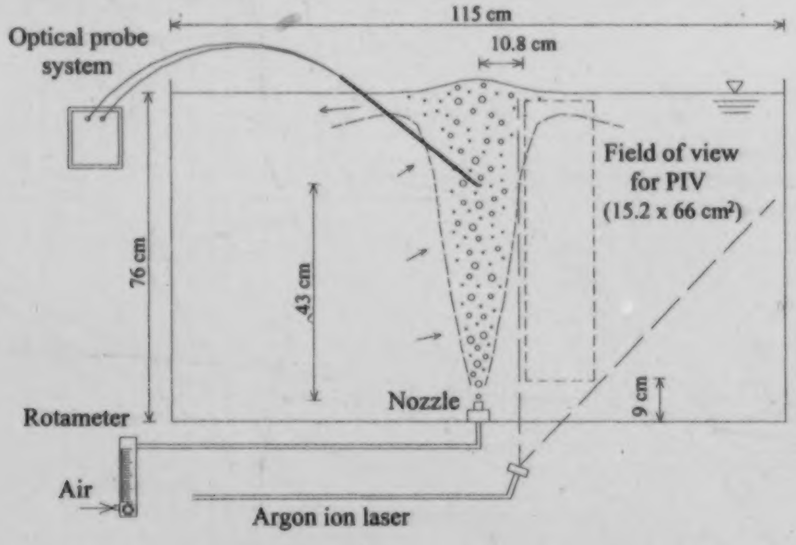
115 cm
10.8 cm
Optical probe system
Field of view for PIV (15.2 x 66 cm^2)
76 cm
43 cm
9 cm
Nozzle
Rotameter
Air
Argon ion laser

Figure 4-1. Schematic of experimental apparatus.

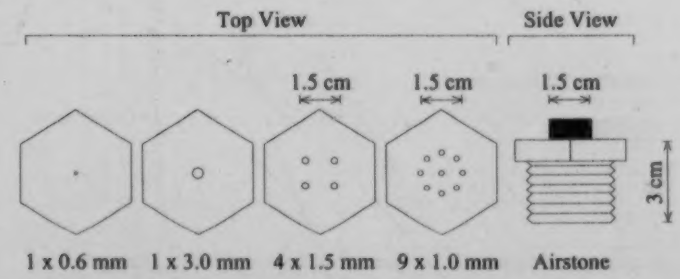
Top View
Side View
1.5 cm
1.5 cm
1.5 cm
3 cm
1 x 0.6 mm
1 x 3.0 mm
4 x 1.5 mm
9 x 1.0 mm
Airstone

Figure 4-2. Sketch of the nozzle types, indicating number and diameter of the orifices (top view) and the porous airstone nozzle (side view)

Table 4-1. Estimated volumetric mass transfer coefficients ($K_L a$) for each experimental condition. The values of K_L were obtained from the correlation given by Wüest et al. (1992) and McGinnis and Little (2002) as a function of the mean bubble diameter.

	Estimated values of $K_L a$ (h^{-1})	
Nozzle	$Q_a = 33.3$ cm^3/s	$Q_a = 50.0$ cm^3/s
1x0.6mm	12.34	15.91
1x3.0mm	8.65	11.77
4x1.5mm	11.04	13.83
9x1.0mm	13.88	15.79
Airstone	18.96	19.16

4.2.1. Optical Probe Tests

In the study, a double-tip optical fiber probe system (RBI Instrumentation) was used to measure bubble characteristics. The system is described as following: A module emits infrared light via two fiber-optic cables to the tips of the probe, 2 mm apart. Each tip extends 1.5 cm and is sharpened into a 30 μm diameter. Emitted light is refracted when water surrounds the tips, and reflected back to the module when air surrounds the tips. The reflected light passes through a semi-transparent mirror combined with a prism towards a photo-sensitive diode in the module, and can be recorded at a sampling rate of 1 MHz. Finally, direct amplification and detection through a threshold technique results in a two-state signal corresponding to the phase (air or water) surrounding the tips. Thus, the double-tip optical fiber probe can measure not only void fraction and bubble frequency but also estimate through cross-correlation the velocity in which a bubble travels from one tip to the other. Similar RBI double-tip optical fiber probe systems were used by Rensen and Roig (2001), Boes and Hager (2003), Kiambi et al. (2003), Chaumat et al. (2005) and Murzyn et al. (2005) to measure two-phase flow characteristics in bubbly flows.

The optical probe signals were processed to calculate void fraction (α), bubble frequency (f_b) and velocity (u_b). The following equations given by Chanson (2002) were used to estimate the specific interfacial area (a) and bubble mean Sauter diameter (d_b):

$$a = 4f_b/u_b \tag{4.2}$$

$$d_b = 6\alpha/a \tag{4.3}$$

Since Eqs. (4.2) and (4.3) assume that the bubbles are spherical and their motion is unidirectional, which does not often occur in artificial aeration/mixing systems, we conducted two preliminary tests to verify the accuracy of the optical probe measurements. The first test was performed in a bubble column of 5 cm diameter filled with tap water up to 68 cm, as shown schematically in Fig. 4-3. Air was injected from the bottom at different flow rates through the porous airstone, and the void fraction was obtained using the optical probe and measuring the additional water level due to the presence of the bubbles (see Chang et al., 2003). The results showed that the optical probe underestimates the void-fraction by about 11%, which is in agreement with the differences of up to 14% obtained by Kiambi et al. (2003) by comparing double optical probe measurements and image processing. The second test was performed in the tank (see Fig. 4-1) where air was injected at low flow rates through different nozzles to produce dilute bubble plumes containing bubbles ranging from about 2 to 10 mm volume-equivalent sphere diameter, as shown in Fig. 4-4. In this case the optical probe was placed in the horizontal position with the tips 2 mm apart in the vertical direction to measure both bubble rising velocity and size. Images of these bubbles were then acquired using a high resolution CCD camera (TM-1040, Pulnix America Inc.) controlled by a computer frame grabber system (Streams 5, IO Industries Inc.) with a frame rate of 30 fps and exposure time of 1/4000 s. The results showed that the optical probes overestimate the bubble velocity by about 29% and underestimate the bubble size by about 10%. Similar results were obtained by Chaumat et al. (2005), who tested vertical bubbly flows with bubble size ranging from about 6 to 9 mm and obtained overestimations of bubble velocity of up to 32% and underestimations of bubble size of up to 20%.

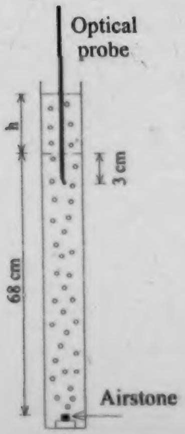

Figure 4-3. Bubble column tests to validate measurements of void fraction.

Figure 4-4. Tests to validate measurements of bubble size and velocity using the optical probe system: (a) small bubbles, (b) intermediate bubbles and (c) large bubbles (Note: distance between the tips of the probe is 2 mm).

Additional preliminary tests conducted in the tank with Q_a equals to 33.3 and 50.0 cm^3/s clearly showed a low-frequency lateral oscillation of the bubble core of about ± 5°. This non-stationary nature of the flow, usually called wandering motion, persisted even for long-time observations (> 3 h) and it was attributed to buoyancy driven instabilities enhanced by the presence of the tank walls. Similar instabilities were previously reported in bubble plume experiments (Leitch and Baines, 1989; Fanneløp et al., 1991; García and García, 2006). In order to obtain stable measurements, tests were performed for sampling times ranging from 2 to 30 min. The results showed that 5 min was enough to obtain measurements of bubble characteristics within less than about ± 10% difference. Therefore, all the bubble plume experiments were performed for 5 min duration. The measurements were taken for radial distances from the plume centerline r of 0, 2, 4 and 6 cm and at a height above the nozzle exit z of 43 cm, which was far enough for the bubble breakup/coalescence processes to be completed. The measurements were taken 5 min after start of air injection in the tank and the time interval between successive experiments was at least 20 min to ensure that the motion induced in the preceding experiment ceased completely. Figure 4-5 shows typical images of the bubbles in which bubble breakup occurs from approximately 10 to 25 cm above the nozzle exit. Bubble breakup processes were more evident for single orifice nozzles, where larger irregular bubbles were formed close to the nozzle exit due to coalescence and collapsed into much smaller spherical and ellipsoidal bubbles due to velocity gradients and turbulence. This is in contrast to the tests with multiple orifice nozzles and the airstone, where most bubbles formed at the nozzle exit were ellipsoidal and with approximately the same size.

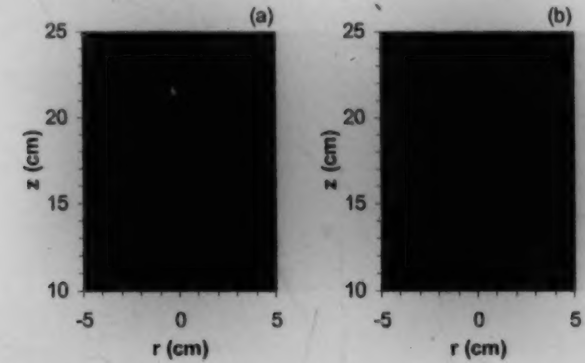

Figure 4-5. Typical images of the bubbles for $Q_a = 50.0$ cm^3/s: (a) single orifice nozzle of 0.6 mm (showing breakup of large bubbles into smaller bubbles); (b) multiple orifice nozzle of 9 x 1.0 mm (showing almost no bubble breakup).

4.2.2. PIV Tests

The time criteria used for the optical probe tests were also applied for the PIV tests. In these tests, silver coated-glass particles with a density of 1.65 g/cm^3 and a mean diameter of 15 μm were homogenously distributed over the tank. A continuous 6W argon ion laser operating at 488 nm (Stabilite 2017, Spectra-Physics Lasers) connected by a fiber-optic cable to a cylindrical lens (OZ Optics Ltd.) illuminated a field of view of 15.2 x 66 cm^2, 4.5 cm above the nozzle exit and 10.8 cm from the nozzle centerline (see Fig. 4-1). A high resolution CCD camera (Pulnix TM-1040) controlled by a computer frame grabber system (Streams 5, I. O. Industries Inc.) captured images of the particles with a frame rate of 30 fps and exposure time of 1/60 s. The field of view corresponded to an image size of 240 x 1040 pixels, yielding a resolution of 15.8 pixels/cm. The displacements between subsequent images were computed using a standard cross-correlation PIV algorithm (Heurisko, version 4.0.8, Aeon Verlag and Studio) with an interrogation window size of 64 x 64 pixels and 50% overlap between adjacent windows.

Because of the non-stationary nature of the flow mentioned above, a digital filtering technique was used to separate the turbulent motions (i.e. high-frequency signals) and the periodic motions (i.e. low-frequency signals) from the original velocity signals, and the mean-turbulent velocity components at each point were then computed using a computer algorithm written in Matlab (The Mathworks Inc.).

Measurements of the flow field within the bubble core were not possible with PIV because the bubbles were much bigger and brighter than the tracer particles and the intensity of the light reflected from them saturated the camera and corrupted the results. However, an electromagnetic propeller anemometer (Omni Instruments, MiniWater20) with internal diameter and casing of 22 and 28 mm, respectively, was used to measure mean vertical water velocity inside the bubble core. The anemometer is suitable for velocities higher than 2 cm/s with an accuracy of 2%. These measurements were taken when the bubble plumes were in a straight vertical position and were used to estimate the relative velocity between the bubbles and the water (i.e., bubble slip velocity). Similar propeller anemometers have been used in bubble plume studies by Swan and Moros (1993), Riess and Fanneløp (1998) and Friedl and Fanneløp (2000).

It is important to stress that both optical probe and PIV tests were performed on tap water with negligible suspended solids concentration. However, if a relatively large amount of suspended solids is added to the water, the refractive index of the mixture will be close to that of the air phase and corrupt the optical probe measurements (see Boyer et al., 2002). The presence of suspended solids in the water will also affect the PIV measurements. The images of suspended solids need to be separated from those of tracer particles either by using fluorescent tracer particles or by size and geometry separation (see Kiger and Pan, 2000). Note that in our PIV tests, the weight concentration of tracer particles was so small (less than 0.001 %) that their interactions with the bubbles were considered negligible.

4.3. Experimental results and analysis

4.3.1. Bubble Characteristics

The time series of void fraction indicated a low-frequency periodic fluctuation about the mean value of about 0.03 Hz, corresponding approximately to the lateral oscillation of the bubble core. Figure 4-6 shows typical void fraction time series measured with the two fiber-optic tips of the RBI probe. The time-averaged radial distributions of all void fraction (and bubble frequency) measurements followed Gaussian curves similar to those obtained by Swan and Moros (1993) and Friedl and Fanneløp (2000). Our discussion will focus, however, on the time-averaged radial distributions of bubble mean Sauter diameter, velocity and specific interfacial area, which are considered of major importance in artificial aeration systems. Figure 4-7 shows typical bubble size distributions obtained from measurements at the plume centerline. These distributions resemble gamma or lognormal curves with more uniform bubble sizes (narrower band) as the number of orifices increases and their size decreases. Figure 4-8 shows typical radial distributions of mean Sauter diameter, velocity and specific interfacial area. It can be seen that while the bubble mean Sauter diameter and velocity distributions are well described by a straight line, the specific interfacial area distribution follows a Gaussian curve.

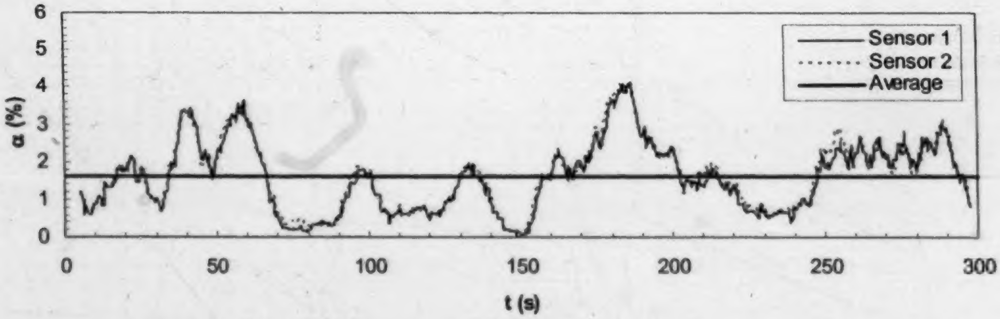

Figure 4-6. Typical void fraction time series for the two fiber-optic tips of the RBI probe: measurements taken at $r = 2$ cm and $z = 43$ cm (nozzle type: 4 x 1.5 mm, $Q_a = 50.0$ cm^3/s)

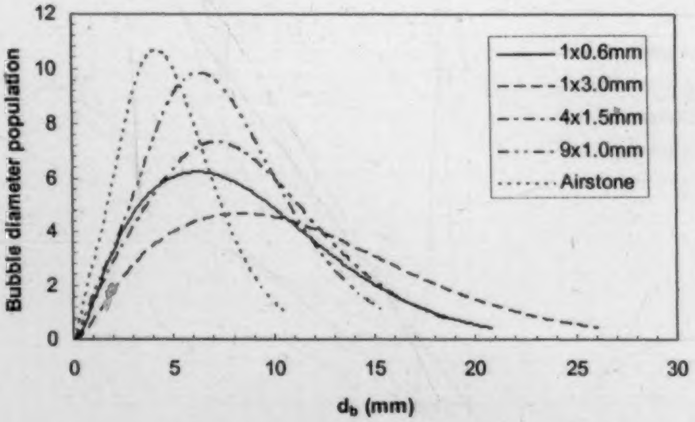

Figure 4-7. Typical bubble size distributions obtained from measurements at $r = 0$ cm and $z = 43$ cm ($Q_a = 33.3$ cm^3/s)

As the bubble velocity is the combination of the water velocity and the bubble slip velocity, the water velocity within the plume was measured using the Omni anemometer. Figure 4-8(b) shows that the water velocity decreased linearly from the maximum at the centre of the plume to close to zero at the edge of the plume. In addition, the bubble slip velocity was about 0.55 m/s, which is higher than the terminal bubble velocity of about 0.30 m/s given by Clift et al. (1978) for isolated bubbles of similar diameters. This may be because trailing bubbles in the wake of leading bubbles rise faster than isolated bubbles due to drag reduction, as observed by Ruzicka (2000). These measurements are important because bubble plume models accounting for oxygen transfer to the water usually assume uniform distributions (top-hat) of bubble characteristics, as well as constant slip velocities equal to the terminal bubble velocities given by Clift et al. (see Wüest et al., 1992).

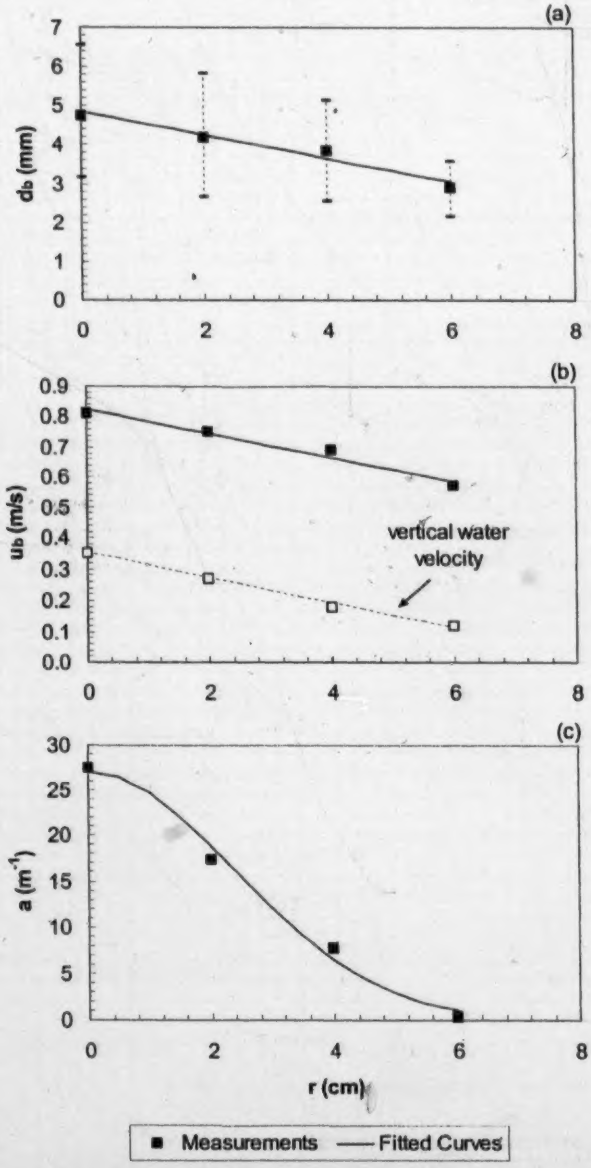

Figure 4-8. Typical radial distributions of: (a) bubble mean Sauter diameter (also indicating standard deviations); (b) absolute bubble velocity (also indicating mean vertical water velocity); and (c) specific interfacial area (nozzle type: Airstone, $Q_a = 33.3$ cm^3/s). Measurements shown were taken at $z = 43$ cm.

Figure 4-9 summarizes the average radial values of bubble mean Sauter diameter ($\overline{d_b}$), absolute bubble velocity ($\overline{u_b}$) and specific interfacial area ($\overline{a}$) for each experimental condition. It can be seen that, bubble mean Sauter diameter could be decreased by about 50% while interfacial area could be increased by about 90% by using the porous airstone instead of the single orifice nozzle of 3.0 mm. On the other hand, absolute bubble velocity did not change substantially, as observed by Iguchi et al. (1989, 1992) in a confined bubble plume setup. However, their values were about 30 % smaller than those obtained here for similar air flow rates and orifice diameters. This may be attributed to smaller bubbles due to stronger breakup processes in their confined setup as well as lower liquid entrainment rate, which will be discussed further in this paper. The results of bubble mean Sauter diameter and interfacial area for the multiple orifice nozzle of 9 x 1.0 mm are comparable to those for the airstone. This means that for systems susceptible to rapid clogging, such as porous nozzles in wastewater treatment tanks and natural water bodies with high concentration of suspended solids and/or organic matter, the use of multiple small-orifice nozzles may be preferrable rather to the use of porous airstones. Note that our porous airstone clogged after some tests and needed cleaning to reduce the friction head losses and achieve the desired air flow rates. The results for the single orifice nozzle of 0.6 mm were similar to those of the multiple-orifice nozzle of 9 x 1.0 mm, but the latter produced bubbles of more uniform size (see Fig. 4-7). The single orifice nozzle of 0.6 mm presented some advantage over the single orifice nozzle of 3.0 mm and the multiple-orifice nozzle of 4 x 1.5 mm because the high-velocity jet issuing from its exit produced more bubbles of smaller size due to very strong bubble breakup processes (especially for the higher air flow rate).

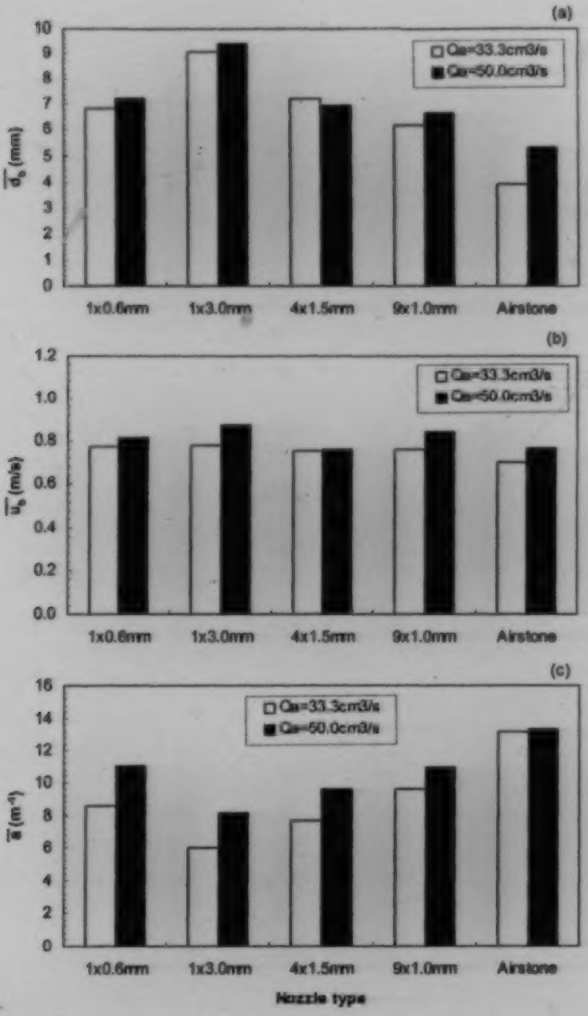

Figure 4-9. Average radial values of: (a) bubble mean Sauter diameter; (b) absolute bubble velocity; and (c) specific interfacial area. Measurements shown were taken at $z = 43$ cm.

In order to normalize the results and make them applicable to other bubble plume conditions, dimensional analysis was conducted. Using the Buckingham's Pi theorem and assuming that the forces due to viscosity, surface tension and compressibility are negligible compared to the forces due to momentum and buoyancy, under fully turbulent flow conditions in a shallow water tank, the radial distributions of d_b, u_b and a for a specific height above the nozzle can be described by the following relation

$$\left[\frac{d_b}{L},\frac{u_b}{U},aL\right]=f\left[\frac{r}{L},Fr\right] \tag{4.4}$$

where L is a length scale defined by $L=\left(Q_a^2/g\right)^{1/5}$ and U is a velocity scale defined by $U=Q_a/L^2$. The third parameter Fr is a densimetric Froude number defined by $Fr=U_e\Big/\sqrt{d_e g\left(\rho_w-\rho_a\right)/\rho_w}$, in which ρ_w and ρ_a are the water and air density, respectively, and U_e and d_e are an equivalent velocity and diameter for each nozzle, respectively. Since our experiments were conducted for nozzles ranging from single/multiple orifices to a porous airstone, it was not possible to estimate values of U_e and d_e (i.e., Fr) for each nozzle in order to collapse all the experimental data in one single curve. Therefore, we neglected Fr and obtained the following dimensionless correlations by adjusting straight lines to the radial distributions of d_b and u_b and a Gaussian curve to the radial distribution of a, the variation corresponding to the upper and lower limits obtained with different nozzles.

$$\frac{d_b}{L}=\left(0.75\pm 33\%\right)-0.35\left(\frac{r}{L}\right) \tag{4.5}$$

$$\frac{u_b}{U}=\left(2.70\pm 11\%\right)-0.13\left(\frac{r}{L}\right) \tag{4.6}$$

$$aL=\left(0.23\pm 41\%\right)e^{-0.12\left(\frac{r}{L}\right)} \tag{4.7}$$

Figure 4-10 shows the adjustment of Eqs. (4.5), (4.6) and (4.7) to experimental data. Not only good adjustments were obtained, but also the upper and lower limits represented by dashed lines clearly show the maximum variation of each parameter with nozzle type (e.g., dimensionless bubble diameter decreases when using the porous airstone instead of the single orifice nozzle of 3.0 mm). This confirms that Fr is of secondary importance for our sets of experiments.

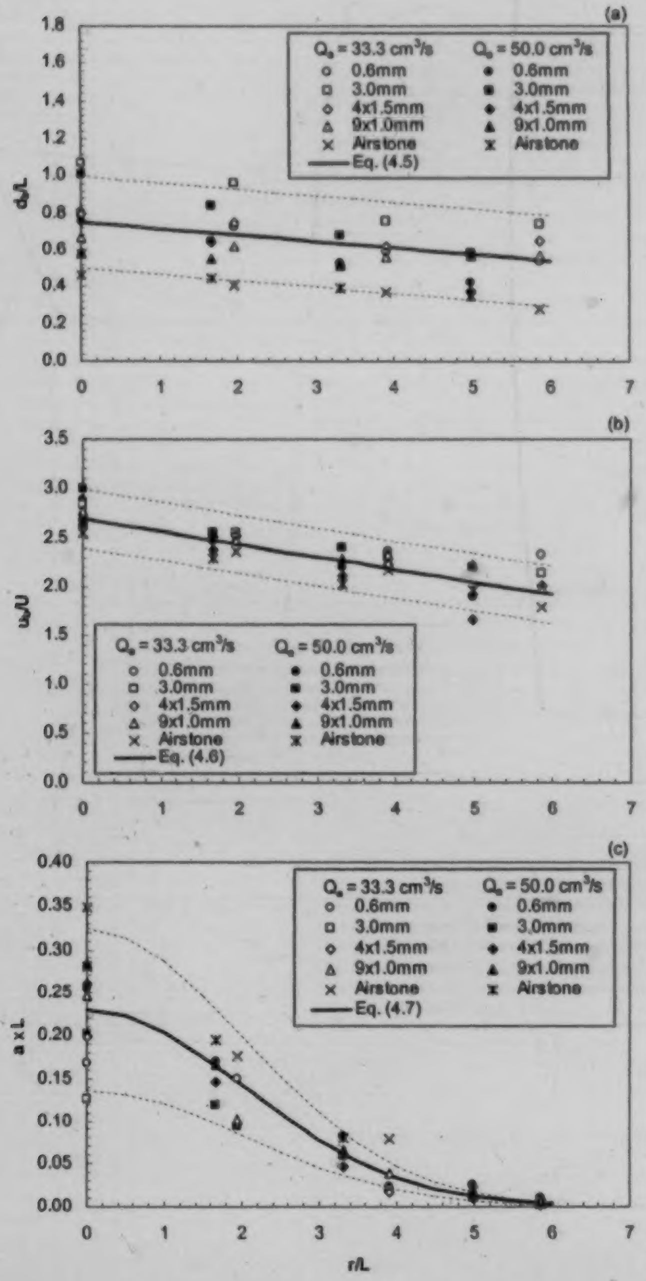

Figure 4-10. Adjustment of Eqs. (4.5), (4.6) and (4.7) to experimental data, with dashed lines indicating approximately the maximum variation of each parameter with nozzle type.

4.3.2. Surrounding Flow Structure

Similar to void fraction measurements, the liquid velocity time series obtained from PIV measurements also indicated a low-frequency periodic fluctuation about the mean. Figure 4-11 shows a typical power spectrum of the horizontal and vertical velocity components, u and v. A line with a slope of -5/3 is also shown to indicate the presence of Kolmogorov's inertial subrange. A dominant frequency of about 0.03 Hz was obtained for the velocity signals near the bubble core. Notice that this frequency was the same obtained from void fraction measurements, which implies that the periodic fluctuation of the velocity signals was caused mainly due to the wandering motion (i.e., bubble core oscillation). Because of this non-stationary nature of the flow surrounding the bubble plumes, a digital filtering technique was used to separate the turbulent motions (i.e. high-frequency signals) from the periodic motions (i.e. low-frequency signals). A fixed cut-off frequency of 0.2 Hz was used for all the experimental conditions. This frequency was selected to be higher than the dominant frequency in the spectrum, as described by García and García (2006) and Lima Neto et al. (2007b). Thus, a Butterworth high-pass filter of 6th order was used to eliminate the mean ($\bar{u}$ and $\bar{v}$) and this low frequency periodic (u'' and v'') velocity fluctuations from the original velocity signal and estimate the turbulent (high frequency) velocity fluctuations u' and v', where $u = \bar{u} + u' + u''$ and $v = \bar{v} + v' + v''$. An example of this velocity decomposition is shown in Fig. 4-12. Although the periodic velocity fluctuations were significant, our discussion will focus on the axial distributions of mean-turbulent velocity components near the bubble core, which are important for estimation of the entrainment rate and kinetic energy of the mean-turbulent flow.

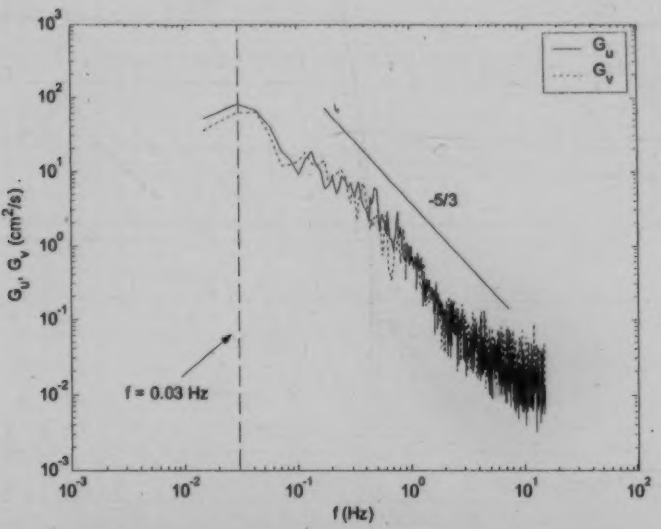

Figure 4-11. Power spectrums of horizontal and vertical velocity components (G_u and G_v) measured at r = 10.8 cm and z = 43 cm, indicating the dominant frequency (0.03 Hz) and the presence of an inertial subrange (line with slope of -5/3) (nozzle type: 9 x 1.0 mm, Q_a = 33.3 cm^3/s).

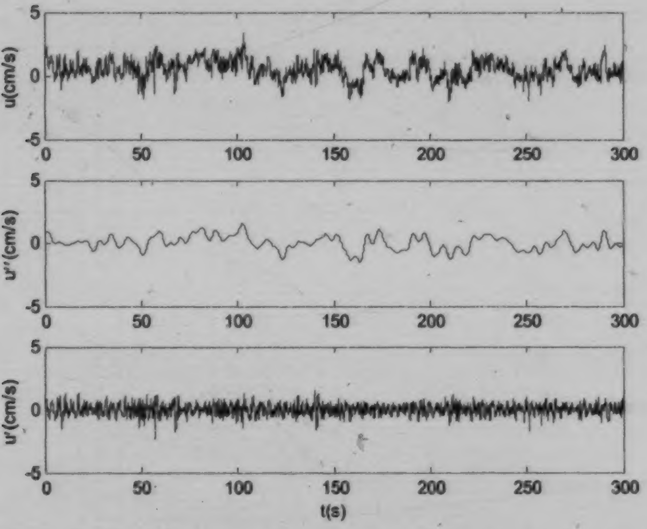

Figure 4-12. Velocity decomposition: (a) original velocity signal u measured at r = 10.8 cm and z = 43 cm; (b) periodic velocity component u''; (c) turbulent velocity component u' (nozzle type: 9 x 1.0 mm, Q_a = 33.3 cm^3/s).

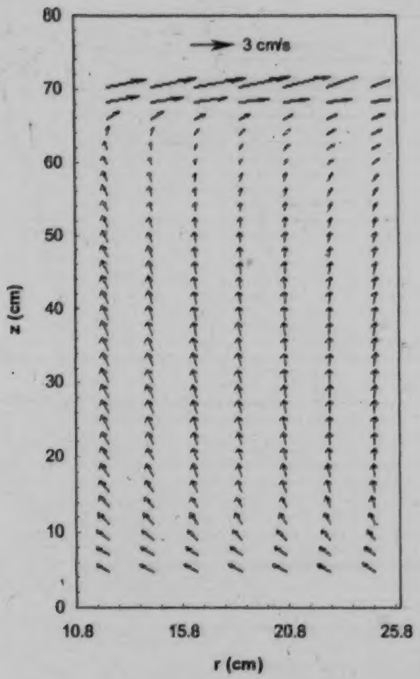

Figure 4-13. Time-averaged flow field indicating a velocity scale of 3 cm/s (nozzle type: 9 x 1.0 mm, $Q_a = 33.3$ cm^3/s).

A typical time-averaged flow field is shown in Fig. 4-13. It can be seen that the mean horizontal velocity component, $\overline{u}$, decreases with axial distance from the nozzle while the vertical velocity component, $\overline{v}$, increases until the flow approaches the surface jet region. The initial thickness of the surface jet (obtained at $r = 15$ cm from the centerline) was of about 12 cm for all experiments, which is consistent with the thickness of about 1/6 of water depth obtained by Fanneløp et al. (1991) and Riess and Fanneløp (1998) for the flow around line-source bubble plumes. Therefore, the cumulative volumetric entrainment rate, Q_w, was estimated by integrating the product of $\overline{u}$ (measured at $r = 10.8$ cm) by the surface area of a cylinder of radius $r_c = 10.8$ cm surrounding the bubble core from $z_1 = 4.5$ cm to $z_2 = 59$ cm, where $\overline{u}$ becomes approximately zero and the border of the surface jet region is reached

$$Q_w(z) = \int_{z_1}^{z} \overline{u}(z) 2\pi r_e \, dz \qquad (4.8)$$

The kinetic energy of the mean flow, *MKE*, and turbulent flow, *TKE*, were calculated (for measurements at $r = 10.8$ cm) using the following equations

$$MKE = \frac{1}{2}\left[\left(\overline{u}\right)^2 + \left(\overline{v}\right)^2\right] \qquad (4.9)$$

$$TKE = \frac{1}{2}\left[\overline{\left(u'\right)^2} + \overline{\left(v'\right)^2} + \overline{\left(w'\right)^2}\right] \qquad (4.10)$$

Because any swirl motion was avoided during the tests, we assumed that the third mean velocity component $\overline{w}$ was equal to zero in Eq. (4.9). We also assumed that the third turbulent velocity component w' was equal to v' in Eq. (4.10). This assumption is supported by measurements of turbulent stresses. Figure 4-14 shows typical axial distributions of the turbulent horizontal normal stresses, vertical normal stresses, and shear stresses. It can be seen that the horizontal normal stresses are slightly higher than the vertical normal stresses and that the shear stresses are very small, which implies that the turbulent flow field is nearly isotropic. Therefore, the assumption of $w' = v'$ is reasonable. The increase in magnitude of the stresses with air flow rate and height is in agreement with the measurements of turbulent kinetic energy, dissipation and eddy diffusivity obtained respectively by García and García (2006), Soga and Rehmann (2004) and Wain and Rehmann (2005) for the flow field surrounding a large-scale bubble plume. Iguchi et al. (1989, 1992) found that the magnitude of the turbulent fluctuations at the bubble core centerline increases with air flow rate but decreases with height in a confined bubble plume setup.

Typical axial distributions of the cumulative entrainment rate and kinetic energy of the mean and turbulent flow are shown in Fig. 4-15. It can be seen that the variation of Q_w with height is well described by a straight line. Notice that this straight line applies for the region above approximately 10 cm from the nozzle exit, where the bubbles are expected to reach their terminal slip velocity, the flow becomes fully established and the cumulative entrainment rate increases linearly with height (see Leitch and Baines, 1989). The variations of *MKE* and *TKE* with height are well described by a polynomial curve and an exponential curve, respectively, but the discrepancy between the measurements of *TKE* and the exponential curve increases as the flow approaches the surface jet region.

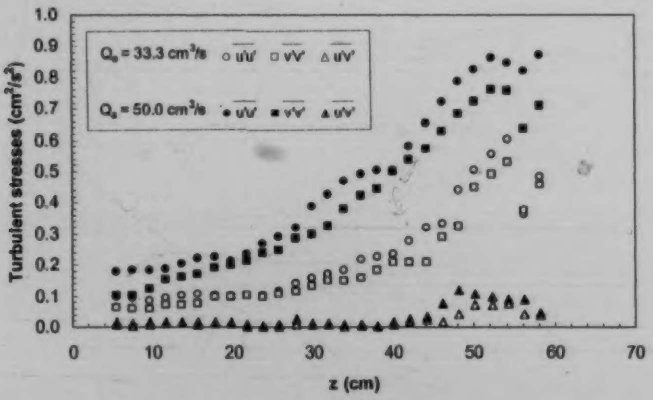

Figure 4-14. Typical axial variation of the turbulent stresses measured at $r = 10.8$ cm (nozzle type: 9 x 1.0 mm).

It is important to compare the water flow rate Q_w obtained from the PIV measurements (Fig. 4-15) with that from the velocity measurements [Fig. 4-8(b)]. The values of Q_w at 43 cm above the nozzles were obtained by integration of the mean vertical velocities [see Fig. 4-8(b)], assuming a linear decay of centerline velocity up to about $r = 9$ cm, where the vertical velocity becomes approximately zero. Overall the values of Q_w obtained with direct velocity measurement within the plume were approximately 10% larger than those measured with PIV. Note that we added 500 cm³/s to the values of Q_w measured with PIV to account for the fact that these measurements were taken from $z_1 = 4.5$ cm above the nozzle exit [see Fig. 4-15(a)]. Some discrepancy between these techniques was expected because the measurements with the anemometer were taken when the bubble plumes were in a straight vertical position while the measurements with PIV were averaged over 5 min, which also included the effects of wandering motion. The cumulative entrainment rates obtained here were about 30 % higher than those obtained by Iguchi et al. (1991) in a confined bubble plume setup for similar air flow rates and orifice diameters.

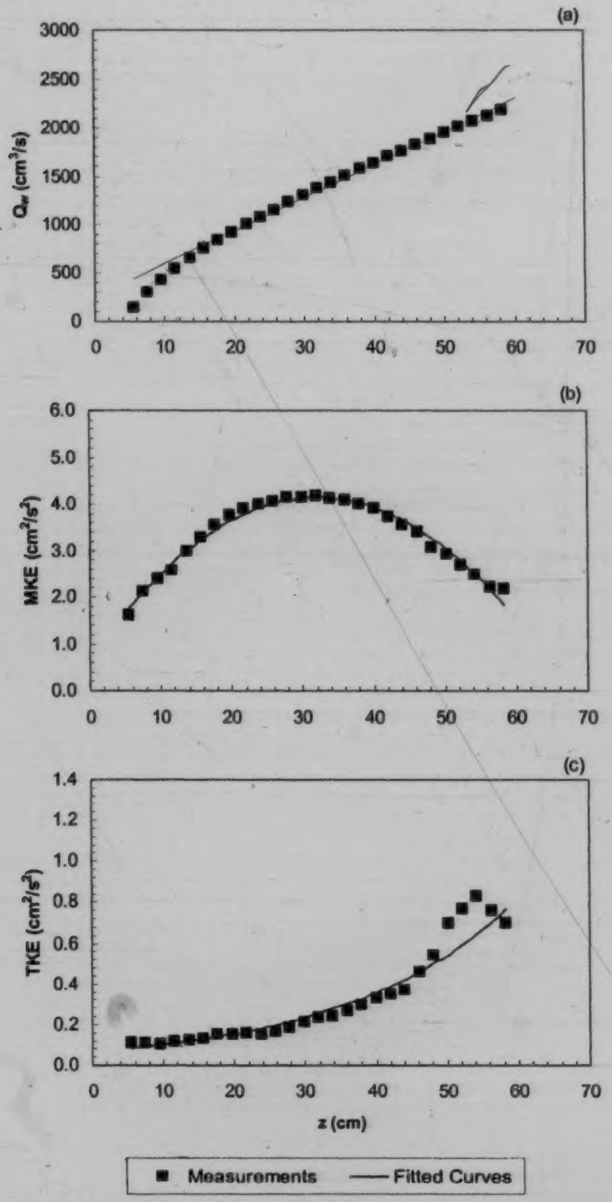

Figure 4-15. Typical axial variation of: (a) cumulative entrainment rate; (b) kinetic energy of the mean flow; (c) kinetic energy of the turbulent flow (nozzle type: 9 x 1.0 mm, Q_a = 33.3 cm^3/s). Measurements shown were taken at r = 10.8 cm.

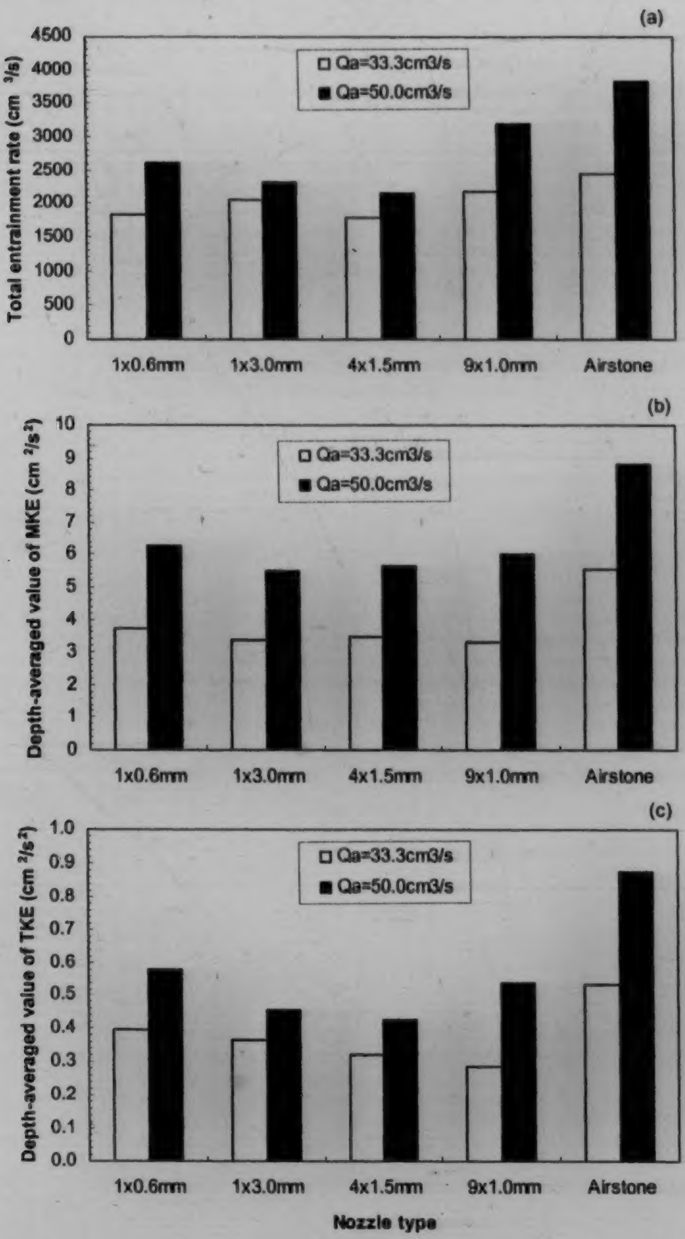

Figure 4-16. (a) Total entrainment rate; (b) depth-averaged value of kinetic energy of the mean flow; (c) depth-averaged value of kinetic energy of the turbulent flow. Measurements shown were taken at $r = 10.8$ cm.

The total entrainment rates and the depth-averaged values of kinetic energy of the mean-turbulent flow for each experimental condition are summarized in Fig. 4-16. It can be seen that the use of the airstone increases the entrainment rate by about 60% and the kinetic energy of the mean and turbulent flow by about 60% and 80%, respectively, when compared to the use of the multiple orifice nozzle of 4 x 1.5 mm. The results for the multiple orifice nozzle of 9 x 1.0 mm are comparable to those for the airstone, which confirms the suitability of its use for systems susceptible to rapid clogging of porous nozzles. Although the single orifice nozzle of 0.6 mm induced lower entrainment rates than the multiple orifice nozzle of 9 x 1.0 mm, it presented higher kinetic energy of the mean-turbulent flow than all the other non-porous nozzles because of the high momentum added to the flow due to the high-velocity jet. These results differ from those of Iguchi et al. (1989, 1992), who found that the mean velocity and the magnitude of the turbulent fluctuations at the bubble core centerline were independent of single orifice diameter in a confined bubble plume setup.

Similarly to the analysis for bubble characteristics, dimensional analysis gives the following relation to describe the axial variations of Q_w, *MKE* and *TKE* for a specific distance from the bubble core

$$\left[\frac{Q_w}{Q_a}, \frac{(MKE)^{0.5}}{U}, \frac{(TKE)^{0.5}}{U}\right] = f\left[\frac{z}{L}, Fr\right] \tag{4.11}$$

Again, we neglected *Fr* and obtained the following dimensionless correlations by adjusting a straight line, a polynomial curve and an exponential curve to the axial variations of Q_w, *MKE* and *TKE*, respectively, the variation corresponding approximately to the upper and lower limits obtained with different nozzles.

$$\frac{Q_w}{Q_a} = 3 + (1.15 \pm 26\%)\left(\frac{z}{L}\right) \tag{4.12}$$

$$\frac{(MKE)^{0.5}}{U} = -5x10^{-5}\left(\frac{z}{L}\right)^2 + 0.0031\left(\frac{z}{L}\right) + (0.03 \pm 45\%) \tag{4.13}$$

$$\frac{(TKE)^{0.5}}{U} = (0.014 \pm 40\%)e^{0.013\left(\frac{z}{L}\right)} \tag{4.14}$$

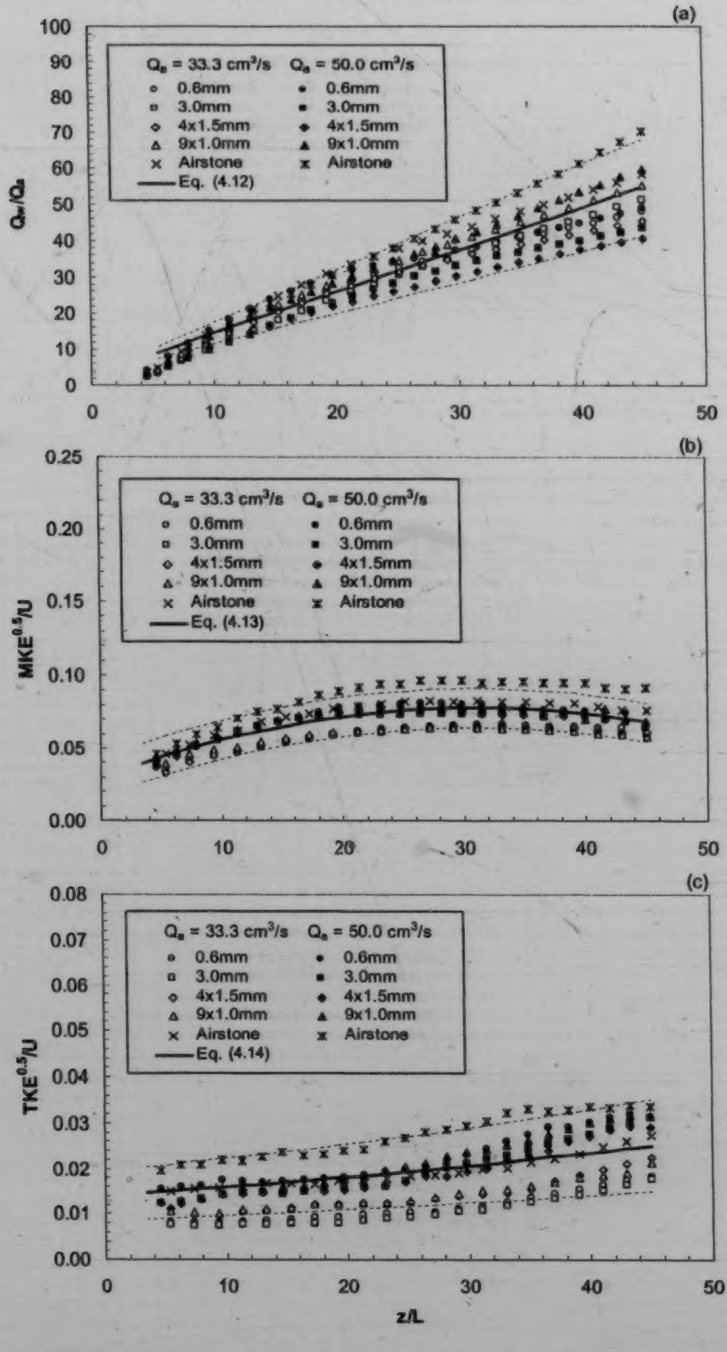

Figure 4-17. Adjustment of Eqs. (4.12), (4.13) and (4.14) to experimental data, with dashed lines indicating approximately to the maximum variation of each parameter with nozzle type.

Figure 4-17 shows a reasonably good correlation of Eqs. (4.12), (4.13) and (4.14) to experimental data. The upper and lower limits represented by dashed lines illustrate the maximum variation of each parameter with nozzle type (e.g., dimensionless entrainment rate increases when using the porous airstone instead of the multiple orifice nozzle of 4 x 1.5 mm). The results also confirm that the effects of *Fr* are relatively small for our experimental conditions.

4.4. Applications

The above results can be used to compare the aeration potential of air injection with different nozzles in shallow wastewater tanks and rivers. An example would be the use of mean bubble diameter and interfacial area to estimate the volumetric mass transfer coefficient (K_La) for each nozzle. Table 4-1 presents estimations of this coefficient considering the correlation given by Wüest et al. (1992) and McGinnis and Little (2002) for K_L as a function of the mean bubble diameter. The values of K_La ranged from 8.65 h^{-1} for the single orifice nozzle of 3.0 mm to 19.16 h^{-1} for the porous airstone, and are within the range from 0.12 h^{-1} for coarse bubble diffusers to 40.15 h^{-1} for very fine bubble diffusers obtained by Schierholz et al. (2006). This suggests that the nozzles evaluated in this study behaved similarly to their fine bubble diffusers. Note that even higher values of K_La are expected in rivers because of enhanced turbulence and bubble breakup processes due to the effect of crossflow. Since the K_La values due bursting of bubbles at the water surface obtained by Schierholz et al. for fine bubble diffusers decreased from about 45 to 5 % of those due to bubble plume aeration as the air flow rate decreased, we expect a contribution even smaller than 5 % in our testes because our flow rates were much smaller.

The correlations obtained here can be applied to predict bubble characteristics and surrounding flow structure in aeration/mixing systems for air flow rates and nozzles similar to those tested in this study. An example of this application would be a bubble plume in a wastewater tank of 4 m diameter and 1.8 m depth where a circulation flow of about 30,000 cm^3/s

is desired to prevent suspended solids deposition and formation of an anaerobic layer at the bottom. Thus, considering an initial surface jet thickness of about 30 cm (i.e., 1/6 of water depth, as mentioned above), the correlation given by Eq. (4.12) predicts an air flow rate Q_a of 415 cm^3/s to attain such requirement. In this case, we could use a circular nozzle of 90 orifices of 1.0 mm diameter with similar flow rate per orifice as the nozzle of 9 x 1.0 mm tested here. Notice that this assumption is not expected to be valid for much higher flow rates per orifice because continuous bubble jets are formed and the flow pattern changes significantly, as the supersonic flow studies conducted by Kobus (1968). Similar analysis can be applied for the porous airstone, but the flow rate per unit area of the stone should be considered instead of the flow rate per orifice.

It is also important to note that, in real wastewater treatment plants, the presence of suspended solids may affect the movement and morphology of the bubbles. Although little is known about the effect of suspended solids and other impurities on bubble swarms, studies on isolated bubbles show that it results in decreased bubble slip velocities due to increased drag forces. The curve given by Clift et al. (1978) shows that the difference between bubble slip velocity in pure and contaminated water systems vary about 30% for the range of bubble equivalent diameters of 3-12 mm obtained in our study. In this case, we expect that decreases in bubble slip velocity will decrease the turbulence levels and the induced liquid volume flux by generating wakes behind the bubbles with lower velocities (see Leitch and Baines, 1989). On the other hand, we expect a counterbalancing effect of increased turbulence due to particle-particle and particle-bubble interactions. Therefore, in wastewater treatment systems, we believe that our correlation for liquid volume flux would give reasonably accurate results with an error of less than about 30% due to the presence of suspended solids in the water.

This study also provides information such as bubble size distribution and entrainment rate for initial conditions in integral bubble plume models (see Wüest et al., 1992) and turbulent flow structure for evaluation and validation of CFD models for more detailed analysis of bubble plume systems (see Buscalia et al., 2002). Besides, information on surface jet thickness and flow rate can be applied to estimate surface aeration due to turbulent diffusion (see Chu and Jirka, 2003).

4.5. Summary and conclusions

An experimental study on air injection in a relatively large water tank was performed to investigate the effect of nozzle type, including single/multiple orifice nozzles and a porous airstone, on the characteristics of the bubbles and the surrounding liquid flow structure. The results revealed that radial distributions of bubble size and velocity were well described by a straight line, while the specific interfacial area followed a Gaussian curve. Bubble slip velocity was found to be higher than the terminal bubble velocity obtained from the literature for isolated bubbles. The water velocity within the bubble plume was found to decrease linearly from the center of the plume to zero at the edge of the plume. The variation of cumulative liquid entrainment rate with height was well described by a straight line, while the variations of kinetic energy of the mean and turbulent flow near the bubble core were well described by a polynomial curve and an exponential curve, respectively.

Although bubble velocity did not change significantly, bubble mean Sauter diameter could be decreased by about 50% while air-water specific interfacial area could be increased by about 90% by using the porous airstone instead of a single orifice nozzle of 3.0 mm diameter. The use of the airstone could also increase the liquid entrainment rate by about 60% and the kinetic energy of the mean and turbulent flow near the bubble core by about 60% and 80%, respectively. The results for a nozzle with 9 orifices of 1.0 mm diameter are comparable to those for the airstone, which suggests the suitability of nozzles with multiple orifices of small diameter for systems susceptible to clogging of porous nozzles such as wastewater treatment tanks and natural water bodies with high concentration of suspended solids and/or organic matter.

Dimensionless correlations using length and velocity scales based on the air flow rates described well the radial variations of the bubble properties and the axial variations of the entrainment rate and kinetic energy of the mean and turbulent flow near the bubble core, and are suggested here for design purposes of artificial aeration/mixing systems. Finally, applications of the results such as estimation of the volumetric mass transfer coefficient and entrainment rate for different artificial aeration/mixing systems are presented.

4.6. Notation

The following symbols are used in this chapter:

a = air-water specific interfacial area (m^{-1})

C = dissolved oxygen (DO) concentration in water (mg/L)

C_s = saturation DO concentration in water (mg/L)

d_b = bubble mean Sauter diameter (mm)

f_b = bubble frequency (Hz)

L = length scale defined by $L=\left(Q_a^2/g\right)^{1/5}$ (cm)

MKE = kinetic energy of the mean flow (cm^2/s^2)

Q_a = volumetric air flow rate (cm^3/s)

Q_w = volumetric entrainment rate (cm^3/s)

r = radial distance from the plume centerline (cm)

TKE = kinetic energy of the turbulent flow (cm^2/s^2)

U = velocity scale defined by $U=Q_a/L^2$ (cm/s)

u_b = bubble velocity (m/s)

$\overline{u}$, $\overline{v}$ = time-averaged horizontal and vertical velocity component (cm/s)

u', v' = turbulent horizontal and vertical velocity fluctuation (cm/s)

u'', v'' = periodic horizontal and vertical velocity fluctuation (cm/s)

$\overline{u'u'}$ = horizontal normal stress due to turbulent fluctuations (cm^2/s^2)

$\overline{v'v'}$ = vertical normal stress due to turbulent fluctuations (cm^2/s^2)

$\overline{u'v'}$ = shear stress due to turbulent fluctuations (cm^2/s^2)

z = axial distance from the nozzle exit (cm)

α = air concentration or void fraction (%)

Chapter 5

Bubbly Jets in Stagnant Water*

5.1. Introduction

Gas-liquid bubbly jets have attracted significant interest during the past three decades because of their high efficiency in promoting artificial aeration, mixing, and chemical reactions in liquids. These two-phase jets are produced by combining liquid pumping with gas pumping, and their gas volume fraction, defined as the ratio of the gas flow rate to the total gas-liquid mixture flow rate, usually ranges from about 5%-80%. Previous experimental investigations on the structure of gas-liquid bubbly jets have been conducted by Sun and Faeth (1986a, b), Kumar et al. (1989), and Iguchi et al. (1997). Sun and Faeth (1986a, b) studied air-water bubbly jets with gas volume fractions lower than 10%, where the liquid phase properties were not strongly affected by inter-phase transport. On the other hand, Kumar et al. (1989) and Iguchi et al. (1997) conducted experiments on air-water bubbly jets with gas volume fractions of up to 20% and 50%, respectively, and found that increases in the gas volume fraction slightly increased the mean liquid velocity but significantly increased its turbulent components. However, these experimental investigations were performed in small-scale vessels, with a diameter (or width) of up to 20 cm and a water depth of up to 40 cm, where the tank walls could impact on the behavior of the bubbly jets (as observed by Lima Neto et al., 2007b in bubble plumes). Besides, gas-phase properties in those bubbly jets such as bubble size distribution and bubble velocity have not been investigated in details.

Concerning the effect of bubbles in flows other than bubbly jets, Leitch and Baines (1989) performed experiments on very dilute bubble plumes in a water tank and concluded that the individual bubble wakes can contribute significantly to the entrainment into the liquid jet, in contrast with the results obtained by Kumar et al. (1989) and Iguchi et al. (1997). In this case, since the space between the bubbles was rather large compared to their size and wakes, bubble properties such as relative velocity between the bubbles and the water (i.e., bubble slip velocity) and drag coefficient were assumed to be the same as those for isolated bubbles. However, this is not expected to be true when the space between the bubbles is smaller, since the interactions of the bubbles and their wakes here have a much greater bearing. Ruzicka (2000) summarized several studies on bubbles rising in line and showed that bubble slip velocity increases and drag coefficient decreases as the space between the bubbles decreases. Risso and Ellingsen (2002) conducted experiments in a dilute bubble column with local void fractions of up to about 1% and showed that liquid velocity fluctuations are controlled by non-linear interactions between the wakes of the bubbles. Rensen et al. (2005) carried out experiments in a water tunnel with void fractions of up to about 3% and showed that the bubbles cause a more significant turbulent energy enhancement on small scales than on large scales. On the other hand, there is no consensus as to the behavior of such properties as slip velocity and drag coefficient at higher void fractions, or of liquid flow structure under varied experimental configurations (see summary in Mudde, 2005).

---

* A paper based on the content of this chapter is under review for submission to the Journal of Fluid Mechanics, as Lima Neto et al. (2007a).

In the present study, we conduct experiments in a relatively large tank in order to investigate the behavior of bubbly jets with gas volume fractions ranging from about 7%-83%. The objective is to clarify the effect of the gas volume fraction and Reynolds number on bubble properties and the mean liquid flow structure induced by bubbly jets, as well as to obtain information such as bubble slip velocity and drag coefficient in such denser bubbly flows.

5.2. Experimental apparatus and program

The experiments were performed in a square glass-walled tank with a width of 1.2 m and a height of 0.8 m, (shown schematically in Fig. 5-1). The tank was filled with tap water to a depth of 0.76 m. The gas supply was taken from an air line, while the water was pumped from a small reservoir, and both air and water temperatures were fixed at about 20°C. Volumetric flow rates of air, Q_{ao}, and water, Q_{wo}, were adjusted by rotameters; mixed into a Venturi injector (Model 484, Mazzei Injector Corporation) connected to a vertical pipe below the tank with a diameter of 2.54 cm; and then discharged through a single orifice nozzle of 0.6 cm in diameter, d_o. The nozzle was placed at the center of the tank with its exit 4.5 cm above the bottom. This arrangement ensured appropriate bubbly flow conditions and allowed us to reach gas volume fractions up to 83%.

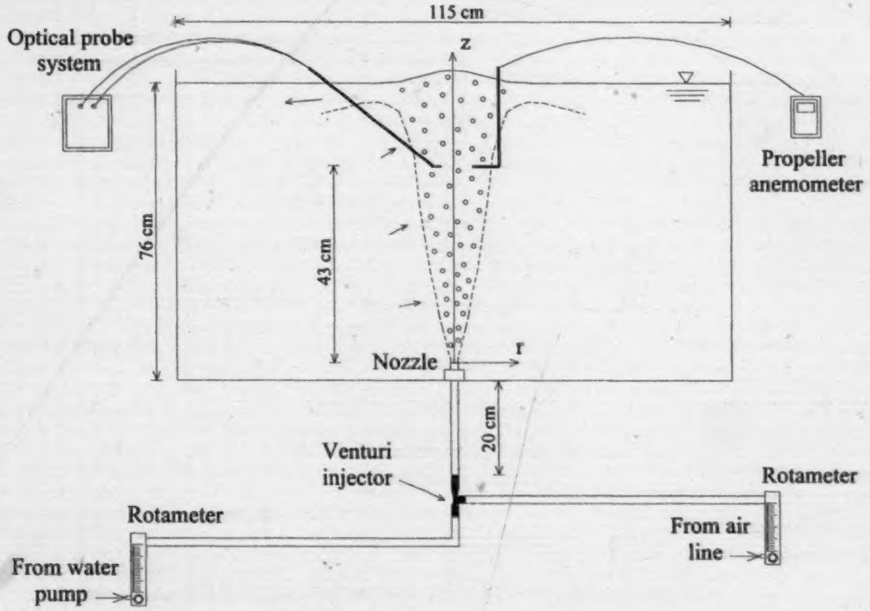
115 cm
Optical probe system
z
Propeller anemometer
76 cm
43 cm
Nozzle
r
20 cm
Venturi injector
Rotameter
Rotameter
From air line
From water pump

Figure 5-1. Schematic of experimental apparatus.

Table 5-1 summarizes the experimental conditions, where C_o and Re represent the gas volume fraction and Reynolds number, respectively, at the nozzle:

$$C_o = Q_{ao}/(Q_{ao} + Q_{wo}) \tag{5.1}$$

$$\mathrm{Re} = U_{wo} d_o / \nu_w \tag{5.2}$$

where U_{wo} is the superficial water velocity based on Q_{wo} and d_o, and ν_w is the kinematic viscosity of water.

Table 5-1. Summary of experimental conditions. The first and second numbers in the notation of the experiments correspond respectively to the air and water flow rates at the nozzle. C_o and Re are defined in the text [see Eqs. (5.1) and (5.2)].

Experiments	Q_{ao} (l/min)	Q_{wo} (l/min)	C_o (%)	Re
0.4-5	0.4	5.0	7.4	17684
1-5	1.0	5.0	16.7	17684
2-5	2.0	5.0	28.6	17684
3-5	3.0	5.0	37.5	17684
4-5	4.0	5.0	44.4	17684
5-5	5.0	5.0	50.0	17684
5-1	5.0	1.0	83.3	3537
5-2	5.0	2.0	71.4	7074
5-3	5.0	3.0	62.5	10610
5-4	5.0	4.0	55.6	14147
5-5	5.0	5.0	50.0	17684
1-1	1.0	1.0	50.0	3537
3-3	3.0	3.0	50.0	10610
5-5	5.0	5.0	50.0	17684
0-2	0.0	2.0	0.0	7074
0-3	0.0	3.0	0.0	10610
0-4	0.0	4.0	0.0	14147
0-5	0.0	5.0	0.0	17684

Typical images of the bubbles for each experimental condition are depicted in Fig. 5-2, where the images for the tests at constant water flow rate, air flow rate and gas volume fraction are shown in sequence. A 500 W halogen lamp was used for background illumination, and the images were acquired using a high resolution CCD camera (Pulnix TM-1040) controlled by a computer frame grabber system (Streams 5, IO Industries Inc.) with a frame rate of 30 fps and an exposure time of 1/4000 s.

A double-tip optical fiber probe system (RBI Instrumentation) based on the phase-detection technique was used to measure bubble properties. This system consists of a module that emits infrared light through two fiber-optic cables to the tips of the probe, 2 mm apart. Each tip extends 1.5 cm and is sharpened into a 30 μm diameter. Emitted light is reflected back to the module when the tips pierce a bubble, resulting in a two-state signal which is recorded at a sampling rate of up to 1 MHz. Similar RBI double-tip optical fiber probe systems have been used to measure two-phase flow characteristics in bubbly flows (Rensen and Roig, 2001; Murzyn et al., 2005).

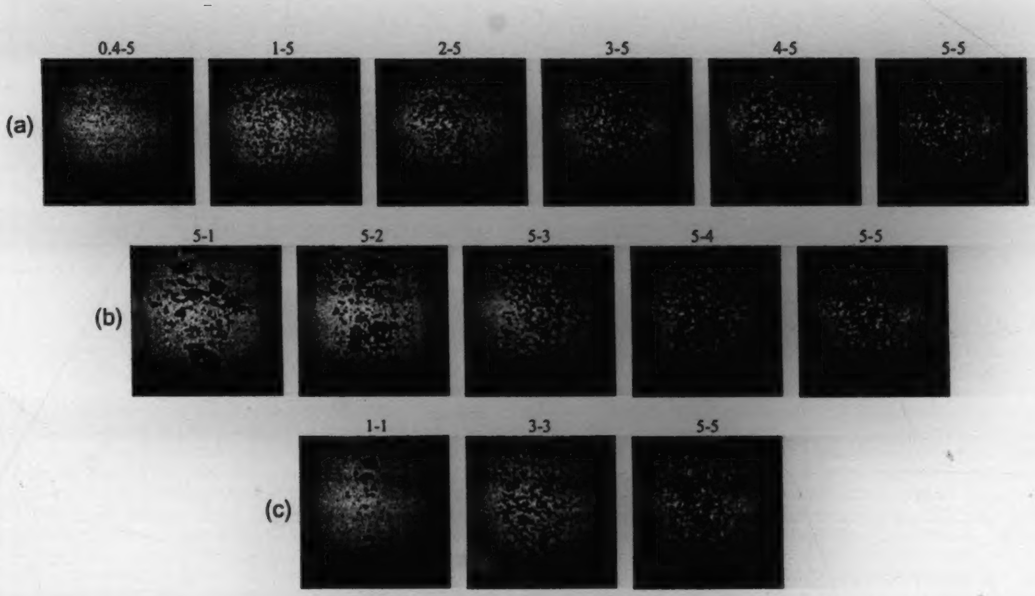

Figure 5-2. Bubble images for each experiment (images of 15 x 15 cm^2 with their centers at $r = 0$ and $z = 43$ cm): (a) at a fixed water flow rate, (b) at a fixed air flow rate, and (c) at a fixed gas volume fraction.

The signals obtained from the optical fiber probe system were processed to calculate the local void fraction (or volumetric air concentration), (C); bubble frequency, (f_b); and absolute bubble velocity, (u_b). The bubble volume-equivalent sphere diameter, (d_b), was then estimated (Herringe and Davis, 1976; Murzyn et al., 2005):

$$d_b = 3Cu_b/2f_b \tag{5.3}$$

Measuring the turbulent liquid flow field within the bubble core using particle image velocimetry was difficult since our flows had relatively high void fractions (i.e., up to about 4 times those of Risso and Ellingsen, 2002). Alternatively, visualization of the entrained liquid jet was achieved using laser-induced fluorescence (LIF). A similar LIF system has been used by Socolofsky (2001) for visualization of the entrained flow induced by bubble plumes. Measurements of the mean vertical water velocity inside the bubble core were performed with an electromagnetic propeller anemometer (Omni Instruments, MiniWater20) with an internal diameter of 22 mm. This anemometer is suitable for velocities higher than 2 cm/s, with an accuracy of 2% when used in pure water, and similar propeller anemometers have been used to measure the mean vertical water velocity in bubble plumes (Milgram, 1983; Fanneløp et al., 1991). The measurement error due to air bubbles in the water is deemed negligible for void fractions lower than 4%, as is the case in this study. The reliability of our propeller anemometer for measurements in vertical bubbly flows with void fractions of up to 3.5% was also confirmed by Lima Neto et al. (2006a).

Both optical probe and anemometer measurements were taken at radial distances, (*r*), of 0, 2, 4 and 6 cm from the bubbly jet centerline and at a height, (*z*), of 43 cm above the nozzle exit, which was more than sufficient for bubble breakup/coalescence processes to be completed. The experiments were carried out for a duration of 2 minutes, which was enough time to obtain stable measurements. The increase in water level due to water injection in the tank was less than 1% over the duration of each experiment, and this effect was considered negligible.

5.3. Results and discussions

5.3.1. Bubble properties and flow structure

Visual observations of the rising bubbles showed that their size did not change significantly with distance from the nozzle, as observed by Risso and Ellingsen (2002) for a disperse bubble column with a water depth of 0.70 m. Bubbles of relatively uniform sizes were generated in our tests, with the exception of experiments 1-1, 5-1 and 5-2 (see Fig. 5-2), where large and irregular bubbles were also generated.

The time series of bubble properties indicated a low-frequency periodic fluctuation about the mean value, which corresponded to the lateral oscillation of the bubble core, ranging from about 0.02 to 0.06 Hz. The occurrence of such oscillations, also called wandering motions, is usually attributed to buoyancy driven-instabilities and the effect of the tank walls (see Rensen and Roig, 2001; Lima Neto et al., 2007b). Figure 5-3 shows a typical void fraction time series measured with the two fiber-optic sensors of the RBI probe, in which *C* is about 1.6 % and the frequency of oscillation is about 0.05 Hz.

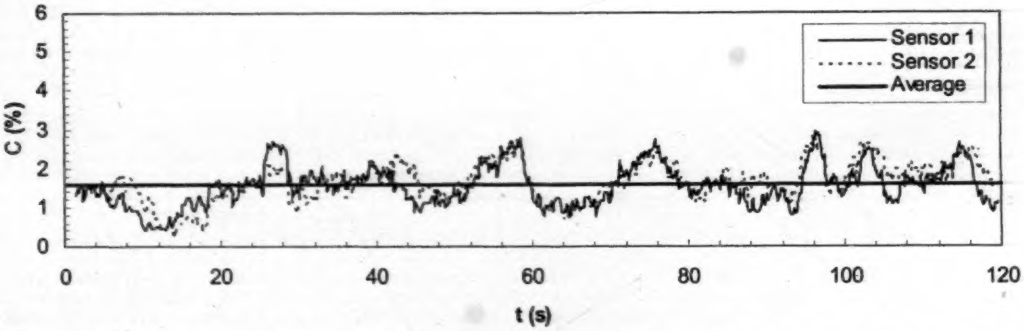

Figure 5-3. Typical void fraction time series (experiment 3-3). Measurements taken at $r = 0$ cm and $z = 43$ cm.

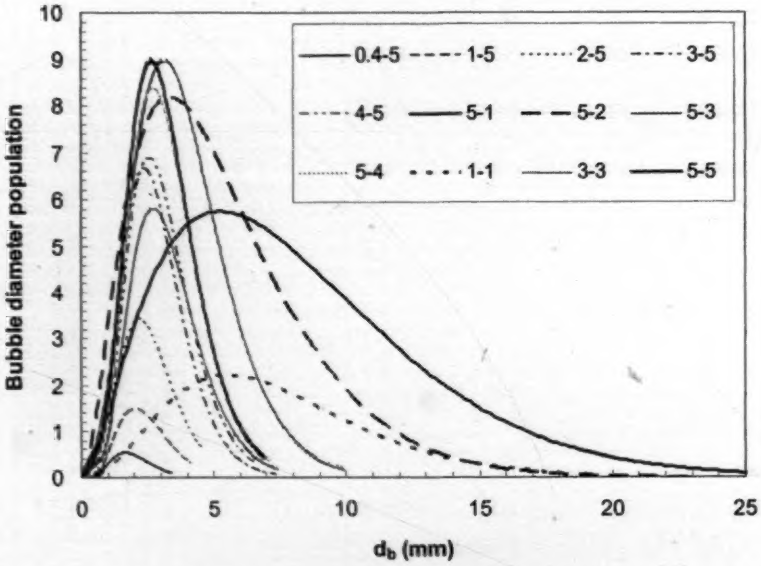

Figure 5-4. Typical bubble size distributions obtained from optical probe measurements at $r = 0$ cm and $z = 43$ cm.

Figure 5-4 shows typical bubble size distributions obtained from measurements at the jet centerline, resembling either gamma or lognormal curves. For three of the experiments (1-1, 5-1, 5-2), the average bubble diameter ranges from about 7-10 mm and is shifted to the right of the peaks. For all other experiments, the average bubble diameter ranges from about 2-4 mm and roughly coincides with the peaks. It can also be seen that the peaks increase along with the gas volume fraction with the result that more bubbles are generated (e.g., see curves for experiments 1-5 and 3-5), and are displaced to the left as the Reynolds number increases such that the bubble diameter slightly decreases (see curves for experiments 3-3 and 3-5, for example).

The non-uniform bubble sizes in experiments 1-1, 5-1 and 5-2 are attributed to the low momentum flux at the nozzle corresponding to a smaller water injection insufficient to break up large bubbles. These three experiments have Reynolds numbers less than 7100. The other experiments show much more uniform bubble sizes, and correspond to Reynolds numbers exceeding 10,600. We can thus conclude that a transition Reynolds number from non-uniform to uniform bubble sizes lies between these two values. We propose that a Reynolds number of 8000 is needed to produce sufficiently strong turbulence to generate uniform bubble sizes in bubbly jets.

Our proposed critical Reynolds number is consistent with the results of Sun and Faeth (1986a,b) and Iguchi et al. (1997), in which bubbles with approximately uniform sizes were observed photographically for experiments with Re-values exceeding about 8200 and 10700, respectively. It should be noted that both of these studies omitted experiments involving lower Reynolds numbers. Interestingly, bubbles with approximately uniform sizes were observed photographically by Kumar et al. (1989) at a smaller Reynolds number of Re = 4700. However, that study used a screen assembly to break up large bubbles and provide a more uniform mixture. Therefore, we expect that a minimum value of Re = 8000 is necessary to produce bubbles of uniform size, independent of the gas volume fraction. It should be mentioned that mean liquid velocity gradients can also cause bubble deformation and turbulence can provide the additional energy to cause bubble break up (see Risso and Fabre, 1998).

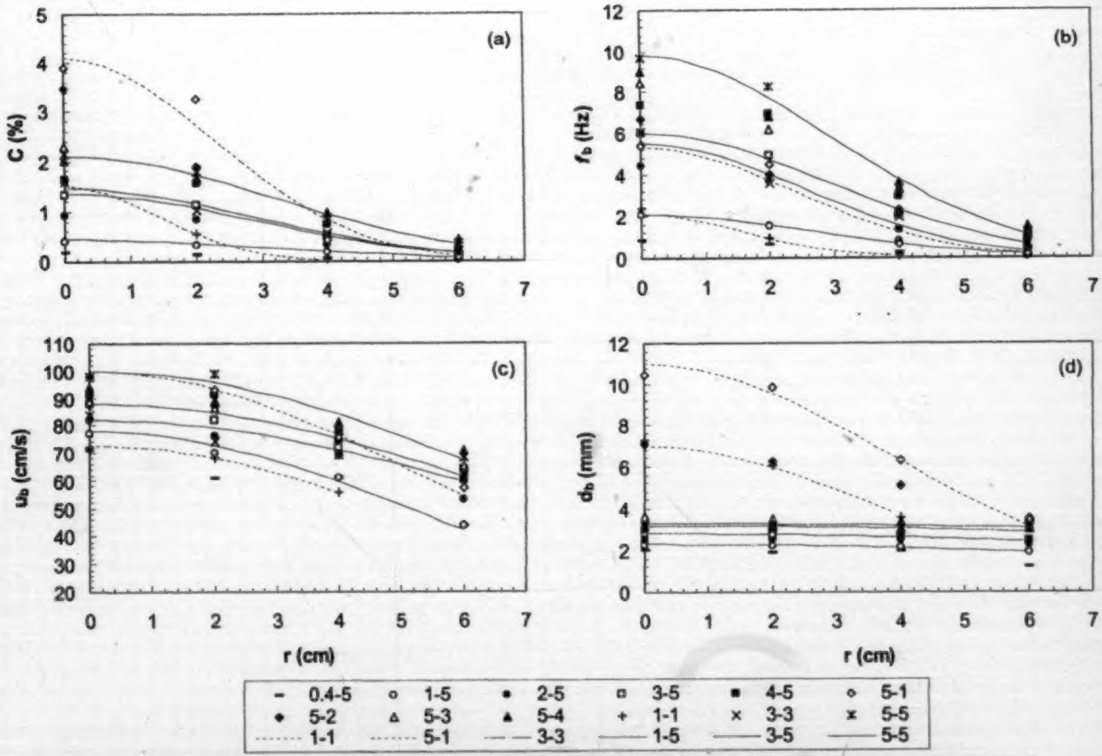

Figure 5-5. Time-averaged radial distributions of: (a) void fraction, (b) bubble frequency, (c) absolute bubble velocity, and (d) bubble diameter for each experimental condition. Measurements were taken at $z = 43$ cm. Line types indicate fitted Gaussian curves to the data with the same Reynolds numbers.

Figure 5-5 shows radial distributions of time-averaged void fraction, (C); bubble frequency, (f_b); absolute bubble velocity, (u_b); and bubble volume-equivalent sphere diameter, (d_b), for each experiment. Gaussian distributions were shown to conform well to all experimental data other than the bubble diameter, which decreased by about 10% from $r = 0$ to 6 cm for the experiments where Re > 8000. Line types indicate fitted curves to the data with the same Reynolds numbers. Although void fraction profiles for the experiments with Re < 8000 did not behave similarly to those for Re > 8000 [see Fig. 5-5(a)], the integration of C-values over the radial direction for the tests with the same air flow rates provided similar weighted-average void fractions, with a maximum discrepancy of about 15%. Bubble frequency and diameter profiles also behaved differently for these two ranges of Re-values, whereas bubble velocities did not vary significantly [see Figs. 5-5(b) – 5-5(d)]. For instance, bubble frequency and diameter for experiments 5-1 and 5-5 presented a two-fold difference even though bubble velocity was of the same order. Similar behaviors can also be observed for experiments 1-5 and 1-1, for example. Bubble diameters shown in Fig. 5-5(d) ranged from 1.2-10.5 mm and were about 10 % smaller than those obtained from the CCD camera images shown in Fig. 5-2, while bubble velocities shown in Fig. 5-5(c) ranged from 44-98 cm/s and were about 20% larger. Note that, for the experiments with very dense bubble clouds, this comparison was only possible closer to the border of the bubble core, where individual bubbles could be better visualized.

The effect of the gas volume fraction, (C_o), on bubble characteristics, (shown in Fig. 5-5), was relatively strong. For experiments 3-5 and 5-5, for example, we can see from the corresponding fitted Gaussian curves that an increase in C_o of 33% resulted in increases in C, f_b, u_b, and d_b of approximately 70%, 60%, 10%, and 20%, respectively. Conversely, the impact of the Reynolds number in these experiments was relatively weak. An increase in Re of 67% resulted in decreases in C and d_b by only 10% and increases in f_b and u_b by only about 20% and 10%, respectively.

The centerline values of the void fraction (C_c), bubble frequency (f_{bc}), absolute bubble velocity (u_{bc}), and bubble volume-equivalent sphere diameter (d_{bc}) are non-dimensionalized and correlate to C_o and Re in Fig. 5-6. The relationships between the above parameters and C_o are easily observed. The results for the experiments with varied Reynolds numbers also collapsed to the same linear curves, indicating that the effect of the Reynolds number can also be appropriately incorporated into the proposed relationships. The effect of Re (or U_{wo}) on the measured values of C_c, f_{bc}, and u_{bc} was relatively weak, as already mentioned. However, Re-value is directly proportional to U_{wo} and inversely proportional to C_o [see Eqs. (5.1) and (5.2)]. The bubble diameter, however, appears to be independent of the Reynolds number. In fact, only a slight decrease in d_b with respect to Re was observed. Note that these equations are obtained at a specific height of $z = 43$ cm above the nozzle exit.

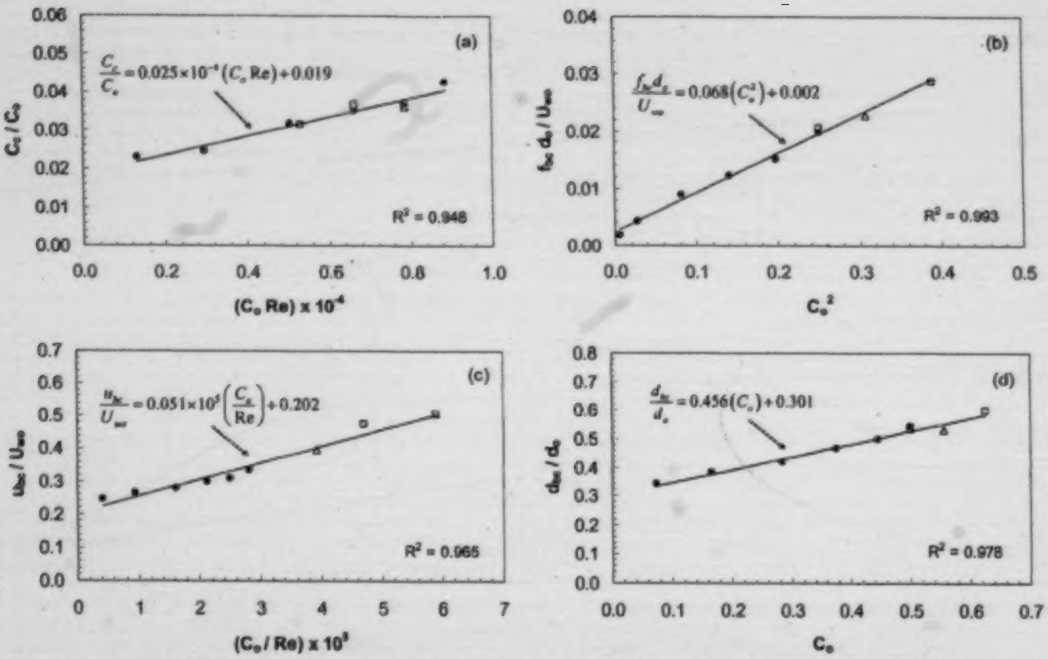

Figure 5-6. Centerline values of (a) void fraction, (b) bubble frequency, (c) absolute bubble velocity, and (d) bubble diameter. ● – Re = 17684, □ – Re = 14147, △– Re = 10610.

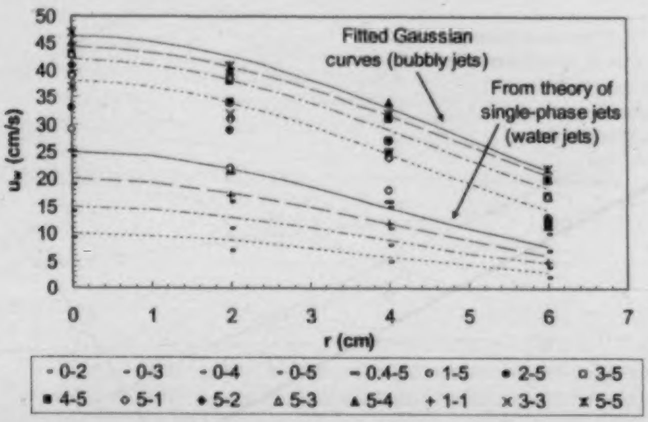

Figure 5-7. Radial distributions of axial water velocity. Measurements were taken at $z = 43$ cm. Lower and upper lines indicate fitted curves for pure water jets (0-2, 0-3, 0-4 and 0-5) and bubbly jets (5-2, 5-3, 5-4 and 5-5), respectively. Line types indicate data with the same Reynolds numbers.

Figure 5-7 shows radial distributions of the axial water velocity (u_w) measured with the Omni anemometer for the experiments with and without air injection into the water jets. The values obtained for the pure water jets followed Gaussian curves in accordance with the theory of single-phase jets (see Rajaratnam, 1976). The values obtained for bubbly jets also followed Gaussian curves, with the magnitude of the velocity increasing with the presence of the bubbles, as compared to pure water jets with the same Re-value. The observed axial water velocities for experiments 5-2, 5-3, 5-4 and 5-5 (with C_o ranging from 71.4%-50.0%), for example, were about 4-2 times larger than the corresponding values for experiments 0-2, 0-3, 0-4 and 0-5 (all with $C_o = 0$), respectively (see the upper and lower Gaussian curves shown in Fig. 5-7). This result differs from previous measurements in confined bubbly jets, where the effect of the gas volume fraction on the mean axial liquid velocity was relatively weak. Kumar et al. (1989) and Iguchi et al. (1997) investigated confined bubbly jets in small-scale vessels for C_o-values of up to 20% and 50 %, and detected increases in the axial water velocity due to the presence of the bubbles of only about 10 and 20 %, respectively. However, the increase in the intensity of turbulence due to the presence of the bubbles approached 100%. This probably occurred because of the relatively small size of their set-ups limiting the entrainment rate, and resulting in a weak increase of this entrainment rate with the gas volume fraction. In our case, the effect of the Reynolds number on measurements of axial water velocity was relatively weak. For experiments 5-3 and 5-5 (or 3-3 and 3-5), for example, an increase in Re-value of 67% resulted in an increase in u_w of only about 10% (observe the upper Gaussian curves in Fig. 5-7). The following dimensionless relationship was rendered by the curve-fitting of experimental data for Re > 8000 to describe the effect of C_o and Re on the axial water velocity:

$$\frac{u_{wc}}{U_{wo}} = 0.028 \times 10^5 \left(\frac{C_o}{\mathrm{Re}} \right) + 0.076 \qquad (R^2 = 0.993) \qquad (5.4)$$

where u_{wc} is the axial water velocity at the centerline. Figure 5-8(a) shows that Eq. (5.4) fitted well the experimental data. Reynolds number was incorporated into this equation because it is directly proportional to U_{wo}.

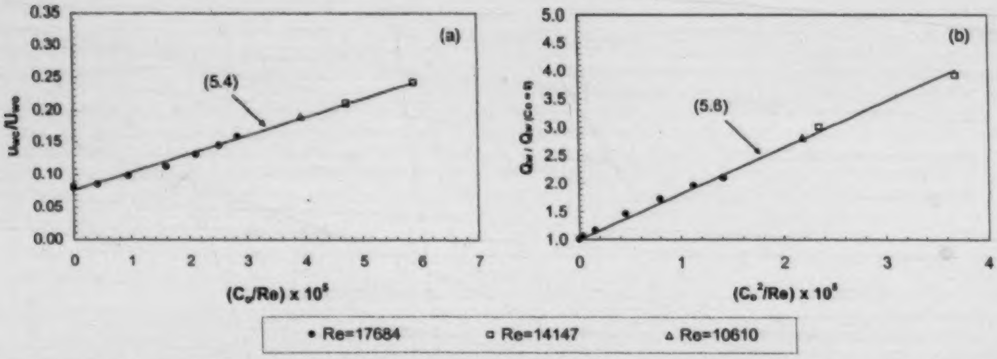

Figure 5-8. (a) Centerline values of axial water velocity and (b) liquid volume flux of the bubbly jet relative to that of a pure water jet with the same water flow rate at the nozzle. ● – Re = 17684, □ – Re = 14147, △– Re = 10610.

We define r_w and r_b as characteristic radii of the water jet and bubble core such that $u_w = e^{-1}u_{wc}$ and $C = e^{-1}C_c$, respectively. Fitting Gaussian curves to the water velocity profiles shown in Fig. 5-7 and neglecting the virtual origin of the jets, we find a linear spreading of the water jet radius, r_w/z, of about 0.12 for pure water jets, 0.11 for bubbly jets with Re < 8000, and 0.14 for bubbly jets with Re > 8000. This linear spreading was also observed from LIF images (see Fig. 5-9). The spreading rates obtained here are close to the value of 0.11 reported by Turner (1986) for single-phase jets and plumes, and are within the range of typical values of 0.10-0.20 reported by Milgram (1983) and Socolofsky (2001) for bubble plumes. A linear spreading ratio of the bubble core radius relative to the water jet radius, r_b/r_w, of about 0.50 for bubbly jets with Re < 8000 and 0.70 for bubbly jets with Re > 8000 is obtained by fitting Gaussian curves to the void fraction profiles shown in Fig. 5-5(a). Again, the spreading ratios obtained here are within the range of typical values of 0.50-0.90 reported by Milgram (1983) and Socolofsky (2001) for bubble plumes.

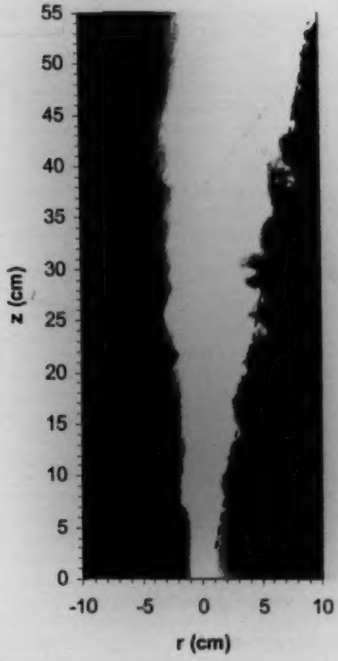

Figure 5-9. Typical LIF image of the bubbly jets (Exp. 3-3). Dashed line indicates a linear spreading of the water jet with height. Note that the left-hand side of the water jet is not completely visualized because the bubbles blocked the laser sheet, which was launched from the right-hand side.

With the assumption that we have a linear spreading of the water jet radius, Gaussian profiles of axial water velocity, and a constant entrainment coefficient, the liquid volume flux increases linearly with z (Rajaratnam, 1976):

$$\frac{dQ_w}{dz} = 2\pi r_w \alpha u_{wc} \tag{5.5}$$

where α is the entrainment coefficient. The entrainment coefficient can be obtained by solving Eq. (5.5) for the water flow rates at the nozzle exit, Q_{wo}, given in Table 1, and Q_w, (which is the liquid volume flux obtained by integration of u_w in the radial direction using fitted Gaussian curves). These calculations generated values of $\alpha = 0.050$ for pure water jets and 0.060 for bubbly jets, which are closer to the value of 0.054 reported by Turner (1986) for single-phase jets than the value of 0.083 for single-phase plumes, and are within the typical range of values, 0.03-0.15, reported by Milgram (1983) and Socolofsky (2001) for bubble plumes.

The liquid volume flux of a bubbly jet Q_w is compared to that of a pure water jet $Q_{w(C0=0)}$ with the same water flow rate at the nozzle in Fig. 5-8(b). Here, Q_w was obtained by direct integration of the axial water velocity profiles given in Fig. 5-7. Equation (5.6) was obtained by the curve fitting of experimental data for the tests with Re > 8000. Figure 5-8(b) shows that $Q_w/Q_{w(Co=0)}$ increases linearly with C_o^2/Re, reaching a maximum of about 4 for experiment 5-3. This result indicates that the liquid volume flux can be increased by about 300% when $C_o = 0.63$ and Re = 10610:

$$Q_w/Q_{w(Co=0)} = 1 + 0.818 \times 10^5 \left(C_o^2/\mathrm{Re}\right) \qquad (R^2 = 0.996) \qquad (5.6)$$

The increase in the liquid volume flux described by Eq. (5.6) can perhaps be attributed to additional entrainment into the wakes of the bubbles, which increase in number, velocity, and size as C_o increases (see Fig. 5-6). Based on the results of Uberoi and Freymuth (1970) for wakes behind a solid sphere, Leitch and Baines (1989) estimated that the entrainment associated with the bubble wakes generated by weak air injection in water ranged from 26-64% of the entrainment with the water jet surrounding the bubble core, with this ratio also increasing along with the gas flow rate. In the present study, it was not plausible to estimate the contribution of the wake of each bubble individually because the space between the bubbles was much smaller than the extent of the isolated wakes studied by Uberoi and Freymuth (1970). Accordingly, additional liquid turbulence caused by interactions of the bubbles and their wakes might also have contributed to the increase in liquid volume flux described by Eq. (5.6). This is consistent with the results of Hetsroni (1989), where particles with Reynolds numbers $\mathrm{Re}_p > 400$ tend to enhance turbulence in the flow, as in our case (see section 5.3.2), while particles with $\mathrm{Re}_p < 400$ tend to suppress it. The increase of $Q_w/Q_{w(Co=0)}$ with C_o^2/Re is also consistent with the results of Kumar et al. (1989), where the increase in turbulence intensities was more pronounced at higher gas volume fractions and lower Reynolds numbers. In the study conducted by Iguchi et al. (1997), the turbulence intensity also increased in conjunction with the gas volume fraction, but their study only presented measurements of turbulence at one Reynolds number, so we cannot compare with their results. A more recent study conducted by Risso and Ellingsen (2002) in a dilute bubble column also showed that, at a considerable distance from the bubbles, the liquid velocity fluctuations linked to non-linear interactions with bubble wakes scaled with the void fraction as $C^{0.4}$. However, their study was limited to gas injection with local void fractions up to about 1% and cannot be directly compared to our results.

5.3.2. Bubble slip velocity, shape and drag coefficient

Figure 5-10(a) shows bubble slip velocities, u_s, obtained by subtracting the water velocities from the absolute bubble velocities. Data obtained from Lima Neto et al. (2006a) by means of experiments on bubble plumes generated through different nozzles is also presented in this figure. It can be seen that, for both bubbly jets and bubble plumes, bubble slip velocity can be described as a function of bubble volume-equivalent sphere diameter, d_b. The values of u_s obtained here follow similar trends but are higher than the terminal bubble velocities given by Clift et al. (1978) for isolated bubbles with diameters ranging from 2-12 mm. This occurrence can be attributed to the fact that trailing bubbles in the wake of leading bubbles rise faster than isolated bubbles due to drag reduction, as observed by Ruzicka (2000) with experiments on bubbles rising in line.

Using the bubble diameters and slip velocities estimated above, we can calculate the bubble Reynolds number ($\mathrm{Re}_b = u_s d_b / \nu_w$), Eötvös number ($E_b = g \Delta \rho d_b^2 / \sigma$), and Morton number ($M_b = g \Delta \rho \mu_w^4 / \rho_w^2 \sigma^3$), where $\Delta \rho$ is the difference between the water density, ρ_w, and the air density, ρ_a, σ is the air-water surface tension; and μ_w is the viscosity of water. These dimensionless numbers are generally used to express the importance of inertia, buoyancy, surface tension, and viscosity on single bubbles rising in liquids. For the present experiments, the ranges of Re_b and E_b were 406-8627 and 0.2-19.5, respectively, and $M_b = 3.1 \times 10^{-11}$. According to the classical diagram describing the behavior of isolated bubbles provided by Clift et al., (1978), our values of Re_b, E_b and M_b fall within the region of spherical, ellipsoidal and wobbling regimes, which is in agreement with the shapes observed from the CCD images (see Fig. 5-2).

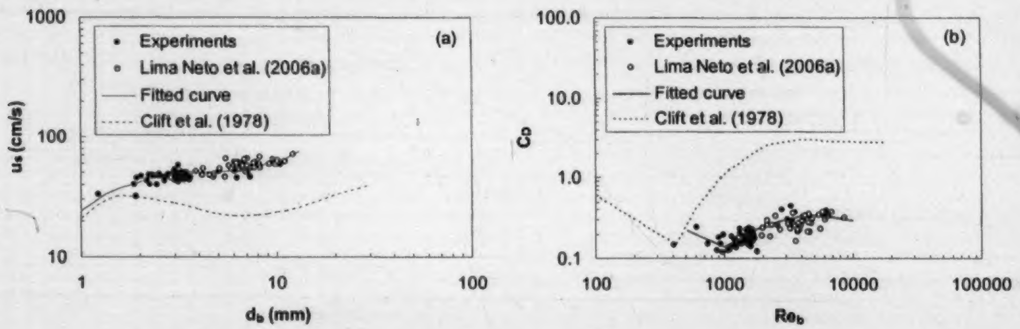

Figure 5-10. (a) Variation of bubble slip velocity with bubble diameter and (b) variation of drag coefficient [calculated using Eq. (5.7)] with bubble Reynolds number.

As mentioned above, changes in the size of the rising bubbles were negligibly small under the present experimental conditions. Thus, assuming that the bubble slip velocity is only a function of bubble diameter and does not vary with axial distance from the nozzle, the drag coefficient can be estimated by equating the drag force imposed by the bubbles to their buoyancy, as shown in the following equation:

$$C_D = \frac{4 d_b g \Delta\rho}{3 \rho_w u_s^2} \tag{5.7}$$

Experimental results obtained by Felton and Loth (2001) for spherical bubbles with diameters of 0.4-1.2 mm moving in a turbulent boundary layer with free stream velocities between 0.40 and 0.90 m/s support the approximation given by Eq. (5.7). In their study, drag and buoyancy forces were of the same magnitude while the other terms involved in the force balance (i.e. liquid stress gradient resulting from fluid acceleration and lift force arising from nonzero vorticity in the liquid flow), accounted for only 10% and 25% of those, respectively. In our case, we anticipate an even higher contribution of the buoyancy forces since the bubble diameters are larger, ranging from 1.2-10.5 mm, and a smaller contribution of the liquid stress gradient and lift force since our centerline water velocities are smaller, ranging from 0.25-0.47 m/s. An experimental study conducted by Ford and Loth (1998) on ellipsoidal bubbles moving in a turbulent shear layer with liquid velocities between 0.20 and 0.43 m/s also exhibited lift forces close to zero for bubbles with diameters ranging from 1.5-3.5 mm, and even negative values for bubbles with a 4.5 mm diameter. With these caveats, we expect our approximation of drag being balanced by buoyancy to be reasonable.

The variation of C_D [calculated using Eq. (5.7)] with Re_b is shown in Fig. 5-10(b). It is observed that the drag coefficient can be described as a function of the bubble Reynolds number. The values of C_D obtained here follow similar trends but are much smaller than those given by Clift et al. (1978) for isolated bubbles with Re_b ranging from about 700-9000. As mentioned, this must have occurred as a result of the fact that trailing bubbles in the wake of leading bubbles experience drag reduction (see Ruzicka, 2000). Moreover, in the curve obtained by Clift et al. (1978), we find a minimum at about $\mathrm{Re}_b = 400$ corresponding to the onset of bubble oscillations, where the small bubbles enter the ellipsoidal regime and the drag coefficient can be seen to increase significantly with Re_b until it reaches the spherical-cap regime and becomes approximately constant. Our results, however, show a clear delay in this minimum, which occurs at about $\mathrm{Re}_b = 1000$. Additionally, the increase in C_D beyond this point is much more gradual than that for isolated bubbles.

5.4. Conclusions

An experimental study on air-water bubbly jets in a relatively large water tank was carried out to investigate bubble properties and mean liquid flow structure. The test included bubbly jets with gas volume fractions, C_o, ranging from about 7%-83%, which produced bubbles with diameters ranging from about 1-10 mm. It was found that a Reynolds number at the nozzle exit exceeding about Re = 8000 was required to breakup larger bubbles into smaller bubbles and produce a more uniform bubble size distribution. For such conditions, bubble properties and mean liquid flow structure can be described by dimensionless relationships as functions of C_o and Re. Injection of air into a liquid jet can significantly increase the liquid volume flux, and the rate of the increase was found to be a linear function of C_o^2/Re. This increase was attributed to additional entrainment into the wakes of the bubbles and turbulence caused by interactions of the bubbles and their wakes, as reported in the literature for disperse vertical bubbly flows.

Bubble slip velocities were higher than the terminal velocities for isolated bubbles, while drag coefficients were smaller. It was concluded that this trend must be tied to the fact that trailing bubbles in the wake of leading bubbles have a lower drag, allowing them to rise faster than isolated bubbles. New relationships are proposed to describe bubble slip velocity as a function of bubble diameter and drag coefficient as a function of bubble Reynolds number. These interactions are important because two-phase models for vertical bubbly flows typically assume bubble slip velocity and drag coefficient values of the same order as those for isolated bubbles.

5.6. Notation

The following symbols are used in this chapter:

C = air concentration or void fraction (%)

C_o = gas volume fraction defined by Eq. (5.1)

d_b = bubble volume-equivalent sphere diameter (mm)

d_o = nozzle exit diameter (mm)

f_b = bubble frequency (Hz)

Q_{ao} = air flow rate at the nozzle (l/min)

Q_{wo} = water flow rate at the nozzle (l/min)

Re = Reynolds number defined by Eq. (5.2)

U_{wo} = superficial water velocity at the nozzle exit (cm/s)

u = vertical water velocity (m/s)

u_b = absolute bubble velocity (m/s)

u_s = bubble slip velocity (m/s)

x = horizontal distance from the nozzle exit defined in Fig. 5-1 (cm)

z = vertical distance from the nozzle exit defined in Fig. 5-1 (cm)

Chapter 6

Horizontal Injection of Gas-Liquid Mixtures in a Water Tank*

6.1 Introduction

Combination of gas and liquid injection have long been used for artificial aeration and mixing in tanks, lakes and rivers (Amberg et al., 1969; Fast and Lorenzen, 1976; Sun and Faeth, 1986a,b; Iguchi et al., 1997; Lima Neto et al., 2006b, 2007a). In these types of flows, the oxygen transfer rate from the bubbles to the water is usually estimated using the following equation, derived from Fick's law of diffusion (see Mueller et al., 2002):

$$\frac{dC}{dt} = K_L a\left(C_s - C\right) \tag{6.1}$$

where C and C_s are the dissolved oxygen (DO) concentration in the water and the saturation concentration, respectively, K_L is the liquid film coefficient or mass transfer coefficient, and a is the air-water interfacial area per unit liquid volume or specific interfacial area.

In water and wastewater systems such as aeration tanks, ponds, lagoons and oxidation ditches, where the water depth is usually small compared to the water surface area, the use of horizontal gas-liquid injection is preferable to vertical gas-liquid injection in order to increase the contact time between the gas and liquid phases. In these systems, mixing chambers, Venturi tubes or ejectors are generally used to mix the gas and the water and discharge the mixture as a series of two-phase jet-plumes that provide both aeration and mixing. These flows are a topic of growing interest because of their relatively high oxygen transfer efficiency and low maintenance and operational costs (Rainer et al., 1995; Morchain et al., 2000; Fonade et al., 2001, Mueller et al., 2002).

---

* A paper based on the content of this chapter has been submitted for publication in the Journal of Hydraulic Engineering, as Lima Neto et al. (2007c).

To the authors' knowledge, the only experimental study on the characteristics of the bubbles generated due to horizontal gas-liquid injection in tanks has been conducted by Varley (1995). In this study, bubble sizes were investigated photographically and a correlation based on dimensional analysis for estimation of the maximum bubble size was proposed. However, his study was limited to gas-volume fractions smaller than about 23%, which is defined as:

$$\varepsilon = Q_{ao} / (Q_{ao} + Q_{wo}) \tag{6.2}$$

where Q_{ao} and Q_{wo} are respectively the volumetric flow rates of air and water at the nozzle. In addition, Varley's measurements were taken only at the nozzle exit and at 10-15 nozzle diameters downstream of the nozzle exit, where bubble breakup and coalescence processes were assumed to be complete. Thus, only bubble size measurements were provided with no other detailed information on bubble characteristics such as bubble velocity and specific interfacial area. On the other hand, Morchain et al. (2000) and Fonade et al. (2001) have estimated the flow circulation patters induced by horizontal gas-liquid injection in water assuming that the liquid jets behave similarly to single-phase horizontal jets, independently of the presence of the bubbles.

In this paper, we conduct an experimental study on horizontal air-water injection with gas-volume fractions ranging from 13 to 63% in a water tank to investigate bubble properties and mean liquid flow structure. The results obtained here are important for estimating the performance of jet aeration systems and to validate CFD codes for simulation of such flows.

6.2. Experimental setup and procedure

The tests were conducted in a rectangular glass-walled tank with length of 1.8 m, width of 1.2 m, and height of 0.80 m, shown schematically in Fig. 6-1. The tank was filled with tap water to a depth of 0.76 m. The gas supply was taken from an air line, while the water was pumped from a small reservoir, and both air and water temperatures were fixed at about 20°C. Volumetric flow rates of air, Q_{ao}, and water, Q_{wo}, were adjusted by rotameters; mixed into a Venturi injector (Model 484, Mazzei Injector Corporation); and then discharged horizontally at the shorter plane of the tank through a single orifice nozzle of 0.6 cm in diameter, d_o. The nozzle was placed at the tank centerline with its exit located at 32 cm below the water surface.

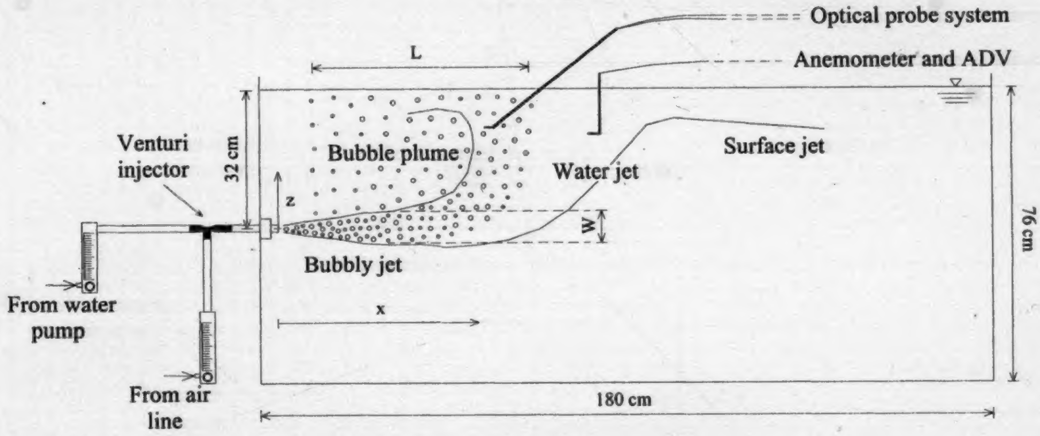
Optical probe system
Anemometer and ADV
L
Venturi injector
32 cm
Bubble plume
Water jet
Surface jet
z
W
76 cm
Bubbly jet
From water pump
x
From air line
180 cm

Figure 6-1. Schematic of experimental setup.

Table 6-1 summarizes the experimental conditions, where the gas-volume fraction (ε), Reynolds number (Re) and densimetric Froude number (Fr) at the nozzle are defined by Eqs. (6.2), (6.5) and (6.7), respectively:

Table 6-1. Summary of experimental conditions.

Experiments	Q_{ao} (l/min)	Q_{wo} (l/min)	ε	Re	Fr
1-3	1	3	0.25	10610	14.6
1-5	1	5	0.17	17684	29.8
1-7	1	7	0.13	24757	48.1
3-3	3	3	0.50	10610	10.3
3-5	3	5	0.38	17684	19.8
3-7	3	7	0.30	24757	31.1
5-3	5	3	0.63	10610	9.2
5-5	5	5	0.50	17684	17.2
5-7	5	7	0.42	24757	26.4

Typical images of the bubbles for each experimental condition are shown in Fig. 6-2. A 500 W halogen lamp was used for background illumination, and the images were acquired using a high resolution CCD camera (Pulnix TM-1040) controlled by a computer frame grabber system (Streams 5, IO Industries Inc.) with a frame rate of 30 fps and an exposure time of 1/2000 s.

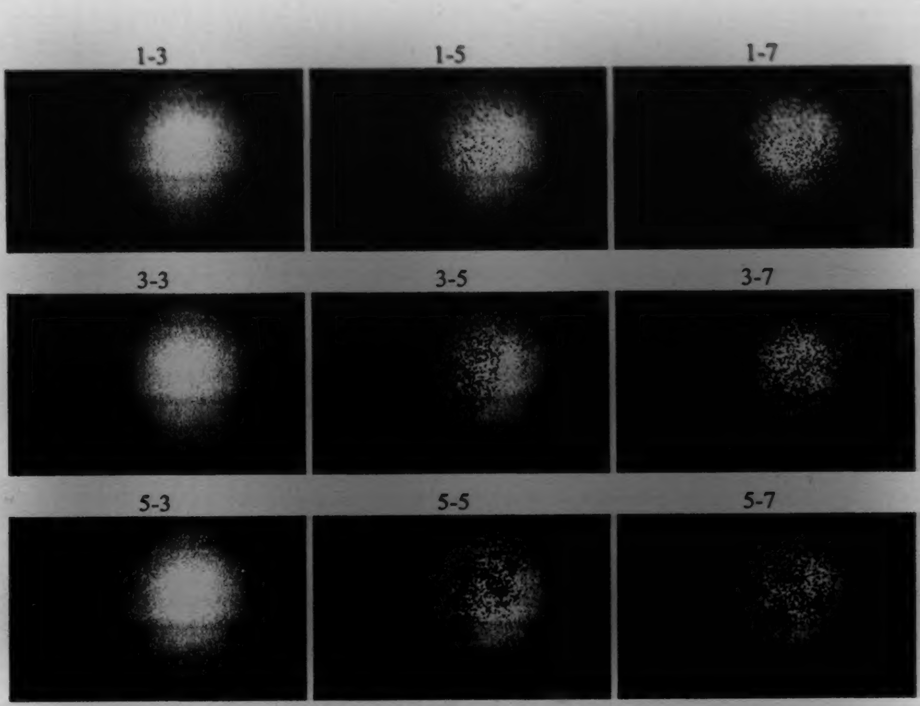

Figure 6-2. Typical images (32 x 50 cm^2) of the bubbles for each experimental condition, showing the tip of the optical probe located at $x = 16$ cm and $z = 24$ cm.

Visualization of the entrained liquid jet was achieved using laser-induced fluorescence (LIF). A similar LIF system has been used by Socolofsky and Adams (2002) for visualization of the entrained flow induced by bubble plumes. Measurements of the mean vertical water velocity along the bubble core centerline and the water jet centerline outside the bubble core were performed with an electromagnetic propeller anemometer (Omni Instruments, MiniWater20) with an internal diameter of 22 mm (see Fig. 6-1). This anemometer is suitable for velocities higher than 2 cm/s, with an accuracy of 2% when used in pure water, and similar propeller anemometers have been used to measure the mean vertical water velocity in bubble plumes (Milgram, 1983; Riess and Fanneløp, 1998). The measurement error due to air bubbles in the water is deemed negligible for void fractions lower than 2.5%, as is the case in this study. The reliability of the propeller anemometer for measurements in vertical bubbly flows with void fractions of up to 3.5% was also confirmed by Lima Neto et al. (2006a). The measurements outside the bubble core were also verified with an acoustic Doppler velocimeter (ADV) (SonTek, 1997). This ADV can measure velocities from about 1.0 mm/s to 2.5 m/s at a sampling rate of 25 Hz.

A double-tip optical fiber probe system (RBI Instrumentation) based on the phase-detection technique was used to measure bubble properties. It consists of a module that emits infrared light through two fiber-optic cables to the tips of the probe, 2 mm apart. Each tip extends 1.5 cm and is sharpened to 30 μm diameter. Emitted light is reflected back to the module when the tips pierce a bubble, resulting in a two-state signal which is recorded at a sampling rate of up to 1 MHz. Absolute bubble velocity is obtained through a cross-correlation analysis of the signals from the two tips of the probe. The same system has been used to measure bubble properties in vertical bubble plumes and bubbly jets (see Lima Neto et al., 2006a, 2007a). Similar RBI double-tip optical fiber probe systems have also been used for other bubbly flows (Boes and Hager, 2003; Murzyn et al., 2005).

The optical probe signals were processed to calculate void fraction (α), bubble frequency (f_b) and absolute bubble velocity (u_b). The following equations (see Chanson, 2002) were used to estimate the specific interfacial area (a) and bubble volume-equivalent sphere diameter (d_b):

$$a = 4 f_b / u_b \tag{6.3}$$

$$d_b = 6\alpha / a \tag{6.4}$$

The optical probe measurements were taken along the bubble core centerline at a height above the nozzle exit z of 24 cm, far enough for bubble breakup/coalescence processes to be complete and the bubbles to rise approximately in a rectilinear path. The tests were performed for a duration of 2 minutes to obtain stable measurements. The increase in water level due to water injection in the tank was less than 1% over the duration of each test. This effect was considered negligible.

6.3. Experimental results and analysis

6.3.1. Bubble properties

Typical images of the bubbles generated due to horizontal air-water injection in the tank are shown in Fig. 6-2. Bubbles with diameters ranging from about 1-4 mm were observed visually. This is consistent with previous experimental results on vertical air-water bubbly jets (see Lima Neto et al., 2007a), where bubbles in this size range were generated when the Reynolds number at the nozzle exit [given by Eq. (6.5)] exceed a limit of about Re = 8000.

$$\mathrm{Re} = U_{wo} d_o / \nu_w \tag{6.5}$$

where ν_w is the kinematic viscosity of water and U_{wo} is the superficial water velocity given by

$$U_{wo} = Q_{wo} / \left(\pi d_o^2 / 4 \right) \tag{6.6}$$

Bubble diameters ranging from about 0.3-2 mm were observed photographically by Varley (1995) from experiments on disperse horizontal bubbly jets with Re > 15000, but the measurements were taken only at the nozzle exit and at 10-15 nozzle diameters downstream of the nozzle exit. Our preliminary tests with Re < 8000 confirmed that for this condition the bubbles were much larger and irregular, and the bubble core was much shorter. Therefore, the results presented here are limited to experiments with Re > 8000, which are expected to be more efficient for aeration purposes. All the following analyses in this paper will be based on the densimetric Froude number [given by Eq. (6.7)], as both momentum and buoyancy forces are expected to affect the behavior of the air-water jets, similarly to single-phase buoyant jets (see Jirka, 2004).

$$Fr = U_{wo} / \sqrt{g' d_o} \tag{6.7}$$

where g' is a reduced gravity given by

$$g' = g\left\{ \rho_w - \left[\rho_w (1-\varepsilon) + \rho_a \varepsilon \right] \right\} / \rho_w \tag{6.8}$$

in which ρ_w and ρ_a are the water and air density, respectively.

Two regions are clearly observed in Fig. 6-2: a quasi-horizontal bubbly jet, where bubble breakup/coalescence processes were observed visually; and a quasi-vertical bubble plume, where the bubbles rose approximately in a rectilinear path with no significant occurrence of breakup/coalescence. Note that part of this bubble plume was formed by some coalesced bubbles that escaped from the quasi-horizontal bubbly jet, especially for the tests with lower values of *Fr*, where bubble coalescence processes appeared to dominate bubble breakup processes. Minimal lateral spreading of the bubble core from the quasi-horizontal bubbly jet to the quasi-vertical bubble plume was observed visually. Therefore, assuming that the width of the bubble core is equal to the average diameter of the quasi-horizontal bubbly jet (W) and that the length of the bubble core is equal to the length of the bubble plume at z = 24 cm (L) (see sketch in Fig. 6-1), we can see from Fig. 6-2 that the approximate width and length of the bubble core range from about 2-5 cm and 17-40 cm, respectively, both increasing with the gas volume fraction and the densimetric Froude number. It can also be observed that the bubbly jet slightly deflects towards the vertical as the gas volume fraction increases.

A low-frequency lateral oscillation of the bubble core was also observed visually in the tests. The occurrence of such oscillations, also called wandering motions, is usually attributed to buoyancy driven-instabilities and the effect of the tank walls (see Rensen and Roig, 2001; García and García, 2006; Lima Neto et al., 2007b). Figure 6-3 shows typical void fraction and absolute bubble velocity time series measured with the optical fiber probe system. The average values of α and u_b are 1.2 % and 0.6 m/s, respectively. The frequency of oscillation was about 0.05 Hz (more clearly observed from the void fraction time series) and the magnitude of the oscillations was smaller for the velocity time series.

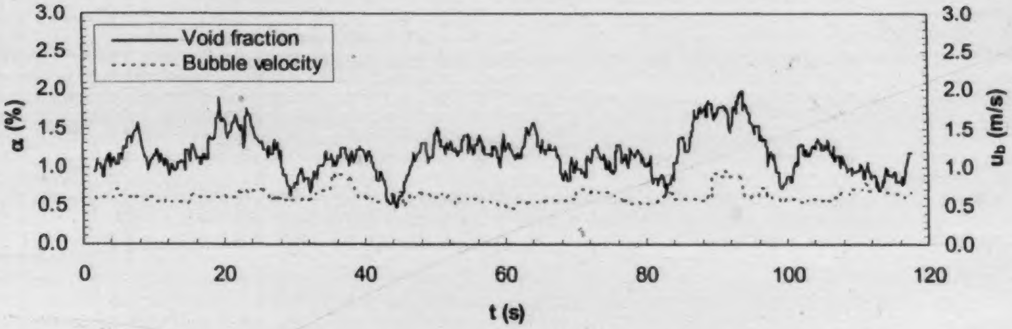

Figure 6-3. Typical void fraction and absolute bubble velocity time series. Measurements taken at $x = 28$ cm and $z = 24$ cm (Exp. 3-5).

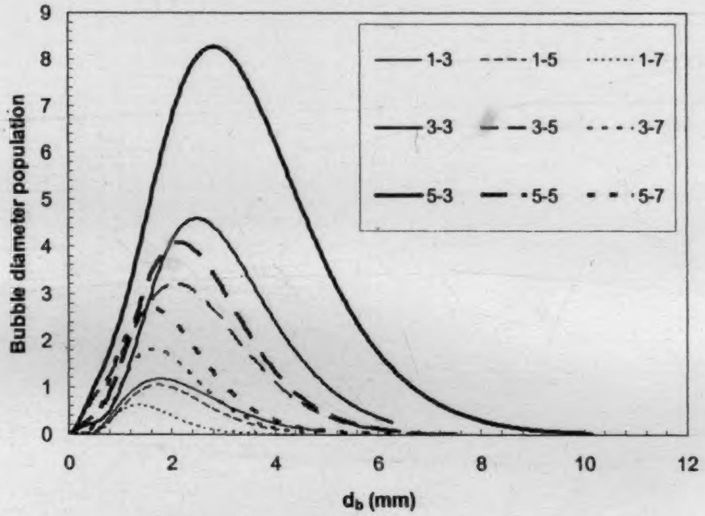

Figure 6-4. Typical bubble size distributions obtained from measurements taken at $x = 16$ cm and $z = 24$ cm.

Figure 6-4 shows typical bubble size distributions obtained from measurements along the bubble plume centerline. For all experiments, the distribution resembles gamma or lognormal curves with average bubble diameters ranging from 1.8-3.4 mm and coinciding approximately with the peaks. Similar curves were also obtained by Varley (1995). The relatively narrow bands of the distributions, as compared to those from experiments with non-uniform bubbles (see Lima Neto et al., 2007a), confirm that the bubbles generated in our tests were approximately of uniform size, as mentioned above (see Fig. 6-2). It can also be seen that the peaks increase and displace to the right along with the gas volume fraction with the result that larger bubbles are generated (e.g., see curves for experiments 1-3 and 5-3), while increases in the densimetric Froude number have the opposite effect (e.g., see curves for experiments 3-3 and 3-7).

Figure 6-5 shows the variations along the bubble core centerline of time-averaged void fraction, (α); bubble frequency, (f); absolute bubble velocity, (u_b); bubble volume-equivalent sphere diameter, (d_b); and interfacial area, (a), for each experiment. Figures 6-5(a), 6-5(b) and 6-5(e) shows that α, f and a follow approximately lognormal distributions, with the peaks displaced to the right. It is clearly seen that the peaks increase as the gas volume fraction increases (e.g., see Exp. 1-5, 3-5 and 5-5), while the bubble plumes become longer as the densimetric Froude number increases (e.g., see Exp. 3-3, 3-5 and 3-7). The lengths of the bubble plumes obtained from Fig. 6-5 ranged from 18 to 44 cm, which are slightly higher than those obtained from the CCD images (see Fig. 6-2). Figures 6-5(c) and 6-5(d) show that u_b and d_b tend to increase as the flow approaches the location of the peak water velocity (see Fig. 6-8 in the next section). Note that for the experiments with lower densimetric Froude numbers (i.e., Exp. 1-3, 3-3 and 5-3), larger bubbles escaped from the weaker water jet and the bubble diameter d_b seemed to decrease with the horizontal distance from the nozzle. Moreover, both u_b and d_b appear to increase with the gas volume fraction and decrease with Fr (e.g., see the same above-mentioned experiments). Similar results were obtained by Varley (1995), who observed an increase in d_b with the air flow rate and a decrease with the water flow rate. Bubble diameters shown in Fig. 6-5(d) ranged from 1.2-3.6 mm and were about 10 % smaller than those obtained from the CCD camera images (see Fig. 6-2), while bubble velocities shown in Fig. 6-5(c) ranged from 41-77 cm/s and were about 25% larger than those obtained from the CCD camera images. Similar results were obtained with the same techniques in vertical bubble plumes and bubbly jets (see Lima Neto et al., 2006a, 2007a).

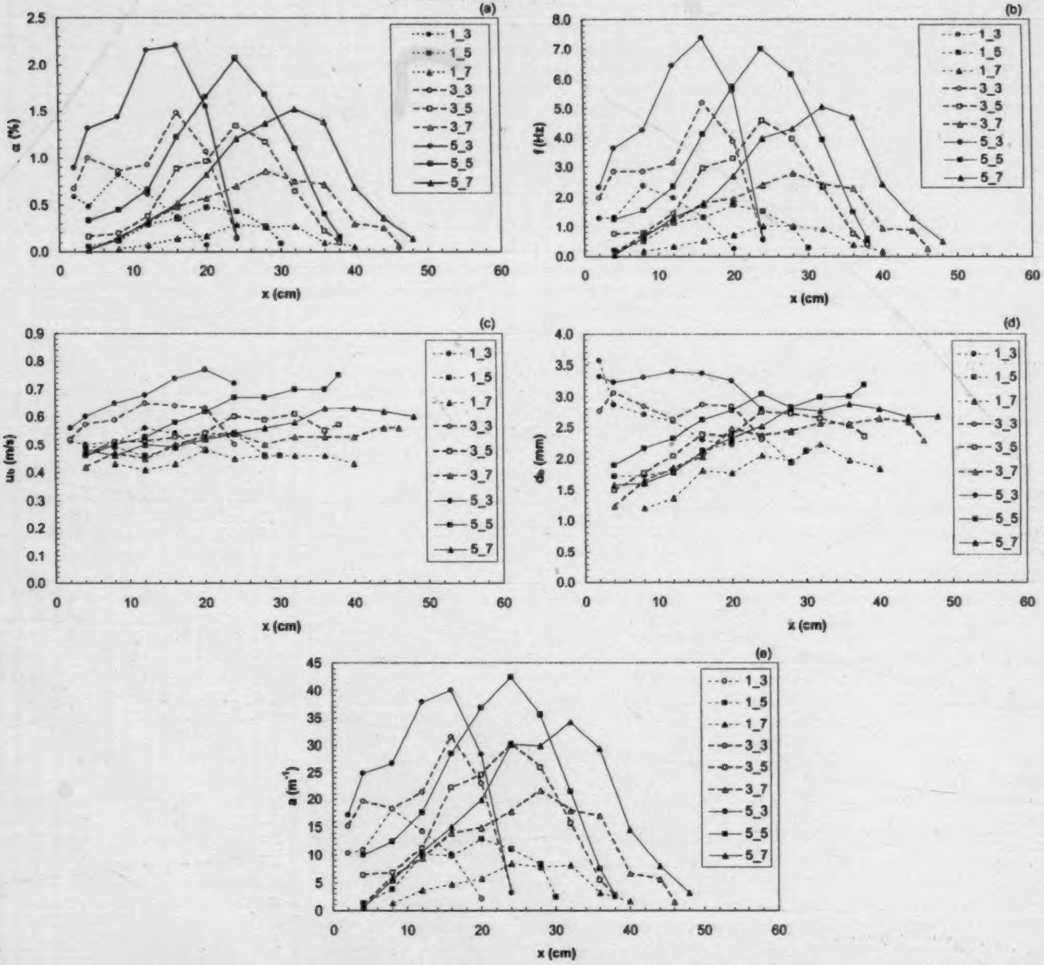

Figure 6-5. Variations along the bubble core centerline of: (a) void fraction, (b) bubble frequency, (c) absolute bubble velocity, (d) bubble diameter, and (e) specific interfacial area. Measurements shown were taken at $z = 24$ cm.

In order to make the results obtained here applicable to other horizontal gas-liquid injection conditions, measured values of W and L as well as longitudinal-averaged values of u_b, d_b and K_La are non-dimensionalized, with a curve fit of experimental data providing the following correlations as a function of the gas volume fraction (ε) and the densimetric Froude number (Fr):

$$\frac{L}{d_o} = Fr^{0.9}\left[-6.54(\varepsilon)^2 + 11.58(\varepsilon) + 0.28\right] \tag{6.9}$$

$$\frac{W}{d_o} = Fr^{1.2}\left[0.44(\varepsilon)^2 + 0.13(\varepsilon) + 0.04\right] \tag{6.10}$$

$$\frac{u_b}{U_{wo}} = Fr^{-1.0}\left[11.79(\varepsilon)^2 - 12.14(\varepsilon) + 6.56\right] \tag{6.11}$$

$$\frac{d_b}{d_o} = Fr^{-0.2}\left[6.68(\varepsilon)^3 - 7.50(\varepsilon)^2 + 2.80(\varepsilon) + 0.40\right] \tag{6.12}$$

$$\frac{(K_L a)d_o}{U_{wo}} = Fr^{-1.0} \times 10^{-3}\left[1.14(\varepsilon)^3 - 1.36(\varepsilon)^2 + 0.80(\varepsilon) + 0.04\right] \tag{6.13}$$

Note that we used a constant mass transfer coefficient $K_L = 4 \times 10^{-4}$ m/s obtained for the range of bubble diameters studied here (see Wüest et al., 1992; McGinnis and Little, 2002), which resulted in volumetric mass transfer coefficients K_La ranging from about 7 to 37 h^{-1}. In the correlations above, we assumed that the forces due to viscosity, surface tension and compressibility are negligible compared to the forces due to momentum and buoyancy, under fully turbulent flow conditions in a relatively shallow water tank. Note that these equations are valid for a specific height z = 24 cm above the nozzle exit. Figure 6-6 shows that Eqs. (6.9) - (6.13) adjusted well to the experimental data, with correlation coefficients ranging from about 0.90 to 0.99.

6.3.2. Liquid flow structure

Figure 6-7 shows a typical sequence of LIF images of the water jet. As sketched in Fig. 6-1, this water jet follows approximately the trajectory of the bubbles in the bubbly jet region (as momentum dominates buoyancy forces), partially separates from the bubble core after some distance from the nozzle (as the bubbles tend to move upwards due to buoyancy forces), and then becomes a surface water jet. This behavior is similar to that of single-phase buoyant jets described by Jirka (2004), except for the separation phenomenon, which has also been observed in bubble plumes in crossflows (see Socolofsky and Adams, 2002).

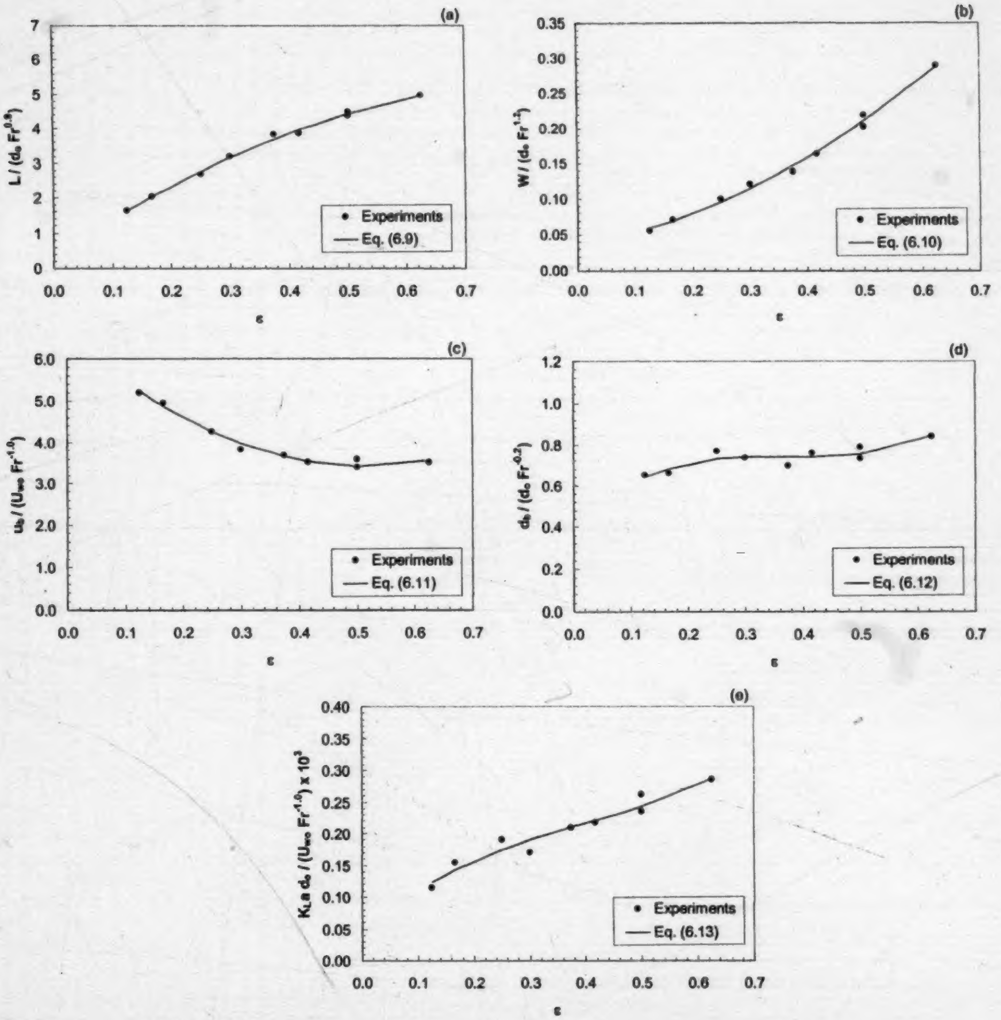

Figure 6-6. Adjustment of the dimensionless correlations for (a) length of the bubble core, (b) width of the bubble core, (c) absolute bubble velocity, (d) bubble diameter, and (e) volumetric mass transfer coefficient to experimental data.

Calculating the horizontal water velocity at the surface jet region from the LIF images, we can estimate the volumetric mass transfer coefficient due to surface aeration at the air-water interface using predictive equations given by Lima Neto et al. (2006b). For example, considering a horizontal water velocity of about 5 cm/s (see Fig. 6-7) and the water depth of 76 cm, we estimated a volumetric mass transfer coefficient of the order of 0.05 h^{-1} for Exp. 3-5, which is much smaller than the corresponding K_La value of 22 h^{-1} estimated above for mass transfer from the bubbles to the water. This implies that most of the oxygen transferred to the water is due to bubble dissolution, even though the contact area between the bubbles and the water is about 20 times smaller than that between the atmosphere and the water.

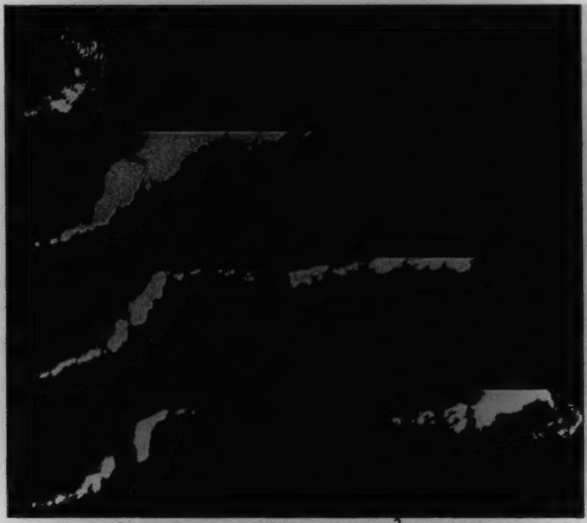

Figure 6-7. Typical sequence of LIF images (32 x 140 cm^2) at times $t = 0.0$, 6.7, 13.3, and 20.0 s after dye injection (Exp. 3-5). Note that the bubbles are shown in the first image while the water jet development is shown in the subsequent images. Part of the water jet inside the bubble core cannot be visualized because the bubbles blocked the laser sheet.

Part of the water jet inside the bubble core could not be visualized from LIF images because the bubbles blocked the laser sheet. However, propeller anemometer measurements of vertical water velocity, (u), shown in Fig. 6-8, confirmed that significant velocities were present inside the bubble core, with the velocity distributions roughly resembling lognormal curves. This occurred because of additional entrainment into the wakes of the bubbles, as observed by Leitch and Baines (1989) and Lima Neto et al. (2007a) in experiments with vertical bubble plumes and bubbly jets, respectively. Figure 6-8 also shows that the magnitude of the velocities and the penetration lengths increase along with the gas volume fraction (see Exp. 1-5, 3-5 and 5-5), while increases in the densimetric Froude number increase the penetration lengths but decrease the peak velocities (see Exp. 3-3, 3-5 and 3-7). It is important to mention that a distinct behavior was observed for Exp. 1-7, where the water jet completely separated from the bubble core at about $x =$

40 cm and two peaks are present in the vertical water velocity profiles shown in Fig. 6-8: one at about $x = 30$ cm due to the flow induced by the bubble plume and another at about $x = 65$ cm due to the water jet itself. This separation was mainly attributed to the relatively small buoyancy as compared to the high momentum of the water jet (see Table 6-1). We can thus conclude that a transition densimetric Froude number for separation of the bubble core from the water jet lies between the values of 31.1 and 48.1, which correspond to experiments 3-7 and 1-7, respectively. We propose that a value of *Fr* higher than about 40 is needed to cause complete separation between the bubble core and water jet.

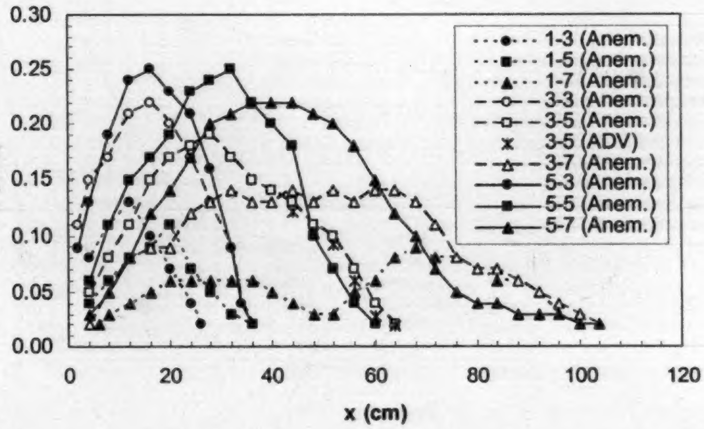

Figure 6-8. Typical variations of mean vertical water velocity along the bubble plume/water jet centerline. Measurements shown were taken at and $z = 24$ cm.

6.3.3. Trajectory of the bubble plumes and water jets

Assuming that the center of the bubble plumes coincides with the location of the peak void fraction measurements [see Fig. 6-5(a)], we can normalize our data and obtain the following relationship to describe the dimensionless trajectory of the bubble plumes:

$$\frac{z_b}{d_o} = Fr^{-1.6}\varepsilon^{-1.2}\left[0.013\left(\frac{x_b}{d_o}\right)^3 - 0.322\left(\frac{x_b}{d_o}\right)^2 + 30.672\left(\frac{x_b}{d_o}\right)\right] \qquad (6.14)$$

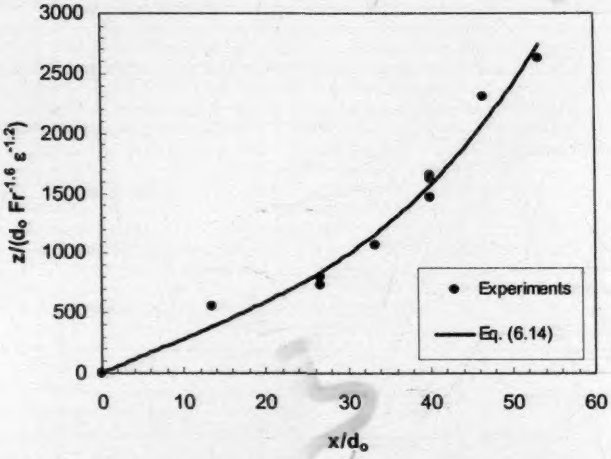

Figure 6-9. Dimensionless trajectory of the bubble plumes.

Figure 6-9 shows the fit of Eq. (6.14) to the experimental data, with a correlation coefficient of 0.98. Similarly, assuming that the center of the water jets coincides with the location of the peak vertical water velocities (see Exp. 3-5 in Figs. 6-7 and 6-8), we obtain the following relationship to describe the dimensionless trajectory of the water jets:

$$\frac{z_w}{d_o} = Fr^{-1.7}\varepsilon^{-1.1}\left[0.228\left(\frac{x_w}{d_o}\right)^2 + 36.202\left(\frac{x_w}{d_o}\right)\right] \qquad (6.15)$$

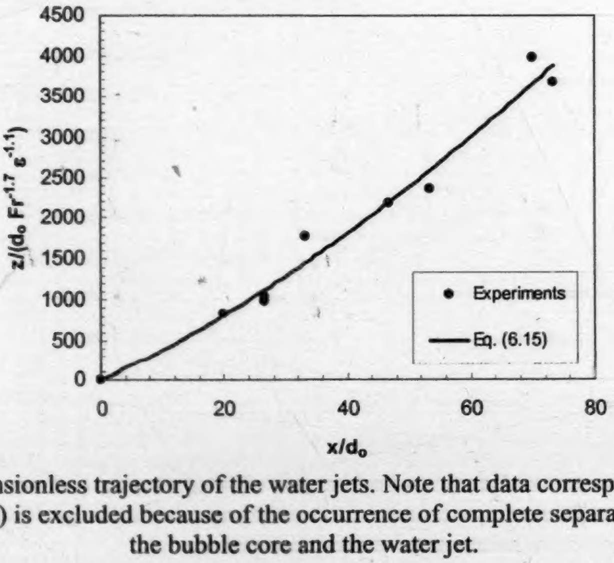

Figure 6-10. Dimensionless trajectory of the water jets. Note that data corresponding to Exp. 1-7 (with $Fr > 40$) is excluded because of the occurrence of complete separation between the bubble core and the water jet.

Figure 6-10 provides the fit of Eq. (6.15) to the experimental data, with a correlation coefficient of 0.98. Note that experimental data corresponding to Exp. 1-7 (with $Fr > 40$) was excluded from this figure because, in this case, the water jet separated completely from the bubble core, as mentioned above. Eq. (6.15) is important because models for simulation of the flow induced by jet aerator systems usually assume that the behavior of the horizontal water jet is not affected by the bubbles (see Morchain et al., 2000; Fonade et al., 2001).

6.3.4. Bubble slip velocity and shape

With the measurements of vertical water velocity and absolute bubble velocity, we can now estimate the bubble slip (or relative) velocity, (u_s). Figure 6-11 shows that bubble slip velocities obtained in this study ranged from about 0.3 to 0.5 m/s and collapsed well within the curve proposed by Lima Neto et al. (2007a) to describe the variation of u_s with d_b in vertical bubbly flows. The values above are higher than the terminal bubble velocity of about 0.2 m/s given by Clift et al. (1978) for isolated bubbles of similar diameters. This occurred because trailing bubbles in the wake of leading bubbles rise faster than isolated bubbles due to drag reduction, as observed by Ruzicka (2000) on experiments on bubbles rising in line. The results shown in Fig. 6-11 are important because models for simulation of bubbly flows usually assume constant slip velocities equal to the terminal bubble velocities given by Clift et al. (1978).

Using the values of u_s and d_b estimated above, we can calculate the bubble Reynolds number ($\mathrm{Re}_b = u_s d_b / \nu_w$), Eötvös number ($E_b = g\Delta\rho d_b^2 / \sigma$), and Morton number ($M_b = g\Delta\rho\mu_w^4 / \rho_w^2\sigma^3$), where $\Delta\rho$ is the difference between the water and air densities, σ is the air-water surface tension and μ_w is the viscosity of water. These dimensionless numbers are generally used to express the importance of inertia, buoyancy, surface tension, and viscosity on single bubbles rising in liquids. For the present study, the ranges of Re_b and E_b were 480-1755 and 0.2-1.7, respectively, and $\mathrm{M}_b = 3.1 \times 10^{-11}$. According to the classical diagram describing the behavior of isolated bubbles provided by Clift et al., (1978), our values of Re_b, E_b and M_b fall within the region of spherical, ellipsoidal and wobbling regimes, which is in agreement with the shapes observed from the CCD images (see Fig. 6-2). Similar results were obtained by Lima Neto et al. (2007a) for vertical bubbly jets.

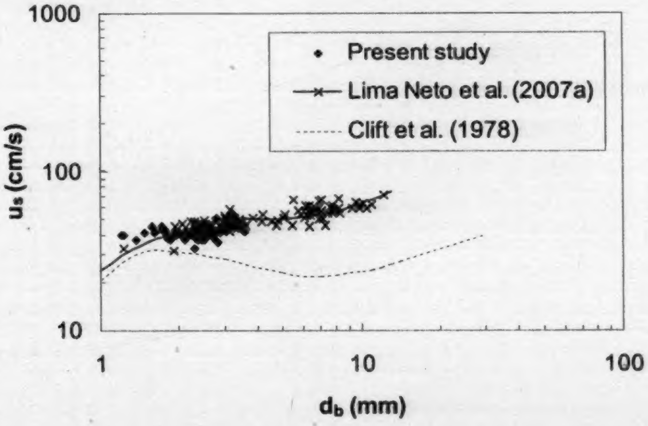

Figure 6-11. Bubble slip velocity *vs.* bubble diameter. Dashed and solid lines indicate fitted curves obtained from the literature pertaining to isolated bubbles and vertical bubbly flows, respectively.

6.4. Applications

The correlations obtained here can be applied to compare the aeration potential for different horizontal air-water injection systems. Defining this aeration potential as the product of the volumetric mass transfer coefficient (K_La) by the approximate area of the bubble core in contact with the water column above the nozzle (W x L), we can estimate, for example, which flow condition studied here is the best for aeration. Figure 6-12 shows that, as expected, the experiment with the highest air and water flow rates (Exp. 5-7) corresponds to the best condition for aeration. On the other hand, experiments with relatively high air flow rates and low water flow rates (e.g., Exp. 5-3) may have comparable aeration potential of those with relatively low air flow rates and high water flow rates (e.g., Exp. 3-5), which in turn will result in higher electricity costs for pumping a higher water flow rate. However, in this case, the benefit will be a higher penetration length of the water jet for circulation and mixing as compared to the experiments with lower water flow rates (see Fig. 6-8). It is important to stress that all experiments conducted here were performed for Re > 8000, where bubbles of approximately uniform sizes were generated. For lower values of Re, we expect the formation of lager bubbles and reduced aeration potential, as mentioned above. Therefore, we recommend that the condition of Re < 8000 should be avoided.

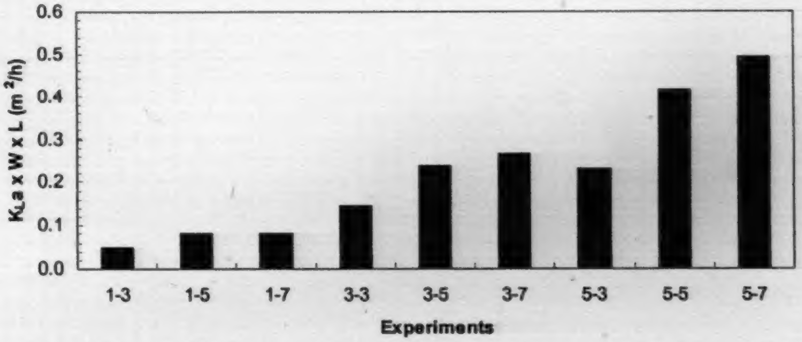

Figure 6-12. Estimated aeration potential for each experimental condition.

Overall, the above results of bubble properties and mean liquid flow structure can also be used to evaluate and validate CFD models for horizontal gas-liquid injection systems. However, caution should be taken when applying these results to systems with different temperatures and high concentration of impurities, which could impact on the two-phase flow behavior and mass transfer characteristics (see Clift et al., 1978; Mueller et al., 2002).

6.5. Summary and conclusions

An experimental study was performed to investigate the behavior of horizontal air-water injection in a water tank. The experimental conditions included gas volume fractions ranging from 13-63%, Reynolds numbers ranging from 10610-24757, and densimetric Froude numbers ranging from 9-48, which produced bubbles with volume-equivalent sphere diameters ranging from about 1-4 mm.

Two important regions were observed from the images of the bubbles: a quasi-horizontal bubbly jet and a quasi-vertical bubble plume. Bubble size distributions obtained from measurements at the bubble plume region resembled gamma or lognormal distributions with relatively narrow bands. This confirmed that the bubbles generated in our tests were approximately of uniform size. Time-averaged distributions of bubble properties along the bubble core centerline were found to depend on the gas volume fraction and the densimetric Froude number. The distributions of void fraction, bubble frequency and interfacial area followed approximately lognormal distributions. On the other hand, absolute bubble velocity and bubble diameter tended to increase with the horizontal distance from the nozzle exit, except for the experiments with lower densimetric Froude numbers, where larger bubbles escaped from the weaker water jet closer to the nozzle exit. Dimensionless correlations for bubble properties and the trajectory of the bubble plumes as a function of the gas volume fraction and the densimetric Froude number were also obtained by curve fitting of experimental data.

It was found that the water jet followed approximately the trajectory of the bubbles in the bubbly jet region, partially separated from the bubble core after some distance from the nozzle, and then became a surface water jet. Both the peak vertical water velocities and the trajectory of the water jets were found to depend on the gas volume fraction and the densimetric Froude number. However, it was found that the water jet completely separated from the bubble core at densimetric Froude numbers higher than about 40. Excluding such particular conditions, a dimensionless correlation for the water jet trajectory as a function of the gas volume fraction and the densimetric Froude number was also obtained by curve fitting of experimental data. This correlation is important because current models for simulation of the flow generated by horizontal gas-liquid injection usually assume that the trajectory of the water jet is not affected by the presence of the bubbles.

Bubble slip velocities were found to be higher than the terminal velocities for isolated bubbles reported in the literature, even though their shapes were similar for the same values of

Reynolds, Eötvös, and Morton numbers. This was attributed to the fact that trailing bubbles in the wake of leading bubbles rise faster than isolated bubbles due to drag reduction, as reported in the literature pertaining to bubbles rising in line. Bubble slip velocities obtained here could be described as a function of bubble diameter and adjusted well to the curve proposed by Lima Neto et al. (2007a) for vertical bubble plumes and bubbly jets. These results are important because two-phase models for vertical bubbly flows typically assume bubble slip velocities of the same order as those for isolated bubbles.

Finally, applications of the results for estimation of the aeration/mixing potential of different horizontal air-water injection conditions are presented and discussed.

6.6. Notation

The following symbols are used in this chapter:

a = air-water specific interfacial area (m^{-1})

C = dissolved oxygen (DO) concentration in water (mg/L)

C_s = saturation DO concentration in water (mg/L)

d_b = bubble volume-equivalent sphere diameter (mm)

d_o = nozzle exit diameter (mm)

f_b = bubble frequency (Hz)

Fr = densimetric Froude number defined by Eq. (6.7)

g' = reduced gravity (m/s^2)

K_L = mass transfer coefficient (m/s)

L = length of the bubble core defined in Fig. 6-1 (cm)

Q_{ao} = air flow rate at the nozzle (l/min)

Q_{wo} = water flow rate at the nozzle (l/min)

Re = Reynolds number defined by Eq. (6.5)

U_{wo} = superficial water velocity at the nozzle exit (cm/s)

u = vertical water velocity (m/s)

u_b = absolute bubble velocity (m/s)

u_s = bubble slip velocity (m/s)

W = width of the bubble core defined in Fig. 6-1 (cm)

x = horizontal distance from the nozzle exit defined in Fig. 6-1 (cm)

x_b = horizontal position of the bubble plume centerline (cm)

x_w = horizontal position of the water jet centerline (cm)

z = vertical distance from the nozzle exit defined in Fig. 6-1 (cm)

z_b = vertical position of the bubble plume centerline (cm)

z_w = vertical position of the water jet centerline (cm)

α = air concentration or void fraction (%)

ε = gas volume fraction defined by Eq. (6.2)

Chapter 7

General Conclusions and Recommendations for Future Research

In the preceding five chapters, we have presented the results and analysis of field and lab studies on gas injection in water. In Chapter 2 we found that oxygen injection into effluent diffusers is an effective means of improving DO levels downstream of effluent outfalls, which can be used when natural water renewal is not sufficient to maintain the desired DO standards. In Chapter 3 it was shown that tank size and geometry affected significantly the flow field induced by circular bubble plumes and water jets. This finding is important to better understand the flow induced by gas injection in lakes, reservoirs and wastewater treatment tanks. In Chapter 4 we found that different nozzle types had significant effect on bubble properties and the flow structure induced by air injection in a water tank. These results can be used to design and optimize gas injections systems for artificial aeration and circulation. In Chapter 5 it was shown that bubble properties and the flow structure induced by vertical injection of gas-liquid mixtures in a water tank depend on the gas volume fraction and Reynolds number at the nozzle exit. The experiments also revealed fundamental results that can be used to model more accurately bubbly flows for aeration, circulation and mixing purposes. In Chapter 6 it was found that the gas volume fraction and densimetric Froude number at the nozzle exit can be used to describe bubble properties and the flow structure induced by horizontal injection of gas-liquid mixtures in a water tank. The experimental results obtained from this study are applicable to the design and optimization of artificial aeration/circulation systems under relatively shallow water conditions. Finally, the results obtained from Chapters 4, 5 and 6 can also be used to evaluate the aeration potential of gas-injection systems in relatively low-velocity streams, as described in Chapter 2.

Overall, this thesis provides important results that advance the knowledge of two-phase flow dynamics in bubble plumes and gas-liquid jets and their artificial aeration/circulation performances. However, there are still some aspects left to continue research on these topics. We suggest the following fundamental and applied research to be further conducted:

Fundamental research

- Experimental study of the effect of bubble-bubble interactions such as collision, coalescence and breakup in gas-liquid flows as well as bubble-particle interactions in gas-liquid-solid flows on bubble size, shape and velocity and induced flow structure;
- Experiments on the structure of the wakes formed by rising bubbles in relatively dense swarms and its effects on the induced flow structure;
- Experimental investigation of the mean, periodic and turbulent liquid flow structure inside the bubble core of gas-liquid flows with relatively high void fractions;
- Detailed measurements of mass transfer induced by single bubbles in clean and contaminated liquids;
- Development, evaluation and validation of CFD models accounting for both micro and macro turbulent flow dynamics as well as mass transfer processes in bubbly flows.

Applied research

- Large-scale experiments or more detailed field studies on bubble plumes and gas-liquid jets. This would be important to investigate the effect of compressibility on bubble properties and the effect of non-confinement on the induced flow structure in large tanks and lakes, and in the ocean.

- Experimental investigation on bubble plumes and gas-liquid jets under stratified water conditions to study both bubble properties and induced flow field;
- Experiments on gas-liquid jets in crossflow to better understand the two-phase flow dynamics in river aeration systems;
- Experimental study to investigate the effect of suspended solids concentration on bubble properties and liquid flow structure;
- Bulk measurements of dissolved oxygen in gas-injection systems containing both clean and contaminated liquids;
- Numerical modeling of bubble plumes and gas-liquid jets including bubble-bubble, bubble-particle and bubble-liquid interactions as well as mean, periodic and turbulent flow dynamics and mass transfer.

References

Abramovich, G. N. (1963). "The theory of turbulent jets". M.I.T. Press, Cambridge, Massachusetts, United States.

Adams, E. E., Golomb, D. S., Herzog, H. J. (1995). "Ocean disposal of CO_2 at intermediate depths". *Energy Conserv. Mgmt.*, 36 (6-9), 447-452.

Akar, P. J.; Jirka, G. H. (1991). "CORMIX2: An expert system for hydrodynamic mixing zone analysis of conventional and toxic submerged multiport diffuser discharges". Technical Report EPA/600/3-91/073, U.S. Environmental Research Laboratory, Athens, Georgia.

Alberta Ambient Air Data Management System (2004). "CASA Data Warehouse – Data Reports". <http://www.casadata.org>

Alberta Environment (1999). "Surface water quality guidelines for use in Alberta". Environmental Assurance Division, Science and Standards Branch, Edmonton, Alberta, 25p.

Alberta Environment (2004). "Alberta River Basins – Water Quality Data". <http://www3.gov.ab.ca/env/water>

Amberg, H. R.; Wise, D. W.; Aspitarte, T. R. (1969). "Aeration of streams with air and molecular oxygen". *Tappi,* 52 (10), 1866-1871.

Barnhart, E. L. (1969). "Transfer of oxygen in aqueous solutions", *J. Sanit. Engrg. Div.*, 95 (3), 645-661.

Beak Consultants Ltd. (1995). "Effluent plume delineation study for Alberta Pacific Forest Industries Inc.". Report, Reference 7.10610.1, Brampton, Ontario.

Boes, R. M., Hager, W. H. (2003). "Two-phase flow characteristics of stepped spillways". *J. Hydr. Engrg.*, 129 (9), 661-670.

Bombardelli, F. (2004). "Turbulence in multiphase models for aeration bubble plumes". PhD thesis, University of Illinois at Urbana-Champaign, Dept. of Civil and Environmental Engineering.

Bouvy, M., Falcão, D., Marinho, M., Pagano, M., Moura, A. (2000). "Occurrence of cylindrospermopsis (Cyanobacteria) in 39 Brazilian tropical reservoirs during the 1998 drought". *Aquat. Microb. Ecol.*, 23, 13-27.

Boyer, C., Duquenne, A. M., Wild, G. (2002). "Measuring techniques in gas-liquid and gas-liquid-solid reactors". *Chem. Engrg. Sci.*, 57 (16), 3185-3215.

Brücker, C., Schröder, W. (2004) "PIV-Study on bubble interaction and wakes in multiphase flows". In: Bubbly Flows – Analysis, Modelling and Calculation, Sommerfeld, M. (Ed.), Springer-Verlag, Berlin, Germany.

Buscalia, G. C., Bombardelli, F. A., García, M. H. (2002). "Numerical modeling of large-scale bubble plumes accounting for mass transfer effects", *Int. J. Multiphase Flow,* 28 (11), 1763-1785.

Chambers, P. A.; Brown, S.; Culp, J. M.; Lowell, R. B. (2000). "Dissolved Oxygen Decline in Ice-Covered Rivers of Northern Alberta and Its Effects on Aquatic Biota." *Journal of Aquatic Ecosystem Stress and Recovery*, 8, 27-38.

Chambers, P. A.; Pietroniro, A.; Scrimgeour, G. J.; Ferguson, M. (1996). "Assessment and validation of modelling under-ice dissolved oxygen using DOSTOC, Athabasca River, 1988 to 1994". Proj. 2231-C1, Northern River Basin Study.

Chambers, P. A.; Scrimgeour, G. J.; Pietroniro, A. (1997). "Winter oxygen conditions in ice-covered rivers: the impact of pulp mill and municipal effluents". *Can. J. Fish. Aquat. Sci.*, 54, 2796-2806.

Chang, K. A., Lim, H. J., Su, C. B. (2003). "Fiber optic reflectometer for velocity and fraction ratio measurements in multiphase flows". *Rev. Sci. Instrum.,* 74 (7), 3559-3565.

Chanson, H. (2002). "Air-water flow measurements with intrusive, phase-detection probes: Can we improve their interpretation?". *J. Hydr. Engrg.,* 128 (3), 252-255.

Chapra, S. C. (1997). "Surface water-quality modeling". McGraw-Hill, Water Resources and Environmental Engineering Series, New York, 844p.

Chaumat, H., Billet-Duquenne, A. M., Augier, F., Mathieu, C., Delmas, H. (2005). "Application of the double optic probe technique to distorted tumbling bubbles in aqueous or organic liquid". *Chem. Engrg. Sci.,* 60 (22), 6134-6145.

Chu, C. R., Jirka, G. H. (2003). "Wind and stream flow induced reaeration". *J. Env. Engrg.*, 129 (12), 1129-1136.

Churchill, M. A.; Elmore, H. L.; Buckingham, R. A. (1962). "The prediction of stream reaeration rates". *J. Sanit. Engrg. Div.*, 88 (4), 1-46.

Clift, R., Grace, J. R., Weber, M. E. (1978). "Bubbles, drops and particles". Academic Press, New York.

Colt, J., Watten, B. (1988). "Applications of pure oxygen in fish culture". Aquacultural Engineering, 7, 397-441.

DeMoyer, C. D., Schierholz, E. L., Gulliver, J. S., Wilhelms, S. C. (2003). "Impact of bubble and free surface oxygen transfer on diffused aeration systems". *Wat. Res.,* 37 (8), 1890-1904.

Dobbins, W. E. (1964). "BOD and oxygen relationships in streams". *J. Sanit. Engrg. Div.*, 90 (3), 53-78.

Dow, K.; Steffler, P. M.; Zhu, D. Z. (2007). "Intermediate field mixing of wastewater effluent in the North Saskatchewan River", *J. Hydr. Engrg., ASCE* (submitted).

Duchene, P., Cotteux, E., Capela, S. (2001). "Applying fine bubble aeration to small aeration tanks". *Wat. Sci. Tech.*, 44 (2-3), 203-210.

Eckenfelder, W. W. (1959). "Absorption of oxygen from air bubbles in water", *J. Sanit. Engrg. Div.*, 85 (4), 89-99.

Environment Canada (2004). "National Climate Archive – Climate Data Online". <http://www.climate.weatheroffice.ec.gc.ca>

Fanneløp, T. K., Hirschberg, S., Küffer, J. (1991). "Surface current and recirculating cells generated by bubble curtains and jets". *J. Fluid Mech.*, 229, 629-657.

Fast, A. W., Lorenzen, M. W. (1976). "Synoptic survey of hypolimnetic aeration", *J. Env. Engrg. Div.*, 102 (6), 1161-1173.

Fast, A. W., Overholtz, W. J., Tubb, R. A. (1975). "Hypolimnetic oxygenation using liquid oxygen", *Wat. Resour. Res.*, 11 (2), 294-299.

Fast, A. W., Overholtz, W. J., Tubb, R. A. (1977). "Hyperoxygen concentrations in the hypolimnion produced by injection of liquid oxygen", *Wat. Resour. Res.*, 13 (2), 474-476.

Felton, K., Loth, E. (2001). "Spherical bubble motion in a turbulent boundary layer". *Phys. Fluids*, 13 (9), 2564-2577.

Fonade, C., Doubrovine, N., Maranges, C., Morchain, J. (2001). "Influence of a transverse flowrate on the oxygen transfer performance in heterogeneous aeration: case of hydro-ejectors". *Wat. Res.*, 35 (14), 3429-3435.

Ford, B., Loth, E. (1998). "Forces on ellipsoidal bubbles in a turbulent shear layer". *Phys. Fluids*, 10 (1), 178-188.

Friedl, M. J., Fanneløp, T. K. (2000). "Bubble plumes and their interaction with the water surface". *Appl. Ocean Res.*, 22 (2), 119-128.

García, C. M., García, M. H. (2006). "Characterization of flow turbulence in large-scale bubble-plume experiments". *Exp. in Fluids*, 41 (1), 91-101.

Gray, D. M.; Prowse, T. D. (1993). "Snow and floating ice". *In* Handbook of hydrology. Edited by D.R. Maidment. McGraw-Hill, Inc, New York.

Gulliver, J. S. (2007). "Introduction to chemical transport in the environment". Cambridge University Press, New York.

Herringe, R. A., Davis, M. R. (1976). "Structural development of gas-liquid mixture flows". *J. Fluid Mech.*, 73, 97-123.

Hetsroni, G. (1989). "Particle-turbulence interaction", *Int. J. Multiphase Flow,* 15(5), 735-746.

Hicks, F. E.; Cui, W.; Andres, D. (1997). "Modelling thermal breakup on the Mackenzie River at the outlet of Great Slave Lake, N.W.T.". *Can. J. Civ. Eng.*, 24 (4), 570-585.

Hou, R.; Li, H. (1987). "Modeling of BOD-DO dynamics in an ice-covered river in Northern China". *Wat. Res.*, 21 (3), 247-251.

Iamandi, C., Rouse, H. (1969) "Jet-induced circulation and diffusion". *J. Hydr. Div.*, 95 (HY2), ASCE, 589-601.

Iguchi, M., Nozawa, K., Tomida, H., Morita, Z. (1992). "Bubble characteristics in the buoyancy region of a vertical bubbling jet", *ISIJ Int.*, 32, 747-754.

Iguchi, M., Okita, K., Nakatani, T., Kasai, N. (1997). "Structure of turbulent round bubbling jet generated by premixed gas and liquid injection", *Int. J. Multiphase Flow,* 23 (2), 249-262.

Iguchi, M.; Takeuchi, H.; Morita, Z. (1991). "The flow field in air-water vertical bubbling jets in a cylindrical vessel", *ISIJ Int.*, 31, 246-253.

Iguchi, M., Tani, J., Uemura, T., Kawabata, H., Takeuchi, H., Morita, Z. (1989). "The characteristics of water and bubbling jets in a cylindrical vessel with bottom blowing", *ISIJ Int.*, 29, 309-317.

Jirka, G. H. (2004). "Integral model for turbulent buoyant jets in unbounded stratified flows. Part I: Single round jet". *Environ. Fluid Mech.*, 4, 1-56.

Jirka, G., Harleman, D. R. F. (1979). "Stability and mixing of a vertical plane buoyant jet in confined depth". *J. Fluid Mech.*, 94, 275-304.

Kiambi, S. L., Duquenne, A. M., Dupont, J. B., Colin, C., Risso, F., Delmas, H. (2003). "Measurements of bubble characteristics: Comparison between double optical probe and imaging". *Can. J. Chem. Engrg.*, 81 (3-4), 764-770.

Kiger, K. T., Pan, C. (2000). "PIV technique for the simultaneous measurement of dilute two-phase flows". *J. Fuids. Engrg., ASME,* 122 (4), 811-818.

Kobus, H. (1968). "The motion of bubbles in liquids". In: Characteristics of self-aerated free-surface flows - Water and waste water – Current research and practice, v. 10, Rao, L., Kobus, H. (Ed.), Erich Schimidt Verlag, Berlin, Germany.

Krenkel, P. A.; Orlob, G. T. (1962). "Turbulent diffusion and the reaeration rate coefficient". *J. Sanit. Engrg. Div.*, 88 (2), 53-116.

Kumar, S., Nikitopoulos, D. N., Michaelides, E. E. (1989). "Effect of bubbles on the turbulence near the exit of a liquid jet", *Exp. Fluids,* 7, 487-494.

Leitch, A. M., Baines, W. D. (1989). "Liquid volume flux in a weak bubble plume". *J. Fluid. Mech.*, 205, 77-98.

Lima Neto, I. E., Zhu, D. Z., Rajaratnam, N. (2006a). "Air injection in water with different nozzles". *J. Env. Engrg., ASCE* (submitted)

Lima Neto, I. E., Zhu, D. Z., Rajaratnam, N. (2007a). "Bubbly jets in stagnant water". *J. Fluid. Mech.* (under review)

Lima Neto, I. E., Zhu, D. Z., Rajaratnam, N. (2007b). "Effect of tank size and geometry on the flow induced by circular bubble plumes and water jets". *J. Hydr. Engrg., ASCE* (accepted)

Lima Neto, I. E., Zhu, D. Z., Rajaratnam, N. (2007c). "Horizontal injection of gas-liquid mixtures in a water tank". *J. Hydr. Engrg., ASCE* (submitted)

Lima Neto, I. E., Zhu, D. Z., Rajaratnam, N., Yu, T., Spafford, M., McEachern, P. (2006b). "Dissolved oxygen downstream of an effluent outfall in an ice-covered river: Natural and artificial aeration". *J. Env. Engrg., ASCE* (accepted)

MacDonald, G; Holley, E. R.; Goudey, S. (1989). "Athabasca River winter reaeration investigation". Final Report, Environmental Assesment Division, Alberta Environment.

Marr, D. H.; Peterson, J. I.; Critchfield, D. H.; Danforth, R. H.; Wiley Jr., F. A. (1993). "The Gulf Island Pond oxygenation project: a unique cooperative solution to an environmental problem". *Tappi*, 76 (7), 159-168.

McCord, S. A., Schladow, S. G., Miller, T. G (2000). "Modeling artificial aeration kinetics in ice-covered lakes". *J. Env. Engrg.,* 126(1), 21-31.

McDougall, T. (1978). "Bubble plumes in stratified environments". *J. Fluid. Mech.,* 85, 655-672.

McGinnins, D. F., Little, J. C. (2002). "Predicting diffused-bubble oxygen transfer rate using the discrete-bubble model". *Wat. Res.,* 36 (18), 4627-4635.

McGinnis, D. F., Lorke, A., Wüest, A., Stockli, A., Little, J. C. (2004). "Interaction between a bubble plume and the near field in a stratified lake". *Water Resour. Res.,*40 (10), W10206.

McWhirter, J. R, Hutter, J. C. (1989). "Improved oxygen mass transfer modeling for diffused/subsurface aeration systems". *AIChE Journal,* 35 (9), 1527-1534.

Milgram, H. (1983). "Mean flow in round bubble plumes". *J. Fluid. Mech.,* 133, 345-376.

Miller, T. G. (2005). "Overwinter lake aeration systems". PhD thesis, University of Alberta, Edmonton, Alberta, 205p.

Moog, D. B.; Jirka, G. H. (1998). "Analysis of reaeration equations using mean multiplicative error". *J. Env. Engrg., ASCE,* 112 (2), 104-110.

Morchain, J., Moranges, C., Fonade, C. (2000). "CFD modelling of a two-phase jet aerator under influence of a crossflow". *Wat. Res.,* 34 (13), 3460-3472.

Motarjemi, M., Jameson, G. J. (1978). "Mass transfer from very small bubbles – The optimum bubble size for aeration". *Chem. Engrg. Sci.,* 33 (11), 1415-1423.

Mudde, R. F. (2005). "Gravity-driven bubbly flows". *Annu. Rev. Fluid. Mech.*, 37, 393-423.

Mueller, J. A., Boyle, W. C., Pöpel, H. J. (2002). "Aeration: principles and practice". CRC Press, New York.

Murzyn, F., Mouaze, D., Chaplin, J. R. (2005). "Optical fibre probe measurements of bubbly flow in hydraulic jumps", *Int. J. Multiphase Flow,* 31 (1), 141-154.

O'Connor, D. J.; Dobbins, W. E. (1958). "Mechanism of reaeration in natural streams". *ASCE Trans.*, 123, 641-684.

Perin, G., Fabris, R., Manente, S., Wagener, A. R., Hamacher, C., Scotto, S. (1997). "A five-year study on the heavy-metal pollution of Guanabara Bay sediments (Rio de Janeiro, Brazil) and evaluation of the metal bioavailability by means of geochemical speciation". *Wat. Res.*, 12, 3017-3028.

Prepas, E. E., Field, K. M., Murphy, T. P., Johnson, W. L., Burke, J. M., Tonn, W. M. (1997). "Introduction to the Amisk Lake Project: oxygenation of deep, eutrophic lake". *Can. J. Fish. Aquat. Sci.*, 54, 2105-2110.

Putz, G.; Odigboh, I.; Smith, D. W. (2000). "Two-dimensional modelling of effluent mixing in the Athabasca River downstream of Alberta Pacific Forest Industries, Inc". Proj. Report 2000-2, Univ. of Alberta.

Rainer, B.; Fonade, C.; Moser, A. (1995). "Hydrodynamics of a new type of ejector". *Bioprocess Engineering, 13, 97-103.*

Rajaratnam, N. (1976). "Turbulent jets". Elsevier Scientific, Amsterdam, The Netherlands.

Rensen, J., Luther, S., Lohse, D. (2005). "The effect of bubbles on developed turbulence". *J. Fluid. Mech.*, 538, 153-187.

Rensen, J., Roig, V. (2001). "Experimental study of the unsteady structure of a confined bubble plume", *Int. J. Multiphase Flow,* 27 (8), 1431-1449.

Riess, I. R., Fanneløp, T. K. (1998). "Recirculation flow generated by line-source bubble plumes". *J. Hydr. Engrg., ASCE,* 124 (9), 932-940.

Risso, F., Ellingsen, K. (2002). "Velocity fluctuations in a homogeneous dilute dispersion of high-Reynolds-number rising bubbles". *J. Fluid. Mech.*, 453, 395-410.

Risso, F., Fabre, J. (1998). "Oscillations and breakup of a bubble immersed in a turbulent field". *J. Fluid. Mech.*, 372, 323-355.

Rosso, D., Stenstrom, M. K. (2006). "Surfactant effects on alpha-factors in aeration systems". *Wat. Res.*, 40 (7), 1397-1404.

Ruzicka, M. C. (2000). "On bubbles rising in line", *Int. J. Multiphase Flow,* 26 (7), 1141-1181.

Sahoo, G. B.; Luketina, D. (2005). "Gas transfer during bubbler destratification of reservoirs". *J. Env. Engrg., ASCE,* 131 (5), 702-715.

Sahoo, G. B., Luketina, D. (2006). "Response of a tropical reservoir to bubbler destratification". *J. Env. Engrg., ASCE,* 132 (7), 736-746.

Schierholz, E. L., Gulliver, J. S., Wilhelms, S. C., Henneman, H. E. (2006). "Gas transfer from air diffusers". *Wat. Res.,* 40 (5), 1018-1026.

Schreier, H.; Erlebach, W.; Albright, L. (1980). "Variations in water quality during winter in two Yukon rivers with emphasis on dissolved oxygen concentration". *Wat. Res*., 14, 1345-1351.

Smoot, J. L. (1988). "An examination of stream reaeration coefficients and hydraulic conditions in a pool and riffle stream". PhD Thesis, Virginia Polytechnic Institute and State University: Blackburg, VA.

Socolofsky, S. A. (2001). "Laboratory experiments of multi-phase plumes in stratification and crossflow". PhD thesis, MIT, Massachusetts, 233p.

Socolofsky, S. A., Adams, E. E. (2002). "Multi-phase plumes in uniform and stratified crossflow". *J. Hydr. Res.,*40 (6), 661-672.

Soga, C. L. M., Rehmann, C. R. (2004). "Dissipation of turbulent kinetic energy near a bubble plume". *J. Hydr. Engrg.,* 130 (5), 441-449.

Sommerfeld, M. (2004). "Bubbly flows - analysis, modelling and calculation". Springer-Verlag, Berlin, Germany.

Speece, R. E. (1996). "Oxygen supplementation by U-tube to the Tombigbee river". *Wat. Sci. Tech*., 34 (12), 83-90.

Stantec (2004). "Alberta-Pacific Forest Industries Inc. dissolved oxygen trials – February 2004". Prepared for Alberta-Pacific Forest Industries Inc. by Stantec Consulting Ltd., Calgary, Alberta.

Sun, T. Y.; Faeth, G. M. (1986a). "Structure of turbulent bubbly jets – I. Methods and centerline properties", *Int. J. Multiphase Flow,* 12, 99-114.

Sun, T. Y.; Faeth, G. M. (1986b). "Structure of turbulent bubbly jets – II. Phase property profiles", *Int. J. Multiphase Flow,* 12, 115-126.

Swan, C., Moros, A. (1993). "The hydrodynamics of a subsea blowout". *Appl. Ocean Res.,* 15 (2), 269-280.

Szekely, J.; Themelis, N. J. (1971). "Rate phenomena in process metallurgy". Wiley, New York.

Tian, Y. (2005). "Dissolved Oxygen Modeling and Sediment Oxygen Demand Study in the Athabasca River" MS thesis, Department of Civil and Environmental Engineering, University of Alberta.

Town, C. A.; Mavinic, D. S.; Moore, B. (1989). "A study of water quality in an urban river and potential improvement using a prototype instream aerator". *Can. J. Civ. Eng.*,16, 308-316.

Turner, J. S. (1986). "Turbulent entrainment: the development of the entrainment assumption, and its application to geophysical flows". *J. Fluid. Mech.*, 173, 431-471.

Tyler, R. G. (1946). "Polluted streams cleared up by aeration". *Civil Engrg.*,16, 348-349.

Uberoi, M., Freymuth, P. (1970). "Turbulent energy balance and spectra of the axisymmetric wake". *Phys. Fluids,* 13 (9), 2205-2210.

Varley, J. (1995). "Submerged gas-liquid jets: bubble size prediction", *Chem. Eng. Sci.,* 50 (5), 901-905.

Wagner, M. R., Pöpel, H. J. (1998). "Oxygen transfer and aeration efficiency – Influence of diffuser submergence, diffuser density, and blower type". *Wat. Sci. Tech.*, 38 (3), 1-6.

Wain, D. J., Rehmann, C. R. (2005). "Eddy diffusivity near bubble plumes". *Wat. Resour. Res.*, 41 (9), W09409.

Water Pollution Control Federation, WPCF (1988). "Aeration - Manual of Practice – No. FD-13", Alexandria, VA.

Water Survey of Canada (2004). "Water Level and Streamflow Statistics".<http://www.wsc.ec.gc.ca/staflo>

Whipple, W. J., Yu, S. L. (1970). "Instream aerators for polluted rivers", *J. Sanit. Engrg. Div.*, 96 (5), 1153-1165.

Whipple, W. J.; Yu, S. L. (1971). "Aeration systems for large navigable rivers", *J. Sanit. Engrg. Div.,* 97 (6), 883-904.

Wüest, A, Brooks, N. H., Imboden, D. M. (1992). "Bubble plume modeling for lake restoration". *Wat. Resour. Res.*, 28 (12), 3235-3250.